UNIVERSIDAD POLITÉCNICA DE MADRID
Escuela Técnica Superior de Ingeniería Aeronáutica y del Espacio

Isolated flames of lean hydrogen-air mixtures in narrow gaps

DOCTORAL THESIS

Submitted for the degree of Doctor by:

Alba Domínguez González
Master of Science in Aeronautical Engineering

Madrid, 2024

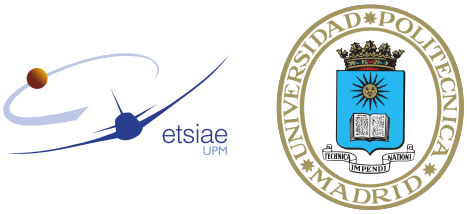

UNIVERSIDAD POLITÉCNICA DE MADRID
Escuela Técnica Superior de Ingeniería Aeronáutica y del Espacio

Doctoral Degree in Aerospace Engineering

Isolated flames of lean hydrogen-air mixtures in narrow gaps

D O C T O R A L T H E S I S

Submitted for the degree of Doctor by:

Alba Domínguez González
Master of Science in Aeronautical Engineering

Under the supervision of:
Dr. Daniel Martínez Ruiz

Madrid, 2024

Title: Isolated flames of lean hydrogen-air mixtures in narrow gaps

Author: Alba Domínguez González

Doctoral Programme: Aerospace Engineering

Thesis Supervision:

Dr. Daniel Martínez Ruiz, Associate Professor, Universidad Politécnica de Madrid (Supervisor)

External Reviewers:

Professor Forman A. Williams (UCSD, USA)
Dr. Pierre Boivin (AMU, France)

Thesis Defense Committee:

Thesis Defense Date:

This work and its scientific diffusion has received financial support from the Agencia Estatal de Investigación of Spain through projects S2CARE (PID2019-108592RA-C43), GROWTHy (TED2021-129446B-C43) and from Ministerio de Innovación, Ciencia y Universidades and Comunidad de Madrid through project GreenH2 (PRTR-C17.I1). Furthermore, the research stay at UCSD was made possible thanks to financial assistance from the Programa Propio I+D+I 2022, through a movility scholarship for PDI.

A mis mecenas

Acknowledgements

As I reach the conclusion of my PhD journey, I would like to take this opportunity to thank all the people who have contributed to its success.

First and foremost, I want to express my deepest gratitude to Daniel Martínez Ruiz, my advisor. Thank you for giving me the opportunity to embark on this adventure. Your guidance, support, and dedication throughout these years have been invaluable. This thesis would not have been possible without your wisdom and hard work. I am especially grateful for your continuous encouragement to attend conferences and travel to explore new places.

I would also like to thank the entire combustion group. Special thanks to Víctor Muntean and Miguel Encinar for their initial pushes, and to Enrique Flores, my companion during the first year. Thanks to the laboratory technicians, and to Nereida, Pedro, Ignacio, and Jorge, your company, laughter, and support have been greatly appreciated. Thanks as well to the turbulence team, Adal and Carlos, and to the Carlos III combustion group for those spectacular images of the Hele-Shaw cell.

A special thank you to Antonio Sánchez for giving me the opportunity to conduct a research stay at UCSD, and for introducing me to asymptotic expansions. To Edu and Paco, thank you both for making my time in San Diego truly unforgettable.

I am also deeply grateful to Luc Vervisch and Pascale Domingo. Thank you for hosting me at INSA and providing me with a fresh perspective on the problem. Thanks to the PhD group there, we are not made of sugar. Thanks, Thomas.

To my friends. Sofi and David, thank you for putting up with me at home for so many years. Cris and Carol, thank you both, you embody the saying, a true friend is a treasure. Thanks to the master propulsion class. Thanks as well to the climbing crew for so many sunny mornings.

Finally, to my parents and my sister, thank you for your unconditional support. Thank you for being an example of resilience.

Abstract

The project of this doctoral thesis focuses on the study of the propagation of deflagration fronts in lean hydrogen-air mixtures. This is a relevant topic addressing safety challenges in the use of hydrogen as an alternative fuel, whose ultimate goal is the development of a more efficient and clean power generation system in the future. The objective of this doctoral thesis is to analyze isolated configurations of lean hydrogen-premixed flames which conform weak but hazardous reactive fronts in channels and gaps, as a representation of accidental combustion in confined leakage scenarios.

The first part of the thesis focuses on the numerical study of two stationary canonical configurations that propagate through a simplified setup, a Hele-Shaw chamber formed by two parallel plates. The stable structures are an isolated circular flame and a double-cell flame, whose two tips are separated by a chemically frozen gap. This analysis includes a description of the flow field as well as a parametric space exploration, based on the heat-losses parameter and the buoyancy effects. A significant result arises from the parametric study: both flame configurations coexist under the same set of parameters. This bi-stable behavior depends on the flow history, allowing the appearance of one or the other steady structure by varying the initial condition at ignition. This work led to the first publication in the *'Proceedings of the Combustion Institute'* in 2022, entitled *'Stable circular and double-cell lean hydrogen-air premixed flames in quasi-two-dimensional channels'*. The contents can be found in chapter 4 Steady-state propagation.

After the presentation of the two canonical steady configurations, chapter 5 focusses on the ignition transients as a key factor for the formation of one or the other isolated configurations. An analysis is conducted through a series of simulations with different initial conditions, where flow segmentation and tracking allow the display of temporal evolution of variables associated with specific flame kernels. This study identifies two processes that determine the merging process between isolated kernels to form the double-cell structure: confinement by adjacent flame fronts and the oscillatory seeding process. Moreover, the incorporation of irregularities with noise at the initial conditions enabled the formation of both kind of propagating structures in the same conditions, characteristic of real-life observations. This second study was developed during the Fifth Turbulence Madrid Workshop, held at ETSIAE in the summer of 2023, and led to a second publication in the *'Proceedings of the Combustion Institute'*, entitled *'Pathway dynamics to double-cell premixed flames in lean hydrogen–air mixtures'*, published in 2024. Moreover, additional collaborations with researchers at UC3M granted the experimental observation of the multiplicity of regimes and validation of the predictions of this work. This was published in *'Physics of Fluids'* with the title *'Unveiling the bi-stable character of stealthy hydrogen–air flames'*. The results are included in chapter 5 Transient dynamics.

After these two sections of results, two more specific aspects are discussed through various methods. Chapter 6 presents a theoretical approach based on asymptotic techniques, allowing for a scale analysis of the problem, applied in this case to the circular configuration. This study began during a research stay at the University of California, San Diego, in the summer of 2022, under the supervision of Prof. Antonio L. Sánchez. On the other hand, chapter 7

links the high heat losses sustained by this configuration type to the curvature of the flame kernel. Specially, a composition-space analysis was proposed to extract particular details of the physical mechanisms involved. The problem is projected onto local curvilinear coordinates according to the isocontours of species scalar, to separate normal components aligned with the gradient of species and tangential contributions. This final analysis was initiated during a research stay at INSA, Rouen in the summer of 2024, under the supervision of Prof. Luc Vervisch.

All the physical understanding obtained from the main studies is gathered in chapter 8, offering a general discussion on the topic. Finally, chapter 9 draws the main conclusions of this work, highlighting the achieved goals and potential repercusion on the field, and details future prospects of research.

All things considered, this work conforms a coherent approach based on numerical and asymptotic methods that has helped to provide further understanding on the behavior of isolated near-limit hydrogen flames, shedding some light on the physical mechanisms and conditions for their appearance. In conclusion, it may serve for the development of future preventive strategies against accidents of hydrogen-fueled devices and grant further scientific analyses and discussion.

Resumen

El proyecto de tesis doctoral se centra en el estudio de propagación de frentes de defragración sobre mezclas pobres de hidrógeno-aire. Estudio enmarcado en temas de seguridad en uso de hidrógeno como nuevo combustible, cuyo fin último es un futuro más eficiente y limpio en términos energéticos. El objetivo de esta tesis doctoral es analizar configuraciones aisladas cuasi-bidimensionales de llama pobre hidrógeno-aire en premezcla.

La primera parte de la tesis se centra en presentar las dos configuraciones canónicas de llama cuasi-bidimensional que se propagan de forma estacionaria por el interior de una cámara de combustión Hele-Shaw. Se trata de una configuración circular y una doble, cuyas dos cabezas se encuentran separadas por una zona químicamente congelada. El estudio abarca, tanto una descripción del flujo, como una exploración del espacio paramétrico, basado en los parámetros de pérdida de calor y constante gravitacional. Es aquí, durante el estudio paramétrico, donde llegamos al primer hallazgo significativo, las dos configuraciones de llama parecen coexistir bajo el mismo conjunto de parámetros. Este comportamiento bi-estable parece depender de la historia del flujo, pudiendo obtener una u otra configuracion estacionaria cambiando la condición inicial. Este trabajo da lugar a una primera publicación, en la revista *'Proceedings of the Combustion Institute'* in 2022, con el título de *'Stable circular and double-cell lean hydrogen-air premixed flames in quasi two-dimensional channels'*. El contenido de este articulo puede encontrarse en el capítulo 4.

Una vez presentadas las dos configuraciones canónicas, se estudian los transitorios de ignición como punto clave en la consecución de una u otra configuración. Se presenta un estudio de igniciones en el que se analizan una serie de casos de simulación. Mediante una segmentación del flujo se siguen los distintos núcleos de llama, permitiendo el estudio de la evolución temporal de variables ligadas a núcleos específicos. Se señalan durante este estudio dos procesos que dictan el proceso de 'unión' entre dos núcleos aislados para dar lugar a la estructura doble, el confinamiento por frentes de llama adyacentes y el proceso oscilatorio y sembrado. Además, se incorpora ruido sobre las condiciones iniciales para dar lugar a casos irregulares en los que se da la formación de las dos configuraciones de llama estudiadas en la misma simulación, característico de las observaciones experimentales. Este segundo estudio se desarrolló durante el 'Fifth Turbulence Madrid Workshop' celebrado en la ETSIAE en el verano de 2023 y da lugar a la segunda publicación, también en el *'Proceedings of the Combistion Institute'*, con el título de *'Pathway dynamics to double-cell premixed flames in lean hydrogen–air mixtures'* publicado ya en 2024. Colaboraciones adicionales con investigadores de la UC3M permitieron la observación experimental de la multiplicidad de regímenes y la validación de las predicciones de los trabajos previos. Esto fue publicado en la revista *'Physics of Fluid* con el título de *'Unveiling the bi-stable character of stealthy hydrogen–air flames'*. El contenido de estos artículos queda reflejado a lo largo del capítulo 5.

Tras esta primera ronda de resultados, en los siguientes dos capítulos se discuten dos aspectos algo más concretos. El capítulo 6 presenta una aproximación teórica basada en técnicas asintóticas, permitiendo un análisis de las escalas del problema, aplicado en este caso a la configuración circular. Este estudio se inició durante una estancia de investigación en la Universidad de California, San Diego, en el verano de 2022, bajo la supervisión del Profesor

Antonio L. Sánchez. Por otro lado, el capítulo 7 relaciona las altas pérdidas de calor soportadas por este tipo de configuración con la curvatura del núcleo de llama. Se proyecta el problema en ejes locales en función del escalar de especies, para separar las contribuciones normales y tangenciales. Este análisis se desarrolló durante una estancia de investigación en el INSA de Rouen en el verano de 2024, bajo la tutela del Profesor Luc Vervisch.

Finalmente, el capítulo 8 presenta una discusión sobre las implicaciones físicas de los resultados obtenidos para, posteriormente, pasar a las conclusiones en el capítulo 9.

Este trabajo constituye un planteamiento teórico basado en métodos numéricos y asintóticos que ha contribuido a comprender mejor el comportamiento de los kernels aislados, arrojando algo de luz sobre los mecanismos físicos y las condiciones de su aparición. El estudio servirá para el desarrollo de futuras estrategias preventivas contra accidentes en dispositivos alimentados por hidrógeno y abrir futuros análisis y discusiones científicas.

Table of Contents

Chapter 1

Motivation

1.1 Climate change and decarbonization policies

The sustained emissions of anthropogenic GreenHouse Gases (GHG) to the atmosphere, primarily carbon dioxide (CO_2), have attained the highest levels in history according to the United Nation's Intergovernmental Panel on Climate Change (UN - IPCC). Their sixth assessment report defines this urging threat as "code red for humanity". The scientific knowledge on the now-happening effects of such conditions is well established. The consequences, previously predicted by science, include vast loss of ice mass, accelerated sea-level rise, severe heat waves, and an irreversible depletion of biodiversity and natural ecosystems. Figure 1.1 presents the dramatic increase in CO_2 emissions since the industrial revolution while natural sinks are not able to capture all the carbon emitted, leading to a constant accumulation in the atmosphere.

The historical framework for the fight against climate change begins with the 1972 United Nations Conference on the Human Environment in Stockholm, which targeted the social awareness of the environmental impact of our society. The concept of sustainability, with an eye on biodiversity, already appeared during the 'Earth Summit' in Rio 1992. Likewise, compromises for the reduction of GHG were adopted through the Kyoto Protocol in 1997, where emission trading policies and clean development mechanisms were initiated. The Paris Agreement on Climate Change, the United Nations Climate Change Conference in 2015, must be highlighted as one of the largest international collaborative efforts. It achieved the adhesion of more countries, based on voluntary commitments to reduce emissions. China and the United States ratify the agreement, the two countries leading the list of emissions levels (30% and 14% respectively). China is committed to reach its peak emissions before 2030, null carbon by 2060 while the United States searches for a $50 - 52\%$ reduction in the emissions referring to 2005 levels for 2030. Regarding the European Union, due to its early industrialization, it has historically been one of the main contributors to CO_2 emissions. Nowadays, it is responsible for approximately $8 - 10\%$ of global carbon dioxide emissions, according to the International Energy Agency (IEA) data. The European Union is imposing restrictions on the emissions of GHG to reach the objectives of cutting anthropogenic pollutant emissions by 55% before 2030 and achieving a climate-neutrality scenario by 2050.

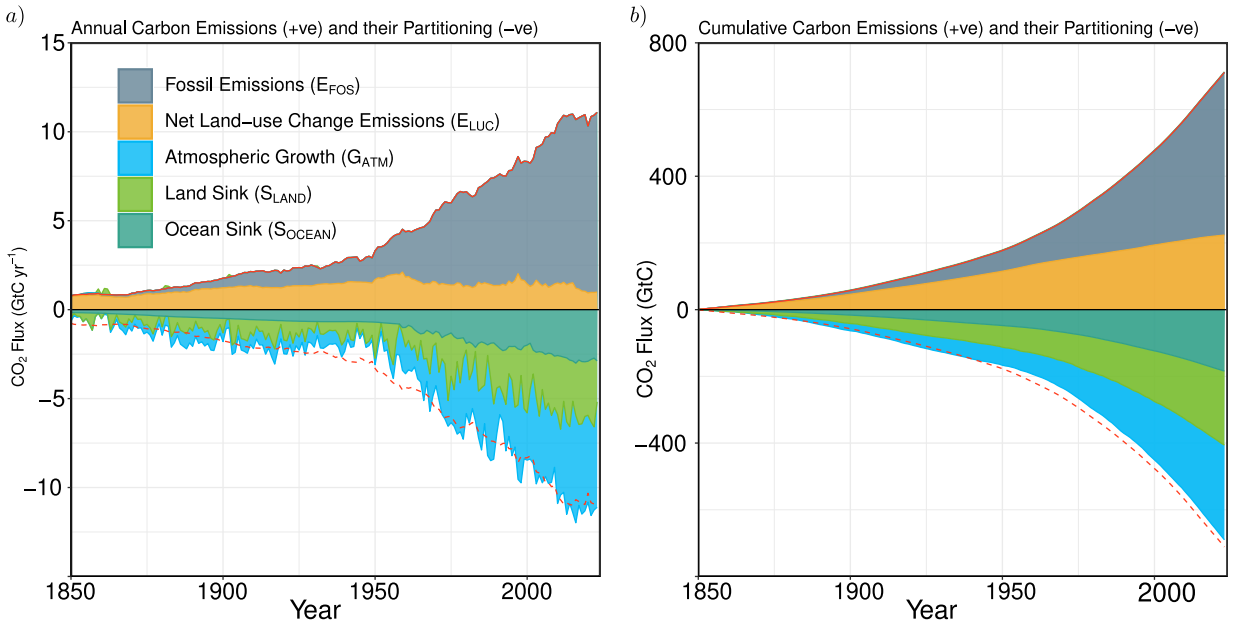

Figure 1.1: Combined components of the global carbon budget in history, for fossil CO2 and land-use change emissions as well as their partitioning among the atmosphere. Annual estimates (a) and cumulative flux (b) are depicted. The red line shows total emissions, with a mirroring dashed red line. Figure reproduced from Friedlingstein et al., 2024.

The agreement focuses mainly on three aspects, the first one is the limitation of the temperature rise, maintaining average warming below 2ºC to the pre-industrial levels through strong emission restrictions. The second one proposes greater adaptation to the impacts derived from climate change, including action plans to protect ecosystems. Finally, the third one focuses on ensuring financial flows to support climate change mitigation and adaptation in developing countries. Paris agreement gave rise to the 2030 Agenda, a general roadmap to sustainable development, and the Sustainable Development Goals (SDG), 17 universal objectives concerning social, environmental and economic issues. Goal number seven appeals directly to energy transformation: 'Ensure access to affordable, reliable, sustainable and modern energy for all'.

1.2 The role of hydrogen

High-energy activities, requiring intense heat production, are evidently the main contributors to CO_2 emissions summing up to more than 30% of the total sources. To this regard, there are two main lines of action. First, strict regulations on the operation of Power and Heat Generation Devices are envisioned, with ancillary penalties in the form of increased maintenance costs and reduced power output caused by the need for increased efficiency and pollutant reduction. Second, the use of new alternative fuels is being proposed to meet the same goals, targeting the reduction of carbon content and the standards of handling safety. Requiring both of them an initial investment, the regularization of the operation of energy generation will lead to performance penalties and increased maintenance costs; while, the use

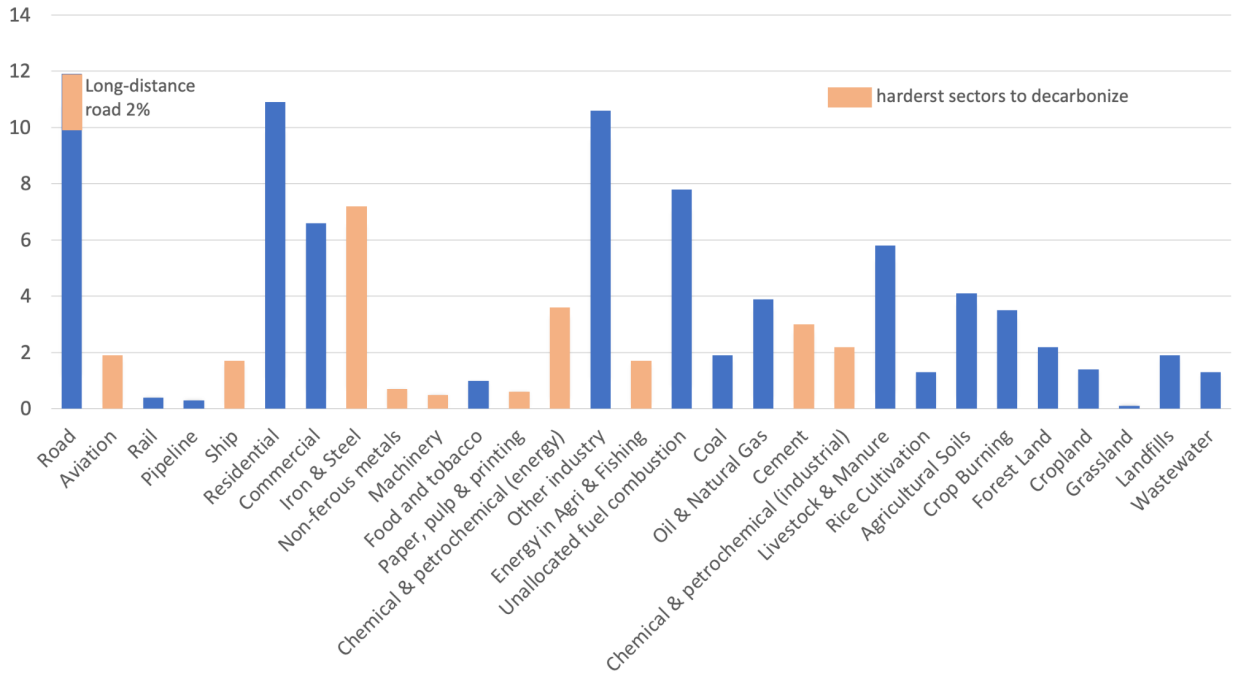

Figure 1.2: Estimates of CO_2 emissions [%] related to different energy services, highlighting those sectors that will be the most difficult to decarbonize (up to 27 % of total). Figure reproduced from Ritchie et al., 2020.

of new alternative fuels not only demands a large economic investment but also an effort in training and development of new technologies and infrastructures.

Specifically, hydrogen (H_2) was considered a potentially clean fuel long before current discussions on energy issues and climate change. Nowadays, its null carbon emissions make hydrogen a great candidate to lead the decarbonization of difficult-to-electrify sectors such as heavy industry or long-distance transport, replacing fossil fuels with a higher carbon footprint. Figure 1.2 highlights those challenging sectors. Thanks to the relentless development of renewable energy technologies, the production of green H_2 has become a realistic choice to store, in chemical bonds, the excess of electricity generated using wind and solar power. This energy-vector strategy may well compete with hydro and battery storage over extended periods (>1000 hours). Besides ensuring the feasibility of green H_2 production, important research efforts are also being allocated to develop its distribution and storage infrastructures, to globally rise the competitiveness of H_2 as a clean alternative. In light of this, further chemical transformation to synthesize ammonia (NH_3) and adapting the existing gas network for its use with H_2 and blends are some of the most-viable alternatives to reduce the investment drawback of developing a whole new distribution system. The injection of H_2 into the current EU grid would constitute a large-scale storage system with an available capacity of 1200 TWh of CH_4 (by 2018).

Moreover, an increasing number of countries are turning their attention to the renewable production of H_2; some examples are the new production plants announced in Portugal, Spain,

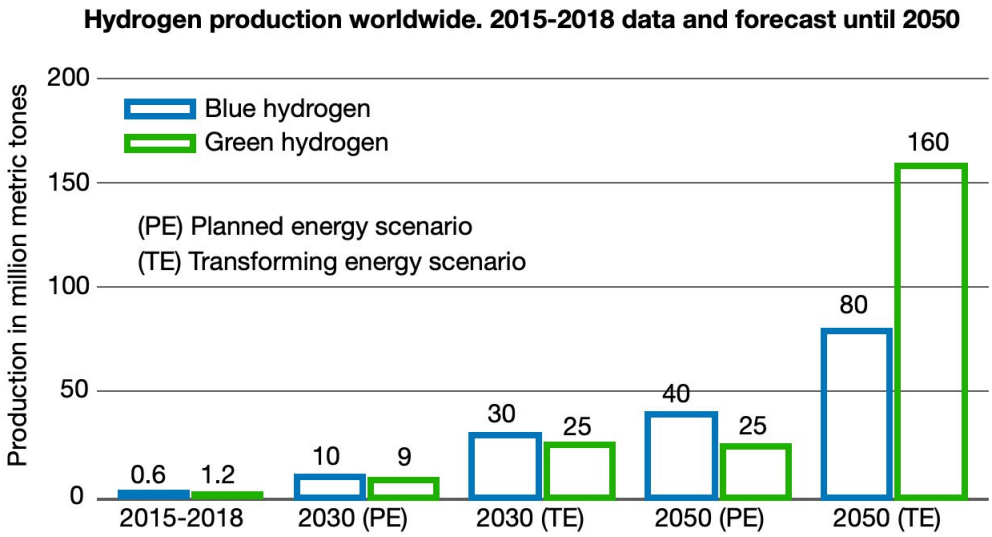

Figure 1.3: Global hydrogen production outlook by type 2015-2050. Reproduced from IRENA, 2020

the Netherlands, China, Australia, or Japan (Bezdek, 2018). According to the International Renewable Energy Agency (IRENA, 2020), over one million metric tons of green hydrogen have been produced worldwide between 2015 and 2018, and the forecast for the next 30 years elevates this figure up to two orders of magnitude within the Transforming Energy Scenario (TE), which describes an ambitious, yet realistic, energy transformation pathway largely based on renewable energy sources and steadily improved energy efficiency. On the other hand, the Planned Energy Scenario (PE), which considers a perspective on energy system developments based on governments' current energy plans (as of 2019), lowers the TE prediction of green H_2 production by a factor of 6, see fig. 1.3. Regardless of the scenario, the outlook anticipates a growing economy in the H_2 sector that will require updated knowledge to turn it into a key player in enabling the collective strategy for sustainable energy transition.

Additionally, H_2 is known to be the most energy-releasing per unit mass (but low specific energy per unit volume) and easily ignitable fuel considered for widespread use in society. Therefore, safety issues need to be addressed during the challenging replacement of carbon-containing fuels with H_2. It represents a considerable hazard during storage and handling (Dagdougui et al., 2018, Staffell et al., 2019 Salvi and Subramanian, 2015). Understanding hazard as "situation that has the potential for causing damage to people, property, or the environment" (AIChE/CCPS, 2000), we can readily advert that the primary hazard associated with any H_2-fueled system is inadvertently producing a flammable or detonable mixture, leading to a fire spread or detonation. It poses a greater risk compared to other carbon-fuels, taking into account that hydrogen is typically stored, transported, or used in pressurized conditions. The ranges may vary depending on uses, 7-70 bar for industrial applications and grid injection, up to 200 filling gas cylinders, and reaching the highest values of 350-700 bar for refueling stations. The storage and handling of hydrogen are the main technological obstacles to the safe and widespread use of this zero-carbon alternative (Edwards et al., 2007). Many of the studies on H_2 stations deal with deflagration or detonation events. They

all exemplify the potential risk of its use and the urgent need to develop safety guidelines. Examples of explosions related to hydrogen are not uncommon. We can cite the accident at Muskingum river Power Plant in 2007 as one of the most representative events (Frazier, 2007). Unfortunately, this is not an isolated case. In 2019, a refueling station in Norway and a chemical plant in California (USA) reported accidents while filling a truck with H_2 (Pagliaro and Iulianelli, 2020). All things considered, safety measures involve an adequate control over potential accidents that can result in losses of lives, infrastructure and deterioration of the environment. Most important, such control must rely on the scientific understanding of the fundamental mechanisms that give rise to a dangerous event. For this reason, all the efforts to bring H_2 to the end-user must run in parallel with the development of safe and reliable technology.

1.3 State of the art

The low density and high diffusivity of hydrogen in ambient conditions reduce the potential of explosion in open space with respect to heavier gases such as gasoline or propane, which dangerously accumulate near the ground surface (Thomas et al., 2015). Contrarily, when available in confined conditions its dilution is hindered and ignition hazards increase because of its particular properties: it shows the widest flammability range and the lowest required ignition energy of any fuel. On top of this, volume confinement promotes pressure increase together with the inherent temperature rise of combustion processes. These combined effects induce greater propagation speeds of the combustion wave, or deflagration, in the reactive mixture of H_2 and air. These reactants, in the presence of an ignition source, give rise to a flame that can accelerate under the expansion of combustion products and the effect of intrinsic instabilities. For sufficiently intense accelerations, the deflagration can transit to a detonation of greater destructive character. These reactive atmospheres can occur accidentally owing to an undesired leakage of fuel, and then generate safety risks, or they can be mixed intentionally, for aeronautical propulsion or technological applications (Kailasanath, 2003).

The present study aims to address accidental leakage conditions of H_2 in the surroundings of technological devices and the ignition of its mixture with air in a fundamental spirit. This framework enables to define the context of ultra-lean mixture conditions in confined geometries. Regardless of the scenario, the desirable control of the ignition event and the subsequent combustion processes rely on the understanding and predictability of physical interactions, and, therefore, on the knowledge of dominant mechanisms and scales that govern the reactive flow. In particular, throughout this thesis emphasis will be placed on quasi-two-dimensional isolated flame kernels.

Numerous fundamental studies in open atmospheres of the combustion process of H_2-air mixtures have been offered by the scientific community in the last fifty years. In 1985, Y. Zel'dovich presented the mathematical steady solution for a spherical flame, the so-called flame ball (Zeldovich et al., 1985). In this study, the stability of the solution depends on the balance between the heat released by the front and the heat losses through radiation. Therein, the large mass diffusivity of the fuel with respect to the thermal diffusivity of the mixture was already pointed out as an essential feature. Two possible radii were found, where only the

larger remains stable. In Buckmaster et al., 1990, a theoretical study on the structure and stability of non-adiabatic flame balls is posed. A steady-state solution was presented using large activation energy asymptotic techniques following Zel'dovich's model and adding a heat loss volumetric term.

Simultaneously, in 1990, this flame configuration was first observed experimentally by P. D. Ronney in a drop tower at the NASA Lewis Research Center in Cleveland, Ohio. Microgravity conditions were obtained during 2.2 s of freefall. Flame balls were found in all mixture families tested when the Lewis number of the deficient reactant was sufficiently low (high diffusivity of H_2) and the composition was sufficiently close to flammability limits. Surprisingly, the flammability limits at these microgravity tests were significantly more dilute than those at Earth gravity, 3.35% vs. 4% H_2 (Ronney, 1990). In 1994, new experiments were carried out in drop towers and parabolic flights, which confirmed that these stable structures do not exhibit self-propagation, as indicated by their absence of movement. There, transient dynamics relevant to the present manuscript results were identified: for mixtures sufficiently far from flammability limits, flame balls consistently split into more flame kernels; for more dilute mixtures, closer to the flammability limits, stable larger flame balls are observed, whereas smaller flame balls shrink and eventually extinguish, probably aided by convective effects (Ronney et al., 1994). Finally, in 1998, results from experiments conducted on the STS-83/MSL-1 Space Shuttle mission were published highlighting the strong influence of unequal rates of diffusion of thermal energy and reactants (Ronney et al., 1998). In fact, curvature effects enhance the local burning rate and together with heat loss mechanisms play a major role in the arising and stability of these spherical structures.

Motivated by this simplified configuration and experimental feasibility, numerous theoretical studies came to light addressing drifting nearly-circular flame cells, which have been found theoretically and numerically when introducing convective heat transfer as the key stabilizing effect (Weeratunga et al., 1990, Buckmaster and Joulin, 1991, Minaev et al., 2001, Grcar, 2009). Later the prediction of stable flame ball radius was offered when including the radiative nature of heat losses (Fernández-Tarrazo et al., 2011, Fernández-Tarrazo et al., 2012). Therein, additional prediction of the lean flammability limit was calculated use made of the one-step reduced chemical scheme developed by Fernández-Galisteo et al., 2009. Additional efforts regarding the chemical kinetics of hydrogen combustion have led to important advances on the understanding of the properties and effects of elementary reactions in defining its flame properties (Sánchez and Williams, 2014).

Contrarily, two-dimensional quiescent circular flames have been usually disregarded owing to the mathematical incompatibility of the solution when prescribing a diffusion-controlled and non-moving structure (Matkowsky and Sivashinsky, 1979). In addition, numerical studies of planar cusp and ring-shaped flamelets under the effects of radiative (Kagan and Sivashinsky, 1997) and conductive (Chen et al., 2017, Z. Lu and Li, 2021) heat losses have offered further descriptions of evolving fronts, closely related to the flame dynamics studied hereafter (Fernández-Galisteo et al., 2018, Kurdyumov et al., 2020, Fernández-Galisteo et al., 2023). Other theoretical analyses have also tried to address this phenomenon from a nearly equidiffusive $\mathrm{Le} \simeq 1$, low-heat-release and one-dimensional reduction of the formulation (Yañez et al., 2023).

Recently, other simplified experiments with partial confinement have been devised in the spirit of analyzing laboratory-based results. Specifically, studies in narrow channels, such as Hele-Shaw chambers, have shown particularities of lean hydrogen-air premixed flames (Kuznetsov and Grune, 2019, Veiga-López, Martínez-Ruiz, et al., 2020, Ballossier et al., 2024). However, it is the combination of intense conductive heat losses through the walls, provided by confinement, and high diffusivity of fuel in H_2-air flames that enable the propagation of isolated drifting flames in nearly two-dimensional configurations, as previously explored numerically by Martínez-Ruiz et al., 2019. Later, this behavior was confirmed experimentally in vertical narrow channels with gaps smaller than 6 mm, under equivalence ratios $\phi < 0.3$, forming isolated fronts that weakly burn a reduced area of the available mixture (Veiga-López, Kuznetsov, et al., 2020). Figure 1.4 shows the different propagation regimes found therein, though the visualization of condensation paths with Schlieren imaging. The upper row corresponds to downward propagating flames while the bottom one displays the upward-propagation modes. From left to right, cases with smaller channel height or lower concentration are shown. The morphology of the front shifts progressively from a continuous flame, to a splitting unsteady process, to finally reach the isolated propagation kernels in (c-c1, f-f1), that leave linear paths of water behind.

The present study offers new developments in the understanding of lean premixed hydrogen-air flames subject to partial confinement in narrow gaps. Particularly, the aforementioned weak burning kernels arising when heat losses through the plates are dominant in the reactive scenario are addressed. This document focuses on the dynamics and structure of two stable quasi-planar canonical flame configurations. 'Canonical', something that follows a canon, is used to highlight the steady typologies of flames following a simple and regular structure which identifies them: the isolated circular flame and the double-cell structure. The dynamics of flames is generally a complex process to deal with, generally conditioned by intense non-linear effects via transport and consumption of the reactants and heat release. Moreover, these processes are strongly linked to the flow dynamics. As a result of the complexity, it is common to rely on simple canonical configurations to shed some light on the main physical effects taking place. In general, the theoretical construct of a planar flame is widely used in combustion science, not only as a comparative reference value but as a basis for many models that emulate more complex flames. Besides the planar flame, and regarding the characteristic lean hydrogen-air mixture, the three-dimensional flame ball explains many of the defining features also present in the studied cases of this thesis. Therefore, this work aims to provide a new framework for fundamental studies on nearly two-dimensional canonical configurations of premixed flames.

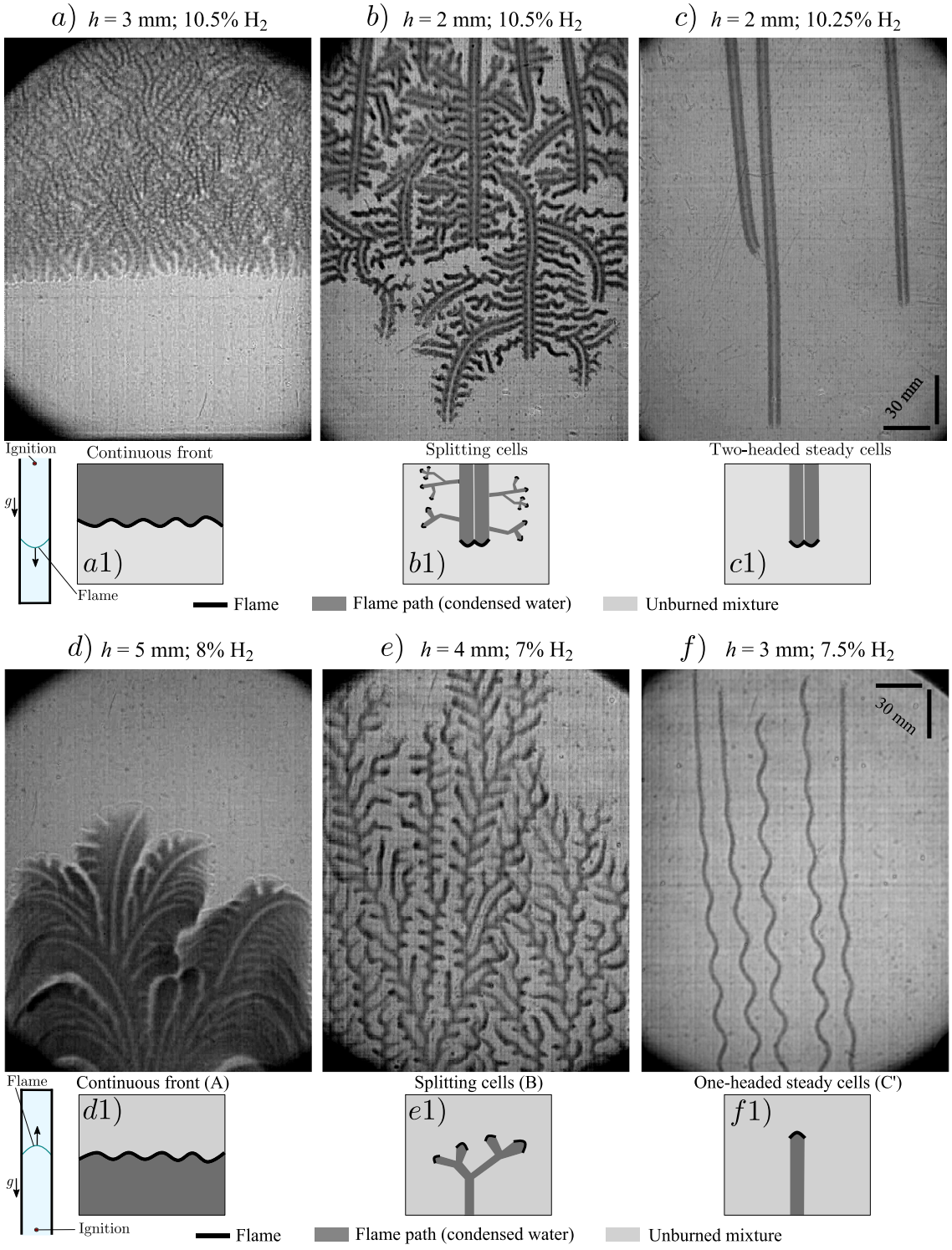

Figure 1.4: Different propagation modes for lean hydrogen flames. Upper row, downward-propagation, image and scheme of (a- a1) continuous flame front propagation, (b-b1) splitting cells forming fractal patterns, and (c-c1) several two-headed isolated steady flame cells. Bottom row, analogous representation for upward-propagation, continuous front (d-d1), splitting cells (e-e1) and several one-heade isolated steady flame cells. Figure extracted from Veiga-López, Kuznetsov, et al., 2020.

Chapter 2

Physical considerations

Among the various types of hazards and risks posed by the use of hydrogen as a fuel, the undesired ignition of reactive mixtures in association with gaseous oxidizer in partially confined geometries is considered in detail. The analyzed scenario is that of a potential gaseous fuel leak that may come into a confined space, enabling a chemically reactive gas to burn upon its contact with an energy source. This may be the case of H_2 leakage in the casing of a fuel cell or engine, which can undergo an accidental combustion process in presence of static sparks or surface hot spots. The present study aims to shed some light on the fundamental problem of a lean hydrogen-air premixed flame propagating inside a simplified geometry between two parallel plates, namely a Hele-Shaw chamber (see left panel of fig. 2.1).

Owing to the high mass diffusivity of H_2 a corrugated flame front is expected, promoted through thermo-diffusive intrinsic instabilities. Whenever the gap distance is small enough, conductive heat losses through the walls will induce extended quenching of the reactive areas, a very characteristic feature of the specific configuration. Therefore, a fragmentation of the front into isolated flame kernels traveling through the Hele-Shaw chamber is typically found. Under a certain set of thermochemical parameters, two stable flame configurations are found after a characteristic ignition transient, an isolated circular flame and a double-headed one. As explained in subsequent chapters, these two configurations propagate steadily through the channel burning the available fuel at two different speeds. Figure 2.1 (right side) shows illustrative numerical results from a simulation example and the two steady configurations.

In this chapter, the spatial configuration of the chamber and the reactive mixture properties are first described in section 2.1. Then, based on the scales and setup properties, a series of flow hypotheses are pointed out within section 2.2.

2.1 Hele-Shaw configuration

A Hele-Shaw chamber is the control volume that is formed between two parallel plates, regardless of their inclination with respect to the action of gravity. This configuration has been extensively used for fundamental research on potential flows. For example, the classical configurations displayed in Van Dyke, 1982, or recently by Baukal Jr, 2020, were able to

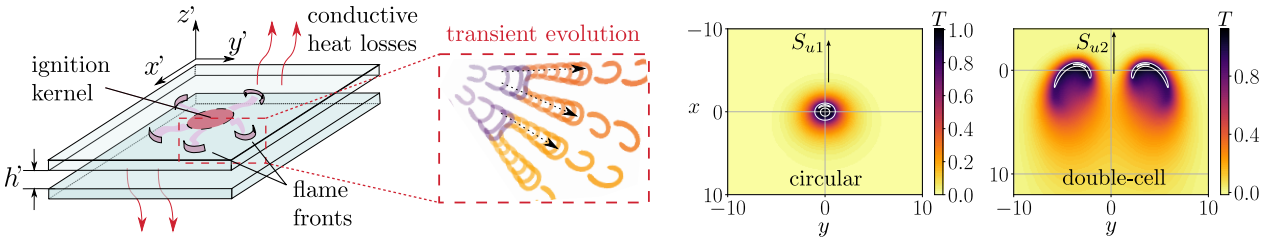

Figure 2.1: Sketch of an ignition transient in-between the two horizontal plates forming the Hele-Shaw chamber. The two steady reactive kernels found in the presence of heat losses: the isolated circular and double-cell flames.

extract great visualizations of quasi-planar flows.

The Hele-Shaw flow requires the parallel flat plates of characteristic size L' to be separated apart a small distance h' compared to viscous layers, giving rise to a narrow channel, our combustion chamber. This small gap ensures the dominance of viscous forces inside the cavity. The main feature of this configuration is the difference of scales between the transverse length and the in-plane size, of several orders of magnitude, $h'/L' \ll 1$. In turn, it leads to a low effective Reynolds number of the flow at hand,

$$\mathrm{Re}_{\mathrm{eff}} = \frac{U'h'}{\nu}\frac{h'}{L'} \ll 1, \tag{2.1}$$

where ν is the kinematic viscosity of the fluid and U' the characteristic speed of the flow induced in the chamber. Therefore, the Hele-Shaw flow approximation is commonly used in fluid dynamics for channels that are in contact with the atmosphere at their far edges, allowing for pressure relief. In this document, almost planar configurations in which the dominant viscous effects produce a highly laminar character are studied.

2.1.1 Lean hydrogen-air mixtures

Based on the scenario of fuel leakage into a cavity, a lean hydrogen-air mixture is considered to be filling the Hele-Shaw chamber. Once the reactive mixture is ignited, a quasi-isobaric deflagration front propagates through the quiescent gases. First, we shall explore some of the most characteristic properties of this fuel, be the high diffusivity of the radical H atom (likewise H_2) and its thermo-chemical character. These facts will produce some particular behaviors of the premixed flames, both through transport effects and through the combustion kinetics process itself.

Transport properties

As the theory of dilute gases provides a realistic description of the molecular interactions under a wide range of ambient conditions, we shall consider an ideal gas to be representative of the lean reactive mixture. The description of molecular transport is fundamental for understanding and modeling the mixing of chemical species and conductive heat transfer, with the kinetic information expressed in terms of the collisions of individual molecules. In the problem of interest, there will be small and light molecules (fuel H_2, H-atom), and also

heavy ones that correspond to the oxidizer or some of the combustion products. The great difference in sizes and weights leads to preferential-diffusion effects, the main transport feature of hydrogen combustion, the light molecules tend to diffuse at greater speeds than the heavy ones.

Diffusion velocities of diverse species in the mixture arise from gradients of composition (Fickian diffusion), temperature gradients (thermal diffusion), pressure gradients (barodiffusion) and other body forces that could act diversely among the different species (e.g. electric forces affecting particles depending on their charge). All these effects are included in the exact multicomponent diffusion equation, Stefan-Maxwell relation, expressed in terms of molar X_i and mass Y_i fractions,

$$\nabla X_i = \sum_{j=1}^{N} \frac{X_i X_j}{\rho' D'_{ij}} \left(\frac{\vec{j}_j}{Y_j} - \frac{\vec{j}_i}{Y_i} \right) + \sum_{j=1}^{N} \frac{X_i X_j}{\rho' D'_{ij}} \left(\frac{D'_{Tj}}{Y_j} - \frac{D'_{Ti}}{Y_i} \right) \nabla \left(\ln T' \right) + (Y_i - X_i) \nabla \left(\ln p' \right) + \frac{\rho'}{p'} \sum_{j=1}^{N} Y_i Y_j \left(\vec{f}_i - \vec{f}_j \right), \quad (2.2)$$

being ρ' the density, p' the pressure and T' the temperature dimensional values of the mixture. Additionally, the mass diffusion coefficients D'_{ij}, the thermal diffusivity D'_{Ti}, body forces $\vec{f}$ and the mass flow by diffusion $\vec{j}$ must be included. However, it is not generally solvable for the diffusion velocities in terms of the concentration distributions. Then, it is typically simplified when pressure gradients do not make a significant contribution and also a null differentiation in body forces is observed. Most of the times, the diffusion velocity is dictated by concentration gradients and the temperature distribution solely. In fuel-air combustion systems the simplification of diluted environments applies. In fact, a minor presence of fuel species diffuse into the one in excess, commonly nitrogen in air. This fact enables the assumption of a binary interaction, and the diffusion flux is simplified to,

$$Y_i \vec{v}_{d_i} = -D'_i \left(\nabla Y_i + \alpha_i Y_i \frac{\nabla T'}{T'} \right), \quad (2.3)$$

with D'_i the binary diffusion coefficient for the minor species i and α_i the thermal diffusion factor for the binary law, which corresponds to the species flux due to temperature gradients or Soret effect. Thermal diffusion tends to drive light molecules to hotter regions, specially fuel reaching the reaction zone that changes the local composition of the mixture. This effect is not negligible at near-stoichiometric conditions (hottest flames), and taking it into account would be important for an accurate flame speed determination. However, Soret term is not included in the following lean-flame analyses, where lower temperature values are attained. The analogous term in the energy flux corresponding to modified heat transport through mass diffusion, Dufour effect, is not included in the following neither.

The great mass diffusivity of this fuel is classically compared to the heat diffusivity of the mixture. The quotient between these two coefficients defines the non-dimensional Lewis number $\mathrm{Le} = D'_T / D'_i$, which compares the thermal and species diffusive speeds. In a lean-premixed hydrogen-air mixture, the low effective Lewis number $\mathrm{Le} \simeq 0.3$ gives rise to the fact that the fuel is diffusing faster than the heat released by the flame. In general, with

a small Le number thicker fronts and higher reaction rates are expected. In addition, it is worth highlighting the tendency to generate thermo-diffusive instabilities, the appearance of corrugated fronts by local combustion reinforcement.

Chemical kinetics and flame structure

As a general feature, the reaction rate of hydrogen combustion is greater than that of other fuel gases, giving rise to faster production rates and potentially more unstable flames. However, the particular type of fuel, mixture and ambient conditions determine the evolution of chemical kinetics, the flame structure and the burnt adiabatic temperature T'_a. Since hydrogen is the simplest fuel molecule, its chemical kinetics is widely studied, constituting the base for the more complex hydrocarbon kinetics. Fundamental knowledge has been gained through previous scientific efforts that enabled an adequate modeling of such reactive processes. Detailed schemes such as the San Diego mechanism, have provided recent advances in understanding the intricate reactions (Sánchez and Williams, 2014), and can be used to describe the combustion process through twenty reversible fundamental reactions and eight species: H_2, O_2, H_2O, H, O, OH, HO_2 and H_2O_2.

The intermediate reactions are characterized by their activation temperature, pre-exponential factor and concentration of the reactants. Arrhenius' modeling for the combustion processes implicitly assumes Boltzmann equilibrium of the internal degrees of freedom of the species. These reactions can be organized into four groups, see the left scheme of fig. 2.2: shuffle reactions (initial generation of the radical pool); formation/consumption of hydroperoxyl radical HO_2 (often present when reactions relative to H_2O_2 are not present), radical-radical elementary reactions (recombination processes) and hydrogen-peroxide formation/consumption (negligible at high temperature and low pressure). In addition, reduced schemes are commonly used to lower computational costs. One of the best-known schemes is the skeletal mechanism, describing accurately premixed and non-premixed combustion over the whole flammability range with only twelve reactions, see right side of fig. 2.2. The different types of reactions define the inner structure of the planar premixed H_2-air flames, which display multiple layers. This arrangement is composed of an intermediate thin layer of fast radical production, where branching takes place, and two radical recombination areas, where recombination, diffusion and convection effects compete, upstream and downstream of the production layer.

Furthermore, additional H_2 flame properties can be derived from chemical kinetics through the balance of two relevant processes: a chain-branching radical production, dominated by the limiting characteristic time of the first shuffle reaction (1f); and the radical recombination processes, limited by (4f). The interplay between the branching overall reaction $3H_2+O_2 \rightarrow 2H_2O+2H$, fast at high temperature and weakly exothermic, and the recombination of radicals through $2H+M \rightarrow H_2+M$ that controls the bulk of heat release, defines the crossover temperature T'_c. For mixtures attaining temperatures below crossover, recombination becomes faster than chain-branching and the chemical reaction cannot progress. Oppositely, whenever $T' > T'_c$ the fast production of radicals sustains the reaction and the H_2 flame can take place. In fact, H atom can only exist under a small concentration within a thin layer where $T'_c < T' < T'_a$, which controls H_2 oxidation. When modifying the equivalence ratio of the mixture, the flammability limits are defined as the values of fuel concentration (lean

Rate coefficients in Arrhenius form $k = BT^n\exp(-T_a/T)$.

		B[a]	n	T_a[a]	Ref.
Shuffle reactions					
$H + O_2 \rightleftharpoons OH + O$		3.52×10^{16}	−0.7	8590	[20]
$H_2 + O \rightleftharpoons OH + H$		5.06×10^{4}	2.67	3165	[24]
$H_2 + OH \rightleftharpoons H_2O + H$		1.17×10^{9}	1.3	1825	[25]
$H_2O + O \rightleftharpoons OH + OH$		7.00×10^{5}	2.33	7321	See text
Hydroperoxyl reactions					
$H + O_2 + M \rightleftharpoons HO_2 + M$	k_0	5.75×10^{19}	−1.4	0.0	[10]
	k_∞	4.65×10^{12}	0.44	0.0	
$HO_2 + H \rightleftharpoons OH + OH$		7.08×10^{13}	0.0	148	[32]
$HO_2 + H \rightleftharpoons H_2 + O_2$		1.66×10^{13}	0.0	414	[32]
$HO_2 + H \rightleftharpoons H_2O + O$		3.10×10^{13}	0.0	866	[31]
$HO_2 + O \rightleftharpoons OH + O_2$		2.00×10^{13}	0.0	0.0	[35]
$HO_2 + OH \rightleftharpoons H_2O + O_2$		2.89×10^{13}	0.0	−250	[31]
		4.50×10^{14}	0.0	5500	[39]
Radical–radical recombination reactions					
$H + OH + M \rightleftharpoons H_2O + M$		4.00×10^{22}	−2.0	0.0	[10]
$H + H + M \rightleftharpoons H_2 + M$		1.30×10^{18}	−1.0	0.0	[10]
$O + O + M \rightleftharpoons O_2 + M$		6.17×10^{15}	−0.5	0.0	[10]
$H + O + M \rightleftharpoons OH + M$		4.71×10^{18}	−1.0	0.0	[10]
Hydrogen peroxide reactions					
$OH + OH + M \rightleftharpoons H_2O_2 + M$	k_0	2.76×10^{25}	−3.2	0.0	[44]
	k_∞	9.55×10^{13}	−0.27	0.0	See text
$HO_2 + HO_2 \rightleftharpoons H_2O_2 + O_2$		1.03×10^{14}	0.0	5556	[37]
		1.94×10^{11}	0.0	−709	[37]
$H_2O_2 + H \rightleftharpoons HO_2 + H_2$		2.30×10^{13}	0.0	4000	See text
$H_2O_2 + H \rightleftharpoons H_2O + OH$		1.00×10^{13}	0.0	1804	[24]
$H_2O_2 + OH \rightleftharpoons H_2O + HO_2$		1.74×10^{12}	0.0	160	[49]
		7.59×10^{13}	0.0	3660	[49]
$H_2O_2 + O \rightleftharpoons HO_2 + OH$		9.63×10^{6}	2.0	2009	[24]

Rate coefficients in Arrhenius form $k = BT^n\exp(-T_a/T)$ for the skeletal mechanism with rate parameters in mol, s, cm^3, kJ, and K.

	Reaction		B	n	T_a
1f	$H + O_2 \rightarrow OH + O$		$3.52\ 10^{16}$	−0.7	8590
1b	$OH + O \rightarrow H + O_2$		$3.03\ 10^{4}$	−0.26	72
2f	$H_2 + O \rightarrow OH + H$		$5.06\ 10^{4}$	2.67	3165
2b	$OH + H \rightarrow H_2 + O$		$3.03\ 10^{4}$	2.63	2433
3f	$H_2 + OH \rightarrow H_2O + H$		$1.17\ 10^{9}$	1.3	1825
3b	$H_2O + H \rightarrow H_2 + OH$		$1.28\ 10^{10}$	1.19	9412
4f	$H + O_2 + M \rightarrow HO_2 + M$[a]	k_0	$5.75\ 10^{19}$	−1.4	0.0
		k_∞	$4.65\ 10^{12}$	0.44	0.0
5f	$HO_2 + H \rightarrow OH + OH$		$7.08\ 10^{13}$	0.0	148
6f	$HO_2 + H \rightarrow H_2 + O_2$		$1.66\ 10^{13}$	0.0	414
6b	$H_2 + O_2 \rightarrow HO_2 + H$		$2.69\ 10^{12}$	0.36	27,888
7f	$HO_2 + OH \rightarrow H_2O + O_2$		2.89×10^{13}	0.0	−250
			$4.50\ 10^{14}$	0.0	5500
8f	$H + OH + M \rightarrow H_2O + M$[b]		4.00×10^{22}	−2.0	0.0
8b	$H_2O + M \rightarrow H + OH + M$[b]		1.03×10^{23}	−1.75	59,675
9f	$H + H + M \rightarrow H_2 + M$[c]		$1.30\ 10^{18}$	−1.0	0.0
9b	$H_2 + M \rightarrow H + H + M$[c]		$3.04\ 10^{17}$	−0.65	52,092
10f	$H_2O_2 + M \rightarrow OH + OH + M$[d]	k_0	$7.60\ 10^{30}$	−4.20	25,703
		k_∞	$2.63\ 10^{19}$	−1.27	25,703
11f	$HO_2 + HO_2 \rightarrow H_2O_2 + O_2$		$1.03\ 10^{14}$	0.0	5556
			$1.94\ 10^{11}$	0.0	−709
12f	$HO_2 + H_2 \rightarrow H_2O_2 + H$		$7.80\ 10^{10}$	0.61	12,045

[a] Chaperon efficiencies: H_2 (2.5), H_2O (16.0), CO (1.2), CO_2 (2.4), Ar and He (0.7), and 1.0 for all other species; Troe falloff with $F_c = 0.5$.
[b] Chaperon efficiencies: H_2 (2.5), H_2O (12.0), CO (1.9), CO_2 (3.8), Ar and He (0.4), and 1.0 for all other species.
[c] Chaperon efficiencies: H_2 (2.5), H_2O (12.0), CO (1.9), CO_2 (3.8), Ar and He (0.5), and 1.0 for all other species.

Figure 2.2: On the left, list of twenty reversible elementary reactions among eight reactive species, grouped in four categories reflecting the main role they play in hydrogen combustion. On the right, the skeletal mechanism (Sánchez and Williams, 2014).

and rich) that produce $T'_a = T'_c$, so that the flame cannot longer exist if the maximum temperature achieved remains below crossover. Critical values of the equivalence ratio and the crossover temperature at the lean flammability limit of the steady planar flame are $\phi_l = 0.251$, $(T'_c)_l = 1080$ K for $T'_u = 300$ K and $p' = 1$ atm.

In the configuration at hand under ambient pressure and dilute fuel conditions, the formation of hydrogen peroxide will not be favored and the radical-radical recombination will mainly take place through H_2+O_2+M→HO_2+M (6b). In this way, lean deflagrations could be represented by reversible shuffle reactions (1-3), recombination (4f) and HO_2 consumption (5f, 6f and 7f), a 7-step reduced scheme for lean applications. Furthermore, by applying the steady-state hypothesis for the H-atom radical in the 7-step scheme, a one-step scheme can be derived for reactions near the flammability limit (Fernández-Galisteo et al., 2009). The overall reaction $2H_2$+$O_2 \rightarrow 2H_2O$, can be modeled through the production rate

$$\omega = \omega_{4f} = \frac{1}{GH}\left(\frac{k_{1f}}{\alpha k_{4f} C_{M4}} - 1\right)\frac{k_{2f}k_{3f}}{k_{1f}}C_{\mathrm{H_2}}^2, \tag{2.4}$$

where G is a function depending on the reaction rates k_i and concentrations, while α and H play the role of constants for lean scenarios. Specially, the lean premixed flame structure is composed by: a preheated upstream region (non-reacting); a diffusion-reaction thin layer with negligible effect of convection, and low rates of radicals production-consumption around T'_c (steady-state assumption); and a downstream area dominated by diffusion and convection.

For the sake of simplicity, the reaction rate in the lean flammability limit can be represented by a one-step irreversible Arrhenius law during the following study. Choosing appropriate

thermochemical parameters allows to qualitatively mimic the complex mechanism, although missing some of the aforementioned details. The study of these ultra-lean hydrogen-air flames through this kind of approximation was already explored in Fernández-Galisteo et al., 2009, including values for the activation energy around $E_a/R_g \simeq 20 \times 10^3 K$. Hence, the value of the Zel'dovich number, defined as $\beta = E_a \left(T'_a - T'_u\right) / \left(RT'^2_a\right)$ takes values around $\beta = 10$, considering a temperature jump between adiabatic and unburnt temperatures of the order of $T'_a/T'_u \sim 2-5$, in the range of interest of this study.

Flame instabilities

Freely propagating reactive fronts cannot preserve a planar shape. Curved and wrinkled surfaces are generated by the fast action of intrinsic instabilities, forming corrugated flames. A detailed description of the different types of instabilities acting upon a premixed flame can be found in Williams, 1985 and in Clavin and Searby, 2016. The intrinsic instabilities of premixed flames can be caused by either body-force, hydrodynamic, or diffusive-thermal effects.

First, the body-force effect refers to the fact that a light fluid placed beneath a heavier one is not stable, developing the well-known Rayleigh-Taylor instability. The body forces could be an acceleration or deceleration of the flame front, which, depending on the direction, could be a stabilizing or non-stabilizing effect. In general terms, the severity of the instability is inversely proportional to the speed of propagation. For decelerating flames, downward propagation, and burner-stabilized flames with the flow moving upward, the body-force effects are stabilizing.

The hydrodynamic Darrieus-Landau instability is produced by the action of the density jump between the burnt and unburnt sides of the flame front. Therefore, the planar deflagration is unconditionally unstable. The direct way to study the case is by modeling the flame as a density discontinuity, introducing a small perturbation to the flame shape of wavelengths much larger than the flame thickness. It is seen that in the convex part (pointing at the fresh mixture) the extra flow expansion of the hot gases pushes the flame front, creating an extra acceleration forward, refeeding the wrinkling process.

Finally, the thermo-diffusive instability promotes the appearance of corrugated fronts due to the unequal species and thermo-diffusive coefficients. This unbalance creates regions of the field where either temperature or species accumulate, giving rise, in turn, to a reinforcement/weakening of the combustion process. The latter causes certain regions of the front to spread faster than others, promoting the corrugation of the front. As already mentioned above, the low Lewis number of the lean-premixed H_2 flames promotes this type of instabilities via differential diffusion.

Figure 2.3 displays various cases from the numerical study in Martínez-Ruiz et al., 2019. Flame fronts in Hele-Shaw chambers can undergo different propagation regimes. On the top row, where Le = 1, a continuous front gaining certain curvature (Darrieus-Landau) weakens while increasing conductive heat losses through parameter b. On the bottom row, case Le = 0.3 presents fragmented fronts. Isolated fronts are characterized by a higher curvature, and higher temperature peaks in comparison to the continuous one. A noticeable change in order

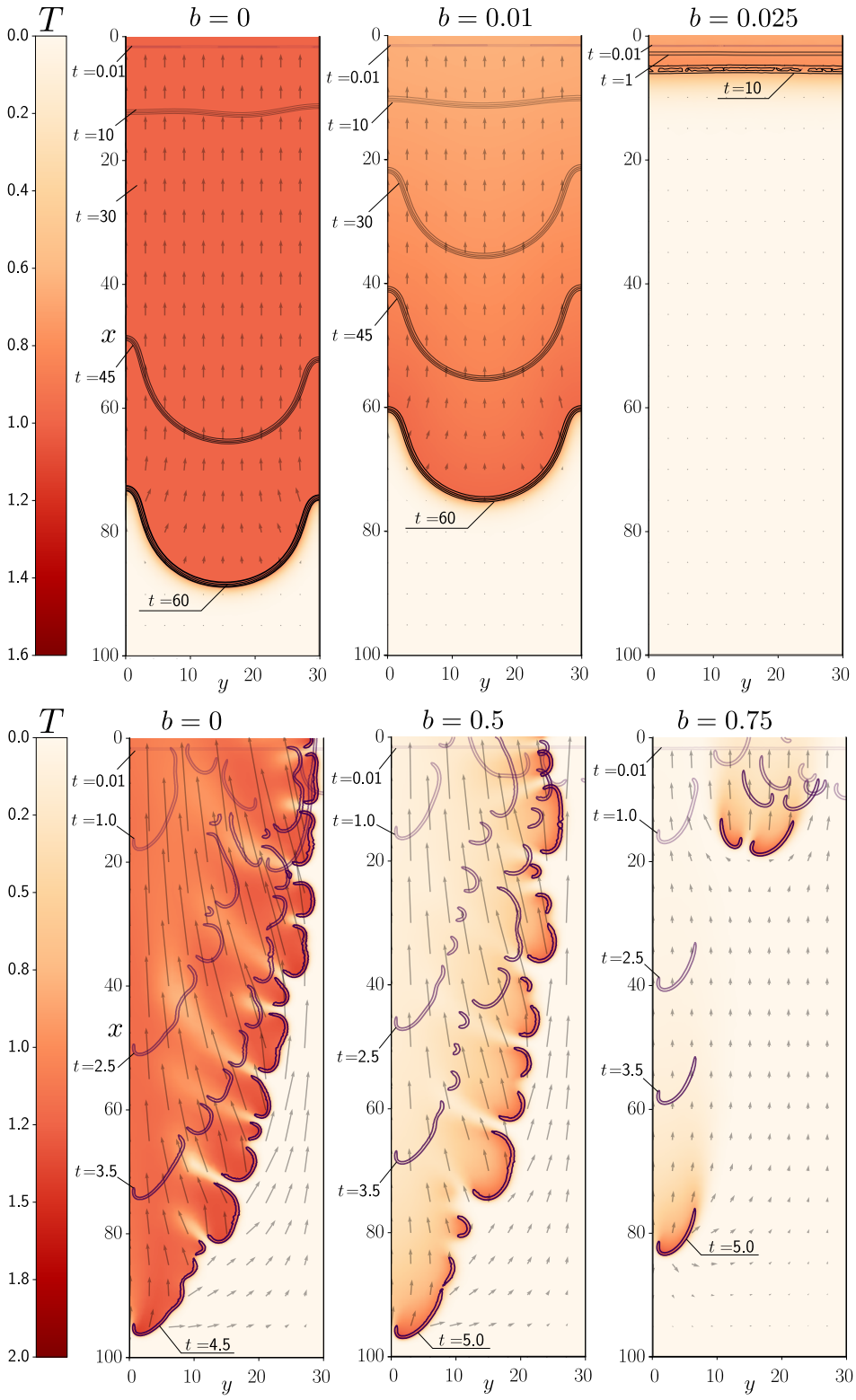

Figure 2.3: Flame propagation behavior. Le = 1 (left) with variation of heat losses parameter $b = [0,\ 0.01,\ 0.025]$, and Le = 0.3 (right) for $b = [0,\ 0.5,\ 0.75]$. Reproduced from Martínez-Ruiz et al., 2019.

of magnitude is observed for the b values leading to extinction. The enhanced combustion process of the second case (thermo-diffusive) results in a greater capacity to sustain heat losses.

2.1.2 Characteristic scales

The isolated flame kernels propagating in narrow channels are the result of combined geometrical and combustion effects that can be addressed through a preliminary analysis, later extended in chapter 6. First, the main characteristic length-scale introduced by the Hele-Shaw chamber is the height of the channel h'. The gap between the plates is small compared to the characteristic lengths of the plates $h' \ll L'$, therefore, a narrow channel is formed and a confinement effect appears, applied to the transversal direction. The confinement effect brings into play two consequences to the fluid enclosed in the chamber: major conductive heat losses through the walls, which act as heat sinks; and the dominance of viscous terms in the transverse direction. Moreover, regarding the flame structure, two more characteristic scales can be identified: the reference velocity given by the chemical kinetics for the planar laminar flame construct S'_L, and the flame thickness which typically scales as $\delta'_T \simeq D'_T/S'_L$. Therefore, the non-dimensional characteristic size of the isolated kernel is $\delta_k = \delta'_k/\delta'_T$, which moves with a propagation speed of the whole cohesive structure, $S_u = S'_u/S'_L$, referred to the characteristic planar flame speed.

In order to extract the relevance of the main physical mechanisms, the different characteristic times involved in the conservation equations should be compared. The typical diffusion time of the flame structure relates to the thermal diffusivity and flame thickness as $t'_{\text{diff}} \sim \delta'^2_T/D'_T$. In turn, the characteristic residence time of the isolated flame structures can be estimated as,

$$t'_{\text{r}} \sim \frac{\delta'_k}{S'_u} = \frac{\delta_k}{S_u}\frac{\delta'_T}{S'_L} \simeq \frac{\delta_k}{S_u} t'_{\text{diff}}, \tag{2.5}$$

such that the time of propagation over a distance of its own size is comparable to the diffusion time when $\delta_k/S_u \sim \mathcal{O}(1)$, as it will be confirmed below. In addition, the inner flame region enables the scaling of the reaction thickness as $\delta_r = \delta_T/\beta$, inversely proportional to the dimensionless activation energy prescribed by the Zel'dovich number β. The production term, defines the shortest time of the problem at hand, namely the chemical time $t'_{\text{ch}} \sim \mathcal{O}(1/\beta^2) t'_{\text{diff}}$, extracted from the reaction-diffusion layer. Finally, the characteristic heat-loss term arises from the transversal conduction of heat to the plates,

$$t'_{\text{cond}} \sim h'^2/D'_T \simeq \frac{h'^2}{\delta'^2_T} t'_{\text{diff}}, \tag{2.6}$$

which will be controlled by the relative size of channel gap to flame thickness. Moreover, the heat lost to the environment, infinite sink at temperature T'_u, through the plates is proportional to the hot contact area of the flame kernel with the walls $A \sim \mathcal{O}(\delta'^2_k)$. Fourier's law for heat conduction indicates that the total amount of heat transferred during the passing of the flame scales as

$$\int \left(\int \dot{q}_k \mathrm{d}A \right) \mathrm{d}t' \sim \rho' c_p D'_T \frac{(T'_a - T'_u)}{h'} A' t'_{\text{r}} \simeq \rho' c_p \frac{(T'_a - T'_u)}{h'} \delta'^3_k \delta'^2_T \frac{S'_L}{S'_u}. \tag{2.7}$$

This quantity must relate to the heat release produced at the flame, which is proportional to its surface. In this case, the total amount of heat production in the combustion process at the reaction-diffusion layer of volume $\mathrm{dVol_f} \sim \mathcal{O}(h'\delta_k'\delta_T')$ can be related to the enthalpy change ΔH

$$\int \left(\int Q\omega \mathrm{dVol_f} \right) \mathrm{d}t' \sim \mathrm{dVol_f} \Delta H \simeq \rho' c_p \left(T_a' - T_u' \right) \delta_k' h' \delta_T'. \tag{2.8}$$

Given a fixed channel gap, an increase in the isolated flame structure size δ_k', causes an increase in conductive heat losses $\propto \delta_k'^3$ while the heat release scales as $\propto \delta_k'$. Therefore, a global energy balance limits the maximum size above which it would be difficult for the flame kernel to survive due to the large losses. Contrarily, for a fixed kernel size and increasing the gap between plates h', the heat loss effect decreases $\propto 1/h'$ while the heat released must increase $\propto h'$, at the same time that the confinement effect is progressively lost and three-dimensional effects take place, ruling out the feasibility of nearly two-dimensional flame structures. Finally, the decrease of the narrow channel gap size h' brings the system closer to the quenching distance, the minimum plate separation for which the flame propagation can be granted.

2.2 Flow hypotheses

All the preliminary concepts and scales presented in this chapter lead to the following assumptions that will simplify the detailed analysis and results offered throughout this work. The main relevant hypotheses are:

- **Very narrow channel.** The length-scale difference between the in-plane coordinates and the transverse one, is not only reduced to a geometrical constraint of the gap between the plates that form the chamber. To ensure a viscous flow the effective Reynolds number must be small or moderate,

  $$\mathrm{Re_{eff}} = \frac{\rho' S_L' h'}{\mu} = \frac{1}{\mathrm{Pr}} \frac{h'}{\delta_T'} \lesssim 1.$$

  Considering that the Prandtl number is of order unity, the controlling dimensionless parameter h/δ_T must not be much larger than unity. This is the narrow channel approximation, responsible for the future simplification of the three-dimensional problem to a quasi-two-dimensional formulation.

- **Low Mach propagation.** The flame propagation speed and the induced flow velocity are expected to be small in comparison to the speed of sound $c' = \sqrt{\gamma R_g T'}$. Therefore, the Mach number must remain small, $\mathrm{M} = S_L'/c' \ll 1$. Compressibility is thus neglected, being the variation of hydrodynamic pressure small in comparison to the thermodynamic base value. Decomposing the total pressure into the thermodynamic and hydrodynamic contributions $p' = P' + p_h' \simeq \rho' R_g T' + \rho' S_L'^2$, it can be brought to our attention that

  $$\frac{p'}{\rho' R_g T'} \sim 1 + \gamma M^2 \tag{2.9}$$

  Therefore, the base pressure is kept constant at the equation of state in the Hele-Shaw chamber open to the atmosphere. Nevertheless, the hydrodynamic contribution is retained for pressure gradient variations in the momentum equation.

- **Fuel-lean mixture**. The cases under study correspond to ultra-lean premixed mixtures. During the combustion process, the deficient fuel reactant is completely consumed while the oxidizer species is considered to practically remain unaffected. In this limit, the reaction rate mainly depends on the deficient reactant concentration, and only its species conservation equation must be solved.

Chapter 3

Mathematical formulation

The configuration selected for the fundamental analysis of lean H_2 deflagrations involves a particular disparity of geometrical scales, with narrow channels that are formed by gaps of height h' much smaller than the characteristic plate size L'. Therefore, the complete Navier-Stokes equations are consistently reduced to represent quasi-two-dimensional problems, as follows from Fernández-Galisteo et al., 2018 and Martínez-Ruiz et al., 2019. The model is already known to reproduce the characteristic dynamics of the flame kernels under study, as observed in Veiga-López, Kuznetsov, et al., 2020. In particular, thermo-diffusive effects and conductive heat losses at the walls remain as key mechanisms controlling the formation of isolated flame structures.

3.1 Reactive Navier-Stokes equations

The starting point of the formulation is the set of reactive low-Mach Navier-Stokes equations. Following the continuous media hypothesis, the solution can be described by the classical flow variables, density, temperature, pressure, mass species concentration and velocity field $[\rho',\ T',\ p',\ Y_i,\ \mathbf{v}']$ respectively, where the prime superscript is used in this section to denote dimensional values as a function of the time variable t' and space coordinates $[x', y']$. Three-dimensional mass, momentum, energy and species conservation equations are written as

$$\frac{\partial \rho'}{\partial t'} + \nabla \cdot (\rho' \mathbf{v}') = 0, \tag{3.1}$$

$$\rho' \frac{\partial \mathbf{v}'}{\partial t'} + \rho' \mathbf{v}' \cdot \nabla \mathbf{v}' = -\nabla p' + \nabla \cdot (\tau') + \rho' \mathbf{f_m}, \tag{3.2}$$

$$\rho' c_p \frac{\partial T'}{\partial t'} + \rho' c_p \mathbf{v}' \cdot \nabla T' = \nabla \cdot (\lambda \nabla T') + Q \omega_F, \tag{3.3}$$

$$\rho' \frac{\partial Y_i}{\partial t'} + \rho' \mathbf{v}' \cdot \nabla Y_i = \nabla \cdot (\mathbf{j_i'}) - \omega_i, \tag{3.4}$$

with τ' the viscous stress tensor, c_p for the specific heat capacity, $\lambda = \rho' c_p D_T'$ the thermal conductivity, Q the heat release per unit mass of fuel burnt, ω_i the consumption/production rate and $\mathbf{j_i'}$ the diffusive flux vector of the species i. An additional relation is used, the equation

of state for ideal gases

$$p' = \rho' R_g T', \tag{3.5}$$

with R_g the gas constant. The chemical reaction, ν_F fuel$+\nu_O$ oxidizer $\rightarrow \nu_P$products$+$(heat), where ν_i is the stoichiometric coefficient of each species, is modeled using a simplified one-step Arrhenius irreversible scheme

$$\omega_F = B C_F C_O \exp\left(-\frac{E_a}{R_g T'}\right), \tag{3.6}$$

where B is the pre-exponential frequency factor, $C_{F,O}$ the species concentration and E_a the activation energy required to trigger the reaction. In the limit of a very lean flame, it becomes dependent only on the species concentration of the deficient reactant, while the amount of oxidizer remains nearly unmodified, $C_O \simeq C_{O_0}$, and, thus, its species conservation equation is not further considered.

The integration of the set of equations involves the use of an appropriate set of boundary conditions. In general terms, the boundary conditions for the in-plane coordinates can define the infinitely far region of the flow, and in the transverse $z-$direction, describe the interaction between the premixed gas and the walls. In particular, the solid-wall heat equation should be included to solve the temperature evolution at the plates

$$\rho'_w c_w \frac{\partial T'_w}{\partial t'} - \nabla \cdot (\lambda_w \nabla T'_w) = 0, \tag{3.7}$$

where the subscript $-w-$ is used from here on in reference to solid walls properties.

3.1.1 Dimensionless equations

An ideal infinite domain along the in-plane coordinates does not provide a characteristic geometrical length for the in-plane coordinates $[x', y']$. The flow variables are expected to vary in lengths of the order of the flame thickness $\delta'_T = D'_{T_u}/S'_L$ (the preheated length), where D'_{T_u} is the aforementioned thermal diffusion coefficient of the fresh mixture and S'_L the in-plane reference propagation speed, given by the planar adiabatic flame. Therefore, the dimensionless scaling for these two coordinates is $[x, y] = [x'/\delta'_T,\ y'/\delta'_T]$. However, for the transverse spatial coordinate the dominant characteristic length is the channel height, so that $z = z'/h'$ becomes the arguable choice. Finally, the dimensionless time is defined as $t = t'/\left(\delta'_T/S'_L\right)$.

Regarding the flow variables, the non-dimensional in-plane gas velocity components are $[v_x, v_y] = [v'_x/S'_L,\ v'_y/S'_L]$. In turn, the continuity equation indicates that the appropriate velocity scale for the $z-$coordinate is $v'_z \sim S'_L h'/\delta'_T$, where the new parameter $a = h'/\delta'_T$, relating the gap between the plates and the flame thickness, arises. Therefore, the transverse component of the flow velocity reads $v_z = (v'_z/S'_L)/a$. The thermodynamic quantities are referred to their unburnt values, generally denoted by a subscript $-u-$ along the document. Then, the non-dimensional density is $\rho = \rho'/\rho'_u$, and the deficient fuel species is rescaled with the unburnt mass fraction $Y = Y_F/Y_{F_u}$. The dimensionless temperature value, $T =$

$(T' - T'_u)/(T'_a - T'_u)$ involves the adiabatic flame temperature, defined as $T'_a = T'_u(1+q)$ use made of the dimensionless heat release

$$q = \frac{(T'_a - T'_u)}{T'_u} = \frac{QY_{F_u}}{c_p T'_u}. \tag{3.8}$$

Next, the set of dimensionless equations can be reduced in terms of the main flow hypotheses. First, continuity reads

$$\frac{\partial \rho}{\partial t} + \frac{\partial(\rho v_x)}{\partial x} + \frac{\partial(\rho v_y)}{\partial y} + \frac{\partial(\rho v_z)}{\partial z} = 0. \tag{3.9}$$

The vectorial dimensionless momentum equation can be written as,

$$\rho\left[\frac{\partial v_x}{\partial t} + v_x\frac{\partial v_x}{\partial x} + v_y\frac{\partial v_x}{\partial y} + v_z\frac{\partial v_x}{\partial z}\right] = -\frac{1}{a^2}\frac{\partial p}{\partial x} + \mathrm{Pr}\left[\frac{\partial \tau_{xx}}{\partial x} + \frac{\partial \tau_{xy}}{\partial y} + \frac{1}{a}\frac{\partial \tau_{xz}}{\partial z}\right] \pm \frac{\rho G}{a^2}, \tag{3.10}$$

$$\rho\left[\frac{\partial v_y}{\partial t} + v_x\frac{\partial v_y}{\partial x} + v_y\frac{\partial v_y}{\partial y} + v_z\frac{\partial v_y}{\partial z}\right] = -\frac{1}{a^2}\frac{\partial p}{\partial y} + \mathrm{Pr}\left[\frac{\partial \tau_{yx}}{\partial x} + \frac{\partial \tau_{yy}}{\partial y} + \frac{1}{a}\frac{\partial \tau_{yz}}{\partial z}\right], \tag{3.11}$$

$$\rho\left[\frac{\partial v_z}{\partial t} + v_x\frac{\partial v_z}{\partial x} + v_y\frac{\partial v_z}{\partial y} + v_z\frac{\partial v_z}{\partial z}\right] = -\frac{1}{a^4}\frac{\partial p}{\partial y} + \frac{\mathrm{Pr}}{a}\left[\frac{\partial \tau_{zx}}{\partial x} + \frac{\partial \tau_{zy}}{\partial y} + \frac{1}{a}\frac{\partial \tau_{zz}}{\partial z}\right] \tag{3.12}$$

with the non-dimensional Prandtl number defined as $\mathrm{Pr} = \nu'_u/D'_{Tu} \simeq 0.7$. The different components for the viscous tensor involve the constitutive relations for the dynamic viscosity coefficient $\mu = \mu'/\mu'_u$. The pressure distribution, in the low-Mach limit, involves small variations provided by the dominant terms in viscous flow $\Delta p' \sim \rho' S_L^2/a^2$, and a much larger constant thermodynamic value $P' \simeq \rho'_u R_g T'_u$. Therefore, the momentum equation involves the gradient of dimensionless pressure $p = p'/(\rho'_u S_L^2/a^2)$, where we anticipate that it will balance viscous terms of order $\sim \mathcal{O}(a^{-2})$ to scale it consistently. As a result, the non-dimensional state equation yields a nearly isobaric behavior

$$\rho(1+qT) = 1 + \gamma\left(\frac{\mathrm{M}}{a}\right)^2 p \simeq 1, \tag{3.13}$$

whenever the Mach number related to the planar-flame speed is small, $M \ll a$. Finally, buoyancy forces are considered to apply in the $x-$direction, controlled by the non-dimensional term $G = ga^2\delta'_T/S'^2_L$ that involves the gravitational constant g. This effect may be considered for Hele-Shaw chambers in a non-horizontal position.

Next, analogous rescaling of the energy equation expressed in non-dimensional form reads

$$\begin{aligned}
&\rho\left[\frac{\partial T}{\partial t} + v_x\frac{\partial T}{\partial x} + v_y\frac{\partial T}{\partial y} + v_z\frac{\partial T}{\partial z}\right] \\
&= \frac{\gamma-1}{q}\left[\frac{1}{\gamma}\frac{\partial P}{\partial t} + \left(\frac{\mathrm{M}}{a}\right)^2\left(\Phi_\nu \mathrm{Pr} + \frac{\partial p}{\partial t} + v_x\frac{\partial p}{\partial x} + v_y\frac{\partial p}{\partial y} + v_z\frac{\partial p}{\partial z}\right)\right] \\
&+ \frac{\partial}{\partial x}\left(\rho D_T\frac{\partial T}{\partial x}\right) + \frac{\partial}{\partial y}\left(\rho D_T\frac{\partial T}{\partial y}\right) + \frac{1}{a^2}\frac{\partial}{\partial z}\left(\rho D_T\frac{\partial T}{\partial z}\right) + \Omega
\end{aligned} \tag{3.14}$$

where $D_T = D'_T/D'_{Tu}$, and Φ_ν is Rayleigh's viscous dissipation, typically negligible in low-Mach conditions together with pressure work terms. Finally, the non-dimensional production rate is written as

$$\Omega = \frac{\delta'_T}{S'_L}\frac{\omega_F Q}{\rho'_u c_p \left(T'_a - T'_u\right)}. \tag{3.15}$$

The concentrations of species included in ω_F can be rewritten in terms of the respective mass fractions as $C_{F,O} = \rho' Y_{F,O}/\mathcal{M}_{F,O}$, and the exponential dependence on temperature can be expressed as

$$\exp\left(-\frac{E_a}{R_g T'}\right) = \exp\left(-\frac{E_a}{R_g T'_a}\right)\exp\left(\frac{\beta\left(T-1\right)}{1+\frac{q}{1+q}\left(T-1\right)}\right),$$

where $\beta = E_a\left(T'_a - T'_u\right)/\left(R_g T'^2_a\right)$ is the effective Zel'dovich number. In addition, the reaction rate can be referred to the planar adiabatic problem and, thus, the propagation speed $s_L = S_L/\left(S_L\right)_a = 1.05$ arises as the eigenvalue of that case, referred to the propagation velocity for infinitely-large activation energy,

$$\left(S_L\right)_a^2 = 2Y_b B\rho_b D_{Tb}\nu_O \frac{\mathrm{Le}_O \mathrm{Le}_F}{\mathcal{M}_F \beta^3}\left(1+\Gamma\right)\left(\frac{\rho_b}{\rho_u}\right)^2 \exp\left(-\frac{E_a}{R_g T'_a}\right), \tag{3.16}$$

where an effective Lewis number can be defined as $\mathrm{Le} = \mathrm{Le}_F \mathrm{Le}_O^{\frac{1+\Gamma}{\beta}}$. Finally, the low concentration of fuel in lean mixtures implies that small amounts of oxidizer must be consumed, while the characteristic dominant N_2 species in air remains effectively unaltered. Therefore, the evolution of the reaction can be adequately represented through the consumption of the deficient reactant, be H_2 in the study at hand. These considerations help rewrite eq. (3.15) for the dimensionless form of the reaction rate,

$$\Omega = \rho^2\beta^2\left(1+q\right)\frac{Y}{2s_L^2 \mathrm{Le}}\exp\left(\frac{\beta\left(T-1\right)}{1+\frac{q}{1+q}\left(T-1\right)}\right). \tag{3.17}$$

Last, the species concentration equation for the deficient reactant must be solved to enable the calculation of the reduced chemical kinetics selected above,

$$\begin{aligned}&\rho\left[\frac{\partial Y}{\partial t} + v_x\frac{\partial Y}{\partial x} + v_y\frac{\partial Y}{\partial y} + v_z\frac{\partial Y}{\partial z}\right]\\ &= \frac{1}{\mathrm{Le}}\left[\frac{\partial}{\partial x}\left(\rho D\frac{\partial Y}{\partial x}\right) + \frac{\partial}{\partial y}\left(\rho D\frac{\partial Y}{\partial y}\right) + \frac{1}{a^2}\frac{\partial}{\partial z}\left(\rho D\frac{\partial Y}{\partial z}\right)\right] - \Omega.\end{aligned} \tag{3.18}$$

In writing the latter, Fick's law is employed to relate the diffusive velocity to the species gradient through the binary diffusion coefficient $D = D'_i/D'_{i_u}$. Additionally, we shall consider that the Lewis number $\mathrm{Le} = D_{T'_u}/D'_{i_u}$ is equivalent to the effective value introduced above. For a more complex representation of the diffusion velocity, the Stefan-Maxwell theory could be used including the dependence on the temperature gradient or other mass forces.

The boundary conditions for the set of equations in the ideal case of the reactive gas contained between two infinite plates, result as the following expressions in $z-$direction,

$$\left.\frac{\partial Y}{\partial z}\right|_{z=0,1} = 0,\ \left.\frac{\partial T}{\partial z} = \frac{\lambda_w}{\lambda_u}\frac{\partial T_w}{\partial z}\right|_{z=0,1},\ T_w = T|_{z=0,1},\ \left.\mathbf{v}\right|_{z=0,1} = 0, \tag{3.19}$$

respectively, non-permeable walls to mass diffusion of species, heat flux and temperature continuity between the gas and the wall surface, and no-slip kinematic condition for the velocity field.

Finally, the non-dimensional heat equation for the solid walls of thickness h'_w and thermal conductivity λ_w, with the aforementioned dimensionless variables,

$$\frac{\rho_w c_w}{\rho_u c_p}\frac{\partial T_w}{\partial t} + \frac{\partial}{\partial x}\left(\frac{\lambda_w}{\lambda_u}\frac{\partial T_w}{\partial x}\right) + \frac{\partial}{\partial y}\left(\frac{\lambda_w}{\lambda_u}\frac{\partial T_w}{\partial y}\right) + \frac{1}{a^2}\frac{\partial}{\partial z}\left(\frac{\lambda_w}{\lambda_u}\frac{\partial T_w}{\partial z}\right) = 0, \tag{3.20}$$

should be solved together with the reactive flow system. The additional boundary conditions required on the exterior surface of the plates consider the temperature match with the infinite-sink ambient conditions, equal to the unburnt gas temperature T'_u,

$$T_w|_{z=-h'_w/h',\, 1+h'_w/h'} = 0. \tag{3.21}$$

3.1.2 Quasi-two-dimensional limit

In this section, we shall analyze the very-narrow-channel limit, to justify the mathematical reduction to a quasi-2D model in which the first-order variables represent the integrated average of these magnitudes across the coordinate z. Theoretically, it should be considered that the dimensionless parameter a is moderate or small, such that the thickness of the channel gap effectively imposes a viscous flow and dominant diffusive effects in the transverse direction. This nearly-planar solution has been shown to remain valid when put in contrast with three-dimensional simulations for small to moderate values of $a \simeq 1$, (Melguizo-Gavilanes et al., 2021).

First, in the low-Mach limit $\mathrm{M}/a \ll 1$, the hydrodynamic pressure variations are much smaller than the thermodynamic contribution. The latter, can be treated as a constant since the Hele-Shaw chamber is considered to be infinite (open to the atmosphere at a far end), which gives rise to the quasi-isobaric form of the equation of state, $\rho\,(1 + qT) = 1$. Moreover, the pressure work terms of eq. (3.14) are consistently neglected. Regarding the dimensionless conservation equations, the flow field variables $\mathbf{\Phi} = [\rho,\ T,\ Y,\ p,\ \mathbf{v}]$ can be expressed through an expansion series over the small parameter a, of the form

$$\mathbf{\Phi} = \mathbf{\Phi}_0 + a^2\mathbf{\Phi}_1 + \mathcal{O}(a^4). \tag{3.22}$$

The expanded variables can readily be plugged into the conservation equations, where first-order terms are easily identified for small values of a. The energy equation terms are here presented to illustrate this fact, separating the contributions to different orders

$$
\begin{aligned}
\sim \mathcal{O}\left(\frac{1}{a^2}\right): \quad & \frac{1}{a^2}\frac{\partial}{\partial z}\left(\rho_0 D_T \frac{\partial T_0}{\partial z}\right) \\
\sim \mathcal{O}\left(1\right): \quad & -\rho_0\left[\frac{\partial T_0}{\partial t} + v_{x0}\frac{\partial T_0}{\partial x} + v_{y0}\frac{\partial T_0}{\partial y} + v_{z0}\frac{\partial T_0}{\partial z}\right] \\
& + \frac{\partial}{\partial z}\left(\rho_0 D_T \frac{\partial T_1}{\partial y}\right) + \frac{\partial}{\partial x}\left(\rho_0 D_T \frac{\partial T_0}{\partial x}\right) + \frac{\partial}{\partial y}\left(\rho_0 D_T \frac{\partial T_0}{\partial y}\right) + \Omega \\
\sim \mathcal{O}\left(a^2\right): \quad & -a^2\rho_1\left[\frac{\partial T_0}{\partial t} + v_{x0}\frac{\partial T_0}{\partial x} + v_{y0}\frac{\partial T_0}{\partial y} + v_{z0}\frac{\partial T_0}{\partial z}\right] \\
& -a^2\rho_0\left[\frac{\partial T_1}{\partial t} + v_{x1}\frac{\partial T_0}{\partial x} + v_{x0}\frac{\partial T_1}{\partial x} + v_{y1}\frac{\partial T_0}{\partial y} + v_{y0}\frac{\partial T_1}{\partial y} + v_{z1}\frac{\partial T_0}{\partial z} + v_{z0}\frac{\partial T_1}{\partial z}\right] \\
& + a^2\frac{\partial}{\partial x}\left(\rho_0 D_T \frac{\partial T_1}{\partial x} + \rho_1 D_T \frac{\partial T_0}{\partial x}\right) + a^2\frac{\partial}{\partial y}\left(\rho_0 D_T \frac{\partial T_1}{\partial y} + \rho_1 D_T \frac{\partial T_0}{\partial y}\right)
\end{aligned}
\tag{3.23}
$$

A quick inspection of the different resulting terms shows that the first-order analysis involves isolated second derivatives in the z-direction. Besides the energy conservation equation, this character is also found at the species conservation and solid heat transfer equations. Therefore, as a first-order approximation,

$$
\frac{\partial}{\partial z}\left(\rho_0 D_T \frac{\partial T_0}{\partial z}\right) = \frac{\partial}{\partial z}\left(\rho_0 D_i \frac{\partial Y_0}{\partial z}\right) = \frac{\partial}{\partial z}\left(\frac{\lambda_w}{\lambda_u}\frac{\partial T_{w\,0}}{\partial z}\right) = 0. \tag{3.24}
$$

Imposing the boundary conditions shown in (3.19), constant first-order profiles of species and gas temperature in the transverse coordinate $T_0 = T_0\left(x, y; t\right)$, $Y_0 = Y_0\left(x, y; t\right)$ are obtained. For the wall temperature profile, the plates are considered thermally-thin, where the characteristic heating time is small and the temperature profile instantly adapts to the boundary conditions given by the channel flow. Linear distributions between the inner surfaces at $T_{w\,0} = T_0$ and the outer surfaces at $T_{w\,0} = 0$ are thus found,

$$
\text{Upper plate: } T_{w0} = \left(\frac{h'}{h'_w}\left(1 - z\right) + 1\right)T, \quad \text{for} \quad 1 < z < 1 + h'_w/h', \tag{3.25}
$$

$$
\text{Bottom plate: } T_{w0} = \left(\frac{h'}{h'_w}z + 1\right)T, \quad \text{for} \quad -h'_w/h' > z > 0. \tag{3.26}
$$

Furthermore, the first-order terms of the different components of the momentum conservation equation show supplementary information on the pressure and velocity fields. Starting with the higher-order term, the z-direction momentum component implies that

$$
0 = -\frac{1}{a^4}\frac{\partial p_0}{\partial z}, \tag{3.27}
$$

yielding a dynamic pressure field $p_0 = p_0\left(x, y; t\right)$ which does not depend on the transverse coordinate. Momentum equations for the in-plane coordinates can be analogously reduced to

the leading-order terms of the order of $\sim \mathcal{O}(a^{-2})$,

$$0 = -\frac{\partial p_0}{\partial x} + \mathrm{Pr}\frac{\partial}{\partial z}\left(\mu\frac{\partial v_{x0}}{\partial z}\right) \pm \rho_0 G, \tag{3.28}$$

$$0 = -\frac{\partial p_0}{\partial y} + \mathrm{Pr}\frac{\partial}{\partial z}\left(\mu\frac{\partial v_{y0}}{\partial z}\right), \tag{3.29}$$

corresponding to the viscosity-dominant momentum equations. Hence, parabolic Poiseuille profiles for the in-plane velocity components are obtained through their integration (Kurdyumov and Matalon, 2013), yielding

$$v_{x0} = \frac{A_x}{2} z\,(z-1)\,; \quad v_{y0} = \frac{A_y}{2} z\,(z-1) \tag{3.30}$$

where A_i are integration constants to be determined. Nevertheless, we shall define the volumetric flux per unit line as the transverse-direction velocity integrals $u_x = \int_0^1 v_{x0} dx$, and $u_y = \int_0^1 v_{y0} dy$, which implies that $[A_x,\ A_y] = [-12u_x, -12u_y]$. As a result, the original dimensionless components can be rewritten as $v_{x0} = -6u_x z\,(z-1)$ and $v_{y0} = -6u_y z\,(z-1)$. Additionally, a consistent rescaling of the pressure variable, $p = (p' - P')\,/\left(12\mathrm{Pr}\rho'_u S'^2_L/a^2\right)$, allows to write the simplified version of momentum equation upon incorporation of the velocity profiles,

$$u_x = \frac{1}{\mu}\left(-\frac{\partial p_0}{\partial x} \pm \rho_0 G\right); \quad u_y = -\frac{1}{\mu}\frac{\partial p_0}{\partial y}, \tag{3.31}$$

with analogous rescaling of the gravitational effect $G = ga^2\delta'_T/\left(12\mathrm{Pr}S'^2_L\right)$, with $G > 0$ for upward and $G < 0$ for downward flame movement.

All things considered, the following order ($\sim \mathcal{O}(1)$) of continuity, energy and species equations (second group of terms at the sample energy eq. (3.23)) involve the $\Phi_0(x, y; t)$ profiles, which are not a function of the transverse coordinate

$$\frac{\partial \rho_0}{\partial t} + \frac{\partial}{\partial x}(\rho_0 u_x) + \frac{\partial}{\partial y}(\rho_0 u_y) = 0 \tag{3.32}$$

$$\rho_0\frac{\partial T_0}{\partial t} + \rho_0 u_x\frac{\partial T_0}{\partial x} + \rho_0 u_y\frac{\partial T_0}{\partial y} = \frac{\partial}{\partial x}\left(\rho D_T\frac{\partial T_0}{\partial x}\right) + \frac{\partial}{\partial y}\left(\rho D_T\frac{\partial T_0}{\partial y}\right) + \frac{\partial}{\partial z}\left(\rho D_T\frac{\partial T_1}{\partial z}\right) + \Omega \tag{3.33}$$

$$\rho_0\frac{\partial Y_0}{\partial t} + \rho_0 u_x\frac{\partial Y_0}{\partial x} + \rho_0 u_y\frac{\partial Y_0}{\partial y} = \frac{\partial}{\partial x}\left(\frac{\rho D_T}{\mathrm{Le}}\frac{\partial Y_0}{\partial x}\right) + \frac{\partial}{\partial y}\left(\frac{\rho D_T}{\mathrm{Le}}\frac{\partial Y_0}{\partial y}\right) + \frac{\partial}{\partial z}\left(\frac{\rho D_T}{\mathrm{Le}}\frac{\partial Y_1}{\partial z}\right) - \Omega, \tag{3.34}$$

and can be integrated between $z \in [0, 1]$. The first integral of the remaining transverse diffusive term in the energy eq. (3.33) can be equated to the heat flux through the wall, $\lambda_u a^2 \partial T_1/\partial z = \lambda_w \partial T_{w\,0}/\partial z$. Therefore, it can be replaced by the integral conductive heat-loss effect at the thermally-thin solid plates,

$$\left.\frac{\partial T_1}{\partial z}\right|_0^1 = \frac{1}{a^2}\frac{\lambda_w}{\lambda_u}\left.\frac{\partial T_w}{\partial z}\right|_0^1 = -2\frac{1}{a^2}\frac{h}{h_w}\frac{\lambda_w}{\lambda_u}T = -bT, \tag{3.35}$$

where a new parameter that will be key in the following study is defined,

$$b = \frac{2}{a^2}\frac{h}{h_w}\frac{\lambda_w}{\lambda_u},$$

namely the conductive heat-loss parameter that contains the combined effects of gap-to-wall thickness relation and relative heat conductivity of the gas and the wall material. The conductive heat losses to the solid walls act as a sink term proportional to the gas temperature through b. The parameter not only collects information on the conductivity gas-solid ratio, and height quotient, but also the aspect ratio between channel height and flame width a. A change in the value of b parameter can be achieved by means of a change in the material of the plates, their separation or a change in flame configuration. Specially, it relates the relative heat loss with respect to the heat generation in the volume of the channel. Regarding the species equation, the analogous substitution of the $z-$integrated transverse diffusive term vanishes owing to the null species flux to the walls $\int_0^1 (\partial Y_1/\partial z)\, dz = 0$.

Ultimately, the dimensionless diffusive transport coefficients are set to a constant value following $\mu = \rho D_T = \rho D = 1$, which is fairly imposed in the ultra-lean limit at hand with well-bounded temperature increase. The resulting quasi-two-dimensional ($z-$averaged) governing equations are presented here,

$$\frac{\partial \rho}{\partial t} + \frac{\partial \rho u_x}{\partial x} + \frac{\partial \rho u_y}{\partial y} = 0, \tag{3.36}$$

$$\rho\left(\frac{\partial T}{\partial t} + u_x\frac{\partial T}{\partial x} + u_y\frac{\partial T}{\partial y}\right) = \frac{\partial^2 T}{\partial x^2} + \frac{\partial^2 T}{\partial y^2} - bT + \Omega, \tag{3.37}$$

$$\rho\left(\frac{\partial Y}{\partial t} + u_x\frac{\partial Y}{\partial x} + u_y\frac{\partial Y}{\partial y}\right) = \frac{1}{\mathrm{Le}}\left(\frac{\partial^2 Y}{\partial x^2} + \frac{\partial^2 Y}{\partial y^2}\right) - \Omega, \tag{3.38}$$

$$u_x = -\frac{\partial p}{\partial x} + \rho G, \tag{3.39}$$

$$u_y = -\frac{\partial p}{\partial y}, \tag{3.40}$$

$$\rho\,(1 + qT) = 1 \tag{3.41}$$

where the subscript $-0-$ is dropped hereafter for the sake of simplicity to note the first-order solution of the in-plane variables.

Making use of the viscous-dominant momentum eqs. (3.39) and (3.40), which act as ligatures of the pressure gradient with the averaged velocity components, the Laplacian of pressure can be composed via the divergence of velocity. Introducing the eq. of state and continuity, an isolated expression for the pressure variable can be written

$$\nabla^2 p = -q\left(\nabla^2 T + \Omega - bT\right) + \frac{\partial \rho}{\partial x} G. \tag{3.42}$$

This is a Poisson equation, that adjusts the pressure profile instantaneously to the local thermal expansion of the flow in the low-Mach and very narrow channel limits. Hence, the problem defined by the set of equations is solved by the resolution of the equations of energy (3.37), species (3.38) and pressure (3.42), while recovering the velocity field from ligatures (3.39) and (3.40), and the resulting density field from the equation of state (3.41).

Boundary and initial conditions

Since the physical problem under consideration is mathematically modeled through a system of partial differential equations, an initial condition for the temporal first derivative of the species and temperature fields is needed. Moreover, spatial boundary conditions are required depending on the selected configuration and either moving-flame or fixed-laboratory reference frame. In the following chapters, different conditions will be prescribed at each study depending on its purpose. The initial condition, representative of an ignition process, is specifically rewritten for each case. It typically consists, in a general sense, of a hot spot (given temperature profile) accompanied by a corresponding depletion of reactants (species concentration profile). For the sake of conciseness, appropriate boundary conditions for the representation of each process will be addressed at each section of different configurations under study.

Chapter 4

Stable propagating flames

Previous studies on lean-premixed hydrogen-air deflagrations in Hele-Shaw chambers, both numerical (Martínez-Ruiz et al., 2019) and experimental (Veiga-López, Kuznetsov, et al., 2020), have identified the heat release, heat losses and buoyancy effects as the controlling parameters responsible for the arising stable propagating solutions. The system of equations of the reactive and confined flow model, presented in chapter 3, can reproduce the dynamics of propagation of weak flame kernels. Particularly, some specific configurations of the nearly two-dimensional flames show a steady propagation at constant speed and fixed kernel shape. These are typically isolated fronts that can take either a circular or a double-cell shape and propagate at different speeds, S_u. A detailed description of both configurations is presented in this chapter, studying the main effects of thermal and species transport, be convection and diffusion.

Since these steady flame structures remain as the first objective of the study, a moving domain is set, be a relative reference frame fixed to the premixed flame. In this sense, it allows for the study of an individual isolated kernel during its propagation through the combustion chamber. Therefore, time-evolving simulations in the moving reference frame are performed, given various initial conditions that closely mimic the steady-state solutions, and undergo small variations towards the stable structures.

The simulations are conducted in a squared domain with side length $L = L'/\delta'_T$, which moves towards the negative x-axis (left) in the absolute reference frame at a prescribed velocity $S_{r.f.} \simeq S_u$. Whenever $S_{r.f.} - S_u \ll S_u$, this method enables the tracking of the flame inside the moving domain for simulation times much longer than the characteristic residence time, ensuring that a steady propagation state is achieved. The value of S_u is then determined through the detection of the steady flame structure position over time. Although this propagation velocity can be negative in the moving reference frame (but small), inlet-outlet boundary conditions remain unchanged. In this way, a computationally affordable domain of size $L = 28$ is used, which is sufficiently large to accommodate flame structures with length scales of order unity centered in the computational area. The calculations use

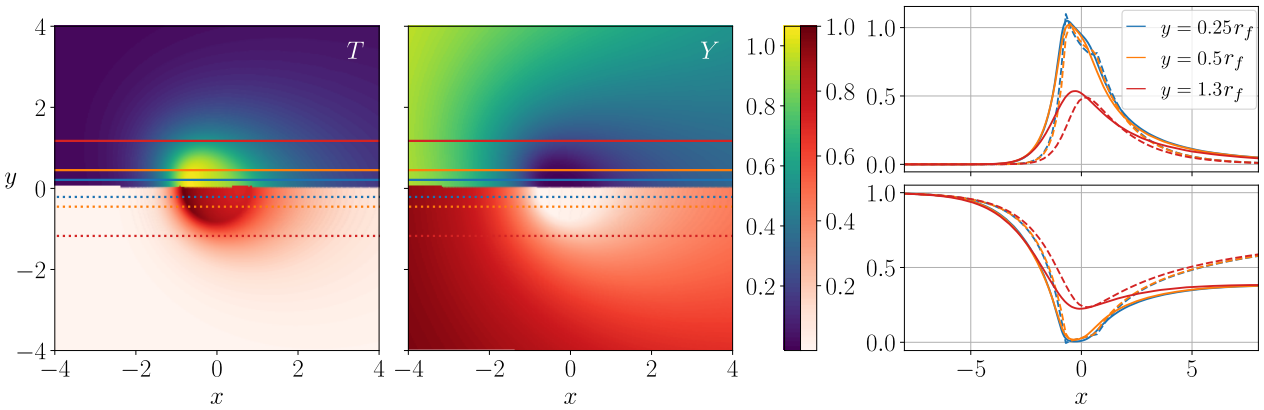

Figure 4.1: Comparison between steady structures obtained from transient FreeFEM simulations (top-half in 2D panels) and initial conditions calculated with the thermo-diffusive model (bottom-half in 2D panels), for temperature (left) and species concentration (center) fields. Longitudinal cuts at selected heights $y = [0.25\ r_f,\ 0.5\ r_f,\ 1.3\ r_f]$ for temperature (right top) and species (right bottom), comparing FreeFEM simulations (solid) and the thermo-diffusive model initial conditions (dashed).

initial conditions obtained from a reduced steady thermo-diffusive problem,

$$m\left(\cos\theta\frac{\partial T}{\partial r} - \frac{\sin\theta}{r}\frac{\partial T}{\partial \theta}\right) = \frac{1}{r}\frac{\partial}{\partial r}\left(r\frac{\partial T}{\partial r}\right) + \frac{1}{r^2}\frac{\partial}{\partial \theta}\left(\frac{\partial T}{\partial \theta}\right) - bT, \tag{4.1}$$

$$m\left(\cos\theta\frac{\partial Y}{\partial r} - \frac{\sin\theta}{r}\frac{\partial Y}{\partial \theta}\right) = \frac{1}{\mathrm{Le}}\left[\frac{1}{r}\frac{\partial}{\partial r}\left(r\frac{\partial Y}{\partial r}\right) + \frac{1}{r^2}\frac{\partial}{\partial \theta}\left(\frac{\partial Y}{\partial \theta}\right)\right],$$

with $m = \rho u_x = \text{const}$. A valid approximation when considering small flow deflections owing to the weak thermal expansion. This set can be solved through a relaxation algorithm when imposing a flame temperature at a given radius $r_f = 0.9$, that follows $T(r_f, \theta) = 0.5[(T_{f_d} - T_{f_u})\cos\theta + (T_{f_d} + T_{f_u})]$ and a depletion of species $Y(r_f, \theta) = 0.5[(Y_{f_d} - Y_{f_u})\cos\theta + (Y_{f_d} + Y_{f_u})]$, with representative upstream and downstream values of the circular flame position noted with the subscripts $-f_u-$ and $-f_d-$ respectively.

The initial 2D fields obtained are put in contrast to the steady-state result of the time-evolving simulations in fig. 4.1, to show the close agreement of the initial conditions with the expected stable outcome of the numerical simulations. The top halves of the two-dimensional panels (blue-yellow colormap) show the computational steady results for temperature (left) and species (center) fields, with the thermo-diffusive initial condition plotted in the lower halves (white-red colormap). Right-side panels show the longitudinal profiles over the selected lines to compare the distributions imposed as initial conditions (dashed) and the numerical result of the complete simulations upon achievement of steady propagation (solid).

Regarding the boundary conditions of the transient numerical simulations, three undisturbed boundaries, inlet $x = -L/2$ and lateral $y = \pm L/2$, are considered, where the initial conditions for temperature, species and pressure are preserved, corresponding to free-stream values $T = 0$, $Y = 1$ and $p = 0$, see fig. 4.2. The right limit of the domain $x = L/2$ is an open boundary where soft outlet conditions are imposed ($\partial/\partial x = \text{const.}$), allowing for convective

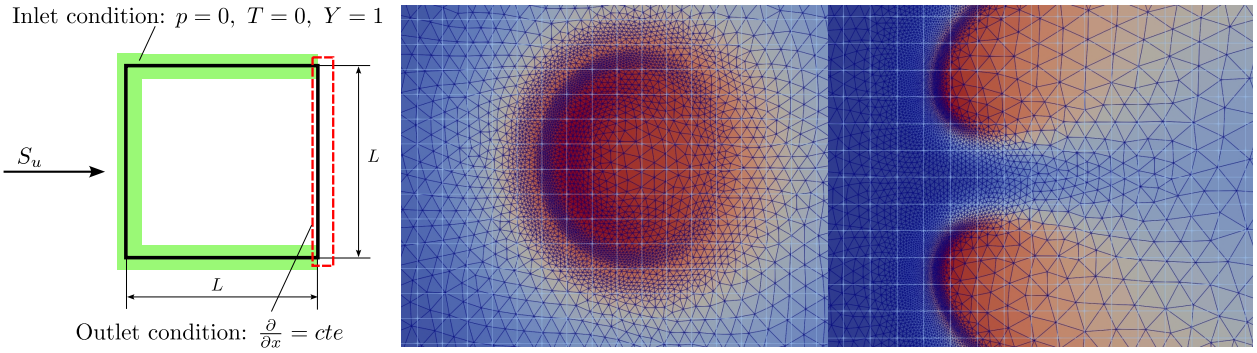

Figure 4.2: Numerical domain sketch on the left. Two mesh zoom examples of both steady structures.

and diffusive flows of mass, species and energy. The latter are automatically incorporated in the variational implementation through the computed derivatives $\partial T/\partial x|_{\text{out}}$, $\partial Y/\partial x|_{\text{out}}$ and $\partial p/\partial x|_{\text{out}}$ used at the domain-boundary integral. Note that velocity components are a byproduct of the pressure field and do not require imposing boundary conditions.

All things considered, computation of the set of equations provides the evolution of the dimensionless leading-order field variables (subscript $-0-$ has been dropped), temperature $T(\mathbf{x}, t)$, mass fraction $Y(\mathbf{x}, t)$, pressure $p(\mathbf{x}, t)$ and velocity $\mathbf{u}(\mathbf{x}, t)$, of the reactive flow confined between two infinite parallel plates and subject to the effect of buoyant forces G and conductive heat losses b. Specifically, the following values are chosen to be representative parameters of very lean hydrogen-air combustion, such as a low Lewis number $\text{Le} = 0.3$. A moderate heat release $q = 2-5$ renders an adiabatic temperature $T_a = (1+q)T_u \leq 1800$ K, typical values for mixtures of equivalence ratios $\phi \simeq (0.2-0.5)$. Moreover, the activation temperature of the lean hydrogen reaction in equivalent one-step global chemical kinetics is $T_{\text{ac}} = E_a/R_g \simeq 20 \times 10^3$ K (Fernández-Galisteo et al., 2009), so that an approximate value for the Zeldovich number is $\beta = T_{\text{ac}}(T_a - T_u)/T_a^2 = 9.26 \simeq 10$.

The numerical simulations in this chapter are computed using an in-house FreeFEM code ("FreeFEM", n.d.), a C++ open-access solver for partial differential equations based on Finite Element Methods. The system of equations is written in a variational way following the weak formulation. The domain Σ is discretized by FreeFEM solver using conforming triangulation $\mathcal{T}_h$ of a Delaunay mesh. One of the key aspects is that it is possible to readapt the mesh in each temporal step, distributing the elements to a personalized evolving feature of the field. The refinement criteria respond to the gradients of reaction rate and temperature, see fig. 4.2, in charge of capturing near-field effects, and pressure, for far-field convective effects adequate resolution. The adapt-mesh tool is effective in reducing the amount of elements in most of the unburnt area of the domain where the flow variables do not practically vary. Concerning the time discretization, a second-order backward differences formula (BDF) is used. A fully-implicit iterative method, steepest descent, is applied to compute T, Y and p in each temporal step. Further details are discussed through appendix A.

4.1 Isolated regimes and general dynamics

Freely propagating flames cannot typically sustain a planar shape of the reactive surface, owing to the rapid growth of small perturbations caused by the various types of intrinsic flame instabilities. Specifically, lean hydrogen-air premixed flames are deeply affected by the low Lewis number of the fuel, triggering the thermo-diffusive wrinkling of the flame front. The unequal rates of diffusion of thermal energy and fuel species causes a reinforcement of the combustion process for a positive stretch, and the local enrichment of the mixture at the leading front causes a rise in the flame temperature due to the lower thermal diffusivity. This process enables the existence of a region of burnt gases whose temperature exceeds the adiabatic value $T = 1$. This heat accumulation is crucial to overcome the conductive heat losses, providing extra thermal energy to sustain the combustion process. However, the large heat losses through the walls promote quenching of weaker flame regions and give rise to isolated curved reactive kernels that propagate burning part of the mixture.

The first part of this section focuses on the general description of the two types of propagating structures. Keeping this in mind, we shall select standard values of the three main controlling parameters: heat losses b, heat release q and buoyancy constant G to produce illustrative results. The first sample cases correspond to canonical configurations with the specific parametric set of $b = 1,\ q = 5$, and $G = 0$.

4.1.1 Circular flame

First, a circular canonical flame structure can be obtained. Numerical results for a characteristic case are depicted in fig. 4.3. The spatial distributions of the problem variables are presented at a late simulation time, when steady-state propagation has already been established. Specifically, the panels display the following variables: temperature (top left), species (top center), reaction rate (top right), pressure (bottom left), velocity field with isocontours for the components (bottom center), and flow streamlines (bottom right). The isocontour of $\Omega/\rho = 5$ (white solid) is plotted everywhere for visual reference of the flame position.

The temperature field exhibits a nearly axisymmetric distribution, with the superadiabatic burnt-gas region identified for $T > 1$. The species distribution, also displaying axial symmetry, shows a greater characteristic length for concentration variation due to larger diffusive effects and the absence of sink terms, contrarily to the heat loss that affects the temperature field. Furthermore, the ring-shaped reaction rate reaches its highest values at the front part, facing the free stream, while the rear part corresponds to a weaker flame front. In this region, the main flow has already been burned, and the mixture is primarily fed by rear diffusion, as it will be shown later. Although the numerical simulations exhibit a clearly circular shape, experimental observations typically reveal a hemicircular front (Veiga-López, Kuznetsov, et al., 2020, Palomeque-Santiago et al., 2024). The rear part of this front is strongly influenced by the trail of burnt products and is especially affected by water condensation on the plates (Yañez and Veiga-López, 2021).

Finally, the velocity field is computed using eqs. (3.39) and (3.40). The unburned flow enters the domain from the left side of the moving reference frame at a speed equal to

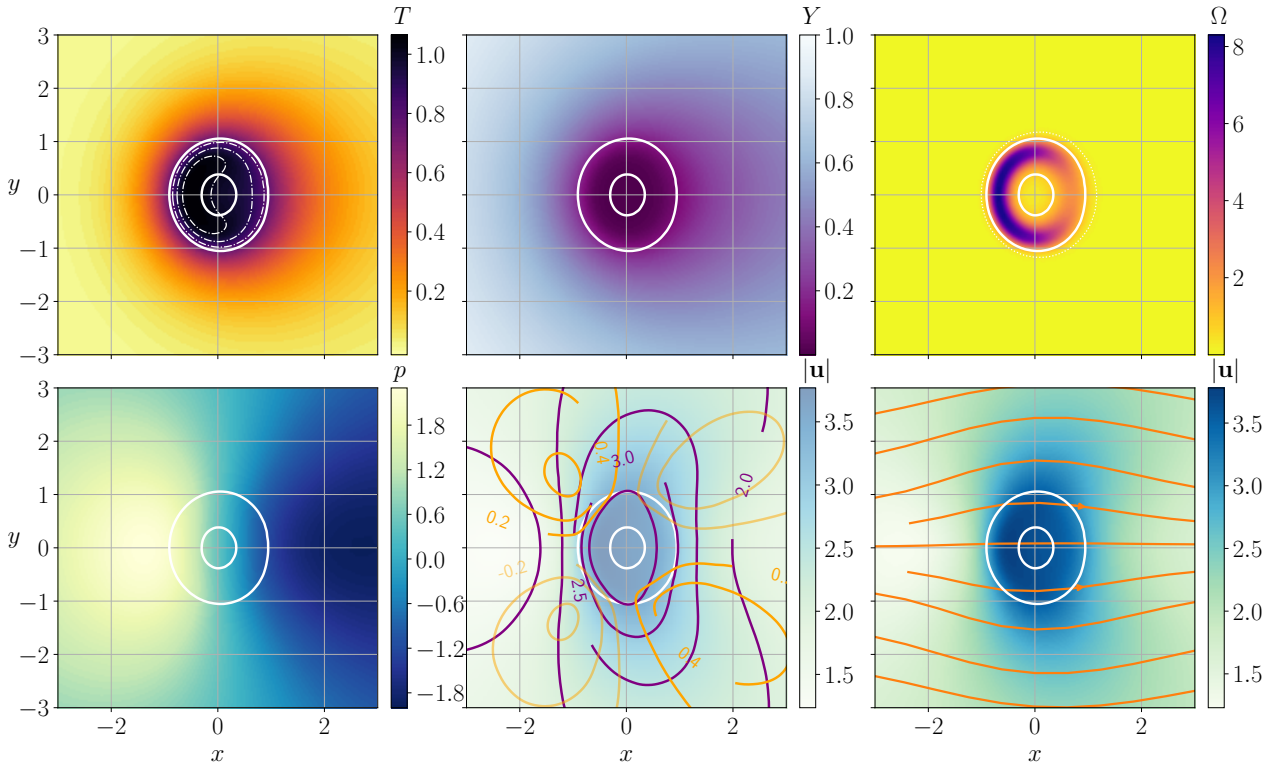

Figure 4.3: Steady circular flame with $b = 1$, $q = 5$, $G = 0$. The isocontour of $\Omega/\rho = 5$ (white solid) is plotted for visual reference of the flame, over temperature (dash-dotted isocontours for $T \in [0.75\ T_{\max},\ 0.85\ T_{\max},\ 0.95\ T_{\max}]$), species concentration, reaction rate, pressure and velocity field, with $u_x \in [1.5,\ 2,\ 2.5,\ 3,\ 3.5]$ and $u_y \in [-0.6,\ -0.4,\ -0.2,\ 0.2,\ 0.4,\ 0.6]$ isocontours (bottom center) and streamlines (bottom right).

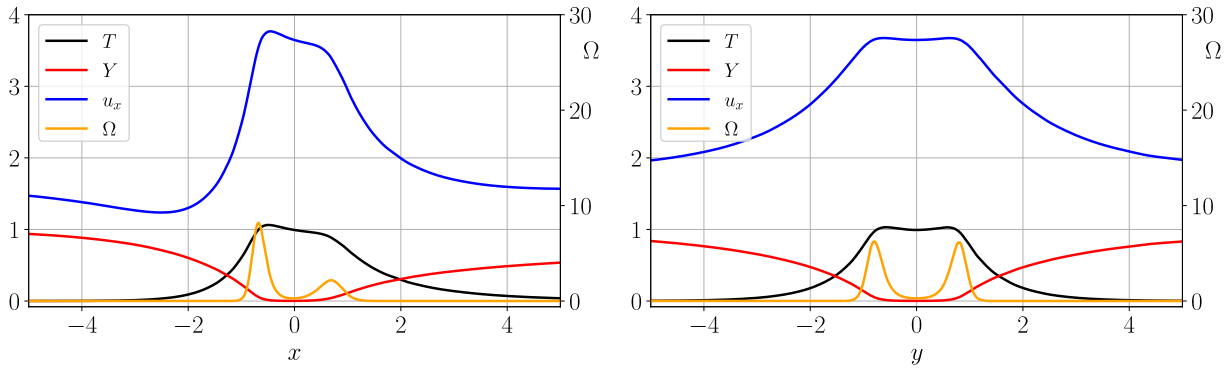

Figure 4.4: Steady circular flame with $b = 1$, $q = 5$, $G = 0$. Longitudinal and transverse cut to the panel configuration in fig. 4.3. Longitudinal cut along the $x-$axis, $y = 0$ (left). Transverse cut along the $y-$axis, $x = 0$ (right). Temperature (black), species (red) and $x-$axis velocity (blue) are referred to the left axis; reaction rate (orange) to the right axis.

$S_{u1} = 1.8$, the kernel's propagating speed. The streamlines superimposed on the velocity field reveal an almost parallel arrangement, indicating a nearly constant mass flow rate projected

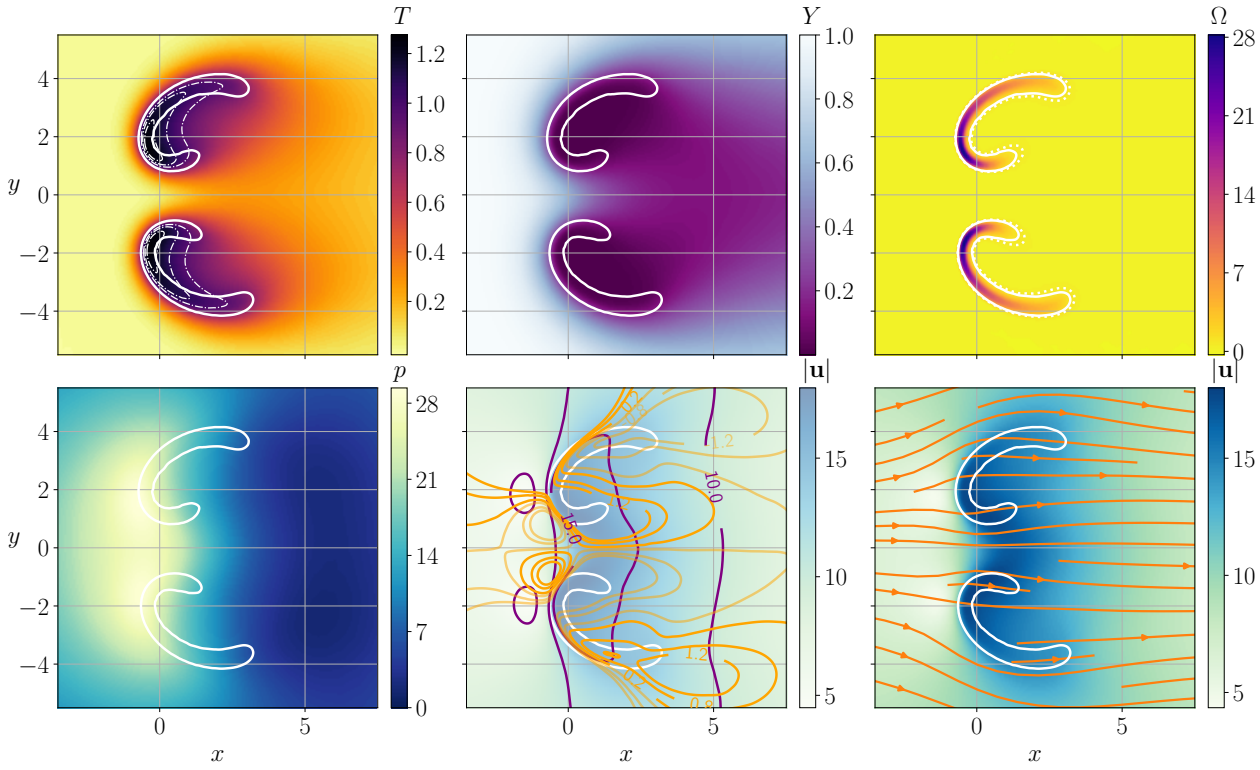

Figure 4.5: Double-cell flame with $b = 1$, $q = 5$, $G = 0$. See caption in fig. 4.3 for detailed references of the panels.

onto the horizontal axis, $\rho u_x \simeq \rho_u S_u$. This relationship was previously hypothesized in the thermo-diffusive model to calculate the initial conditions.

Moreover, fig. 4.4 shows a longitudinal cut of T, Y, u_x and Ω along the symmetry axis on the left, and a transverse cut at $x = 0$ on the right. The facing and rear active fronts are clearly distinguishable in the first panel, while the prominent lateral symmetry of the configuration is evident in the second cut.

4.1.2 Double-cell flame

The second canonical structure is a two-cell flame, as first observed in Veiga-López, Kuznetsov, et al., 2020, that is recovered here as an alternative stable solution for the same parametric set. The variables shown in fig. 4.5 display this secondary stable solution corresponding to the same case with $G = 0$, $q = 5$ and $b = 1$, where the general trends of the fields are conserved from the single flame case. The characteristic hemicircular tips are of a size comparable to the ring structure, of order unity, but display a much thinner reaction sheet. The frozen gap between the two cells also exhibits a thickness of order unity, $\ell = \ell'/\delta'_T \simeq 1$, which turns out to be a function of G and b values, as shown below.

However, some differences of this particular twin-flame structure compared to the circular solution can be pointed out. Some of them are the higher temperature value, a faster reaction rate and larger propagating velocity, $S_{u2} = 9.5$. The increase in intensity of the combustion

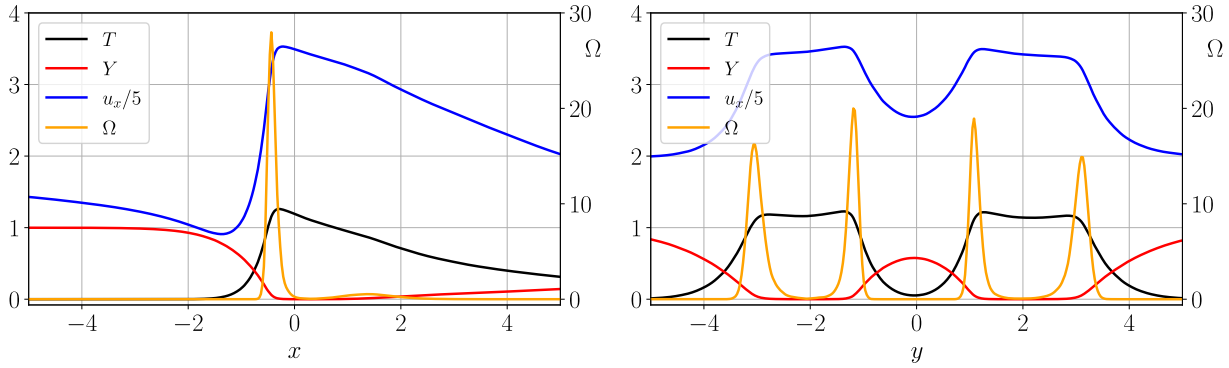

Figure 4.6: Double-cell flame with $b = 1$, $q = 5$, $G = 0$. Longitudinal and transverse cut to the panel configuration 4.3. Longitudinal cut along the $x-$axis, $y = y|_{T=T_{\max}}$, (left). Transverse cut along the $y-$axis, $x = 0$, (right). Temperature (black), species (red) and $x-$axis velocity (blue) are referred to the left axis; reaction rate (orange) to the right axis.

process can be traced to the enhanced convective effect. The thermal and species wakes can also be observed as significantly marked longer trails related to more intense convective effects. It is worth noting that the axisymmetry of the first canonical configuration is completely lost in this case. The reactive structure fails to close in the rear area, as diffusion cannot counterbalance the increasing convective effects.

Finally, fig. 4.6 displays analogous longitudinal and transverse cuts for the double configuration. In comparison to the isolated circular case, a much stronger front is observed in the leading tip, while weaker reaction rates are found in the rear part. The variables are here characterized by sharper profiles and the aforementioned greater chemical reaction. Therefore, a detailed transport analysis is performed next to discern the physical mechanisms driving the formation of each of the flame structures described above.

4.1.3 Transport effects, convection and diffusion

Original findings in lean-hydrogen experiments, flame balls (Zeldovich et al., 1985, Fernández-Tarrazo et al., 2011) and flame circles (Martínez-Ruiz et al., 2019, Veiga-López, Kuznetsov, et al., 2020), indicate that mass diffusion effects must be dominant. Due to the unequal rates of diffusion, $\mathrm{Le} = 0.3$, the transport of reactive species is faster than that of temperature. Therefore, to first characterize the relative importance of these mechanisms, fig. 4.7 shows the species diffusion velocity (left), convective transport (center), and the total composition of scalar transport (right), with superimposed streamlines for each relative term in the steady flame-kernel reference frame. The top-row panels correspond to the isolated circular case, while the bottom row is dedicated to the double-cell structure.

The diffusion velocity field, calculated using Fick's law $-\nabla Y/\mathrm{Le}$, provides fresh reactants to the rear side, while the convective flow pushes the fuel mixture fraction downstream. The latter flow dynamics are governed by the pressure eq. (3.42), developed in chapter 3 and reproduced here for convenience, along with the viscosity-dominated momentum eqs. (3.39)

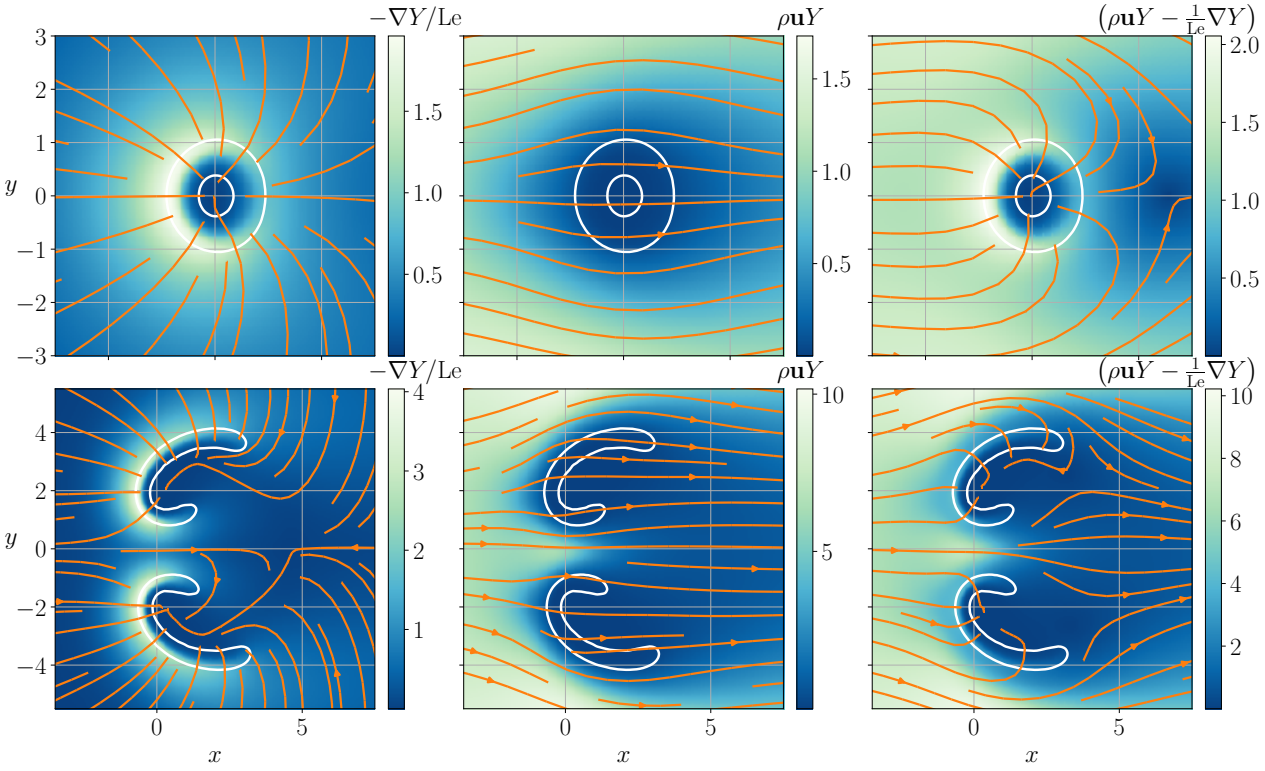

Figure 4.7: Computed fields of $\nabla Y/\mathrm{Le}$ and Y, base configurations at $b = 1$ and $G = 0$, superposed streamlines corresponding to the field variable, from left to right: $-\nabla Y/\mathrm{Le}$ Fickian diffusive transport, $\rho \mathbf{u} Y$ convective transport and $(\rho \mathbf{u} Y - \nabla Y/\mathrm{Le})$ species total flux.

and (3.40) in the moving-flame reference frame.

$$\nabla^2 p = -q \left(\nabla^2 T + \Omega - bT \right) + \frac{\partial \rho}{\partial x} G$$

$$u_x = -\frac{\partial f}{\partial x} + (\rho - 1)G + S_u; \quad u_y = -\frac{\partial p}{\partial y},$$

with $f = p - Gx$. From fig. 4.7, it can be noted that the relative importance of diffusion and convection terms differs between the two configurations. In the circular isolated case, the diffusion velocity is comparable to the convective effects, allowing the unburnt mixture to reach the rear part of the flame ring. In contrast, for the double structure, the convective component is sufficiently large to hinder the refilling process, leaving the reaction structure open at the rear. As a result, an elongated wake of products is observed behind the two tips.

Moreover, the volumetric expansion rate can be expressed in terms of the pressure equation through the definition of the velocity field,

$$\nabla \cdot \mathbf{u} = -\nabla^2 p + \frac{\partial \rho}{\partial x} G = q \left(\nabla^2 T + \Omega - bT \right) \tag{4.2}$$

where the right-hand side corresponds to the energy convection term for the stationary solution $(\nabla \cdot \mathbf{u})/q = \rho \mathbf{u} \nabla T$. The pressure Laplacian is intimately linked to the local thermal expansion

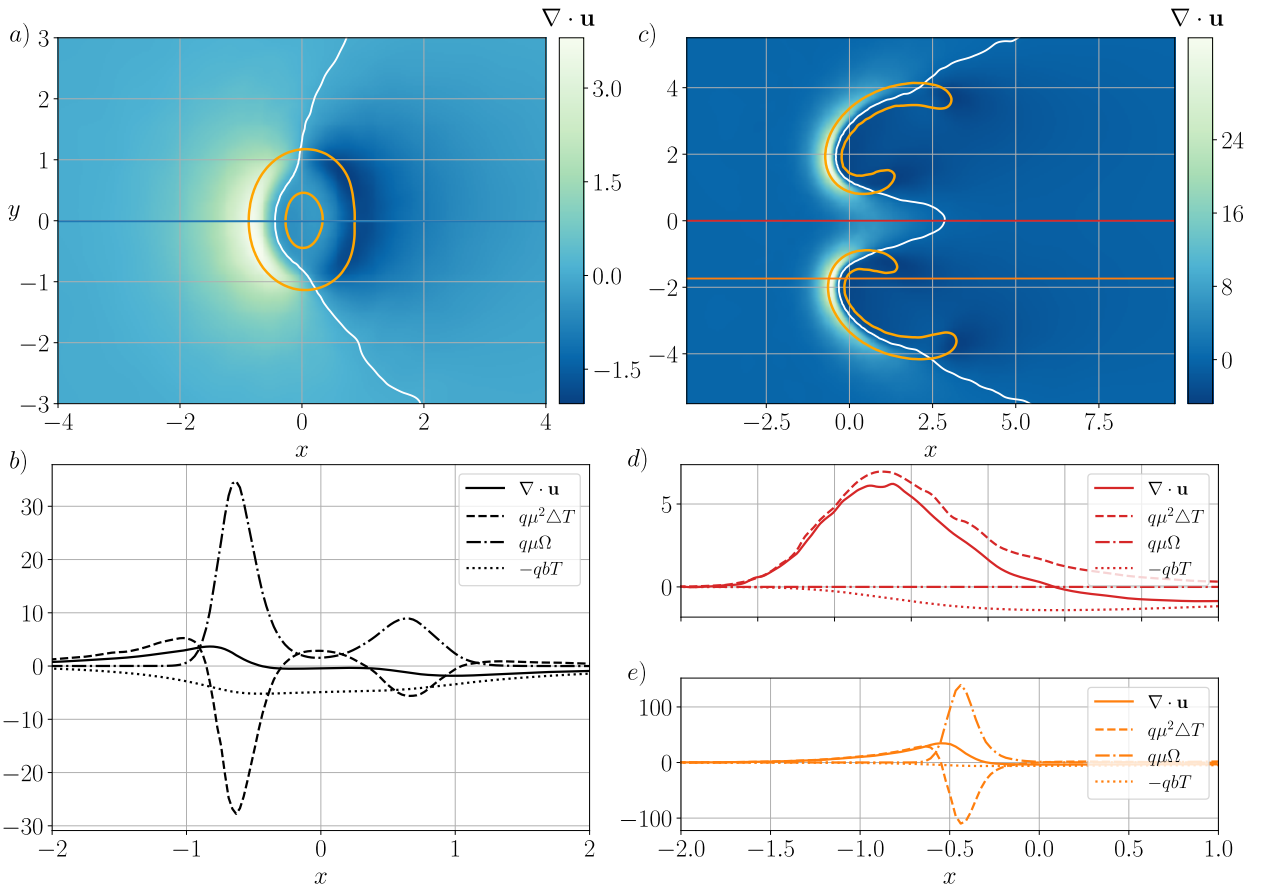

Figure 4.8: Circular and double-cell configurations at $G = 0$, $q = 5$ and $b = 1$. Expansion rate $\nabla \cdot \mathbf{u}$ in (a) and (c) panels, orange isocontour at $\Omega/\rho = 5$. Panels (b,d,e) display $x-$cuts of contributions to eq. (4.2).

of the flow, the volume production rate. Figure 4.8 shows, in the upper row, the spatial distribution of the velocity divergence (color map) with the reaction rate isocontour reference (orange) and zero-divergence isocontour (white). The lower panels offer $x-$axis longitudinal cuts of eq. (4.2) terms. For the isolated circular flame, the volume production term displays negative values (compression zones) behind the flame due to conductive cooling, heat losses, and positive values ahead of the flame (expansion zones) pointing out the preheated region. From the $x-$axis profile in panel (b), it is seen that the convective contribution (solid) divided by the diffusion term,

$$\frac{\rho \mathbf{u} \nabla T}{\nabla^2 T} = \frac{\nabla \cdot \mathbf{u}}{q \nabla^2 T} \sim \mathcal{O}\left(10^{-1}\right), \tag{4.3}$$

is small. Therefore, a direct balance between the diffusion (dashed) and reaction (dash-dotted) takes place.

For the double-cell structure, the divergence map in panel (c) shows a region of positive volume production rate, corresponding to the frozen gap between the two-cell tips. This indicates a flow acceleration region with frozen chemistry. Overall, stronger convection effects and local expansion create a high-stretch extinct area in the central region of the symmetric front. Two

cuts are shown for this second stable flame configuration: one along the symmetry axis on panel (d) and another along the $y-$coordinate of maximum reaction rate $y|_{\Omega_{\max}} = \text{const.}$ in panel (e). The relative relevance of thermal convection (solid line) to diffusion (dashed line) is now increased, in front of the flame, to approximately $\nabla \cdot \mathbf{u}/(q\nabla^2 T) \simeq 1/3$. This enhanced convective effect provided by larger velocities enlarges the local gradients of temperature and species, inducing also more pronounced diffusion and reaction rates balance. However, the greater convection and reaction terms in the double structure prevent mass diffusion from filling the product trail with fresh reactants during a time span comparable to the shortened residence time. Moreover, the hot region is cooled down via heat losses disabling the rear-side reaction.

4.2 Solutions parametric space

The two controlling parameters, for a given mixture with selected heat release $q = 5$, are: the heat losses coefficient $b = 2h'\lambda_w/(a^2 h'_w \lambda_u)$, which accounts for the relative thermal conductivity of the gas and plates, channel and plate heights, and flame thickness; and the gravitational constant $G = ga^2\delta'_T/\left(12\text{Pr}S'^2_L\right)$. Therefore, the different solution regimes are explored in the parametric space within the intervals $b \in [0.8, 1.5]$ and $G \in [-4, 4]$. Although both configurations presented above are stable for specific coincident combinations of the buoyancy and heat-loss parameters, their regions of existence may differ. Figure 4.9 shows the parametric space, the left graph corresponds to the circular flame while the one on the right corresponds to the double-cell solution. The appearance of single circular flame stable solutions (filled circles) and stable double cells (triangles) is depicted over the parametric space $[b, G]$. However, the flame-circle region, marked with a shadowed area, is limited for large values of G and low b by the transient split process of initial circular flames into two separate fronts (empty circles) that advance together with a gap that remains extinct. The dash-dotted boundary is defined by varying-shape solutions that do not achieve splitting neither stable propagation. Furthermore, circular cases can also evolve towards extinction (crosses) for large enough values of b and negative values of G. The second regime arises in an overlapping parametric space, when initial flow conditions are modified to double-front symmetric fields under equal $[b, G]$. It should be clarified that all the stable solutions presented here are found for initial flame conditions propagating in the negative direction of x-axis. Then, values $G_1 = A$ and $G_2 = -A$ provide different propagation speeds $|S_{u1}| \neq |S_{u2}|$ and sizes of the reaction structures. However, inverse-sign solutions $S_{u2} = -S_{u1}$ are also valid for initial flow variables reversed in x (flame propagation in the positive direction) as the equations remain the same if changing signs to $[x,\ G,\ S_u]$. Therefore, mirroring maps in fig. 4.9 with respect to the $G = 0$ axis also exist.

Although there is a multiplicity of stable solutions in the parametric space, each solution arises from different initial conditions. The circular isolated kernel is initialized from the aforementioned thermo-diffusive solution and the double structure is ignited from a $y-$symmetric field involving two hot peaks and species sinks. This leads to the hypothesis that the appearance of each solution strongly depends on the history of the flow. Specifically, the evolution of the flame front for several characteristic times shows a stabilization from the initial condition to the steady propagation state, with a determined size and speed. On the left column of fig. 4.10,

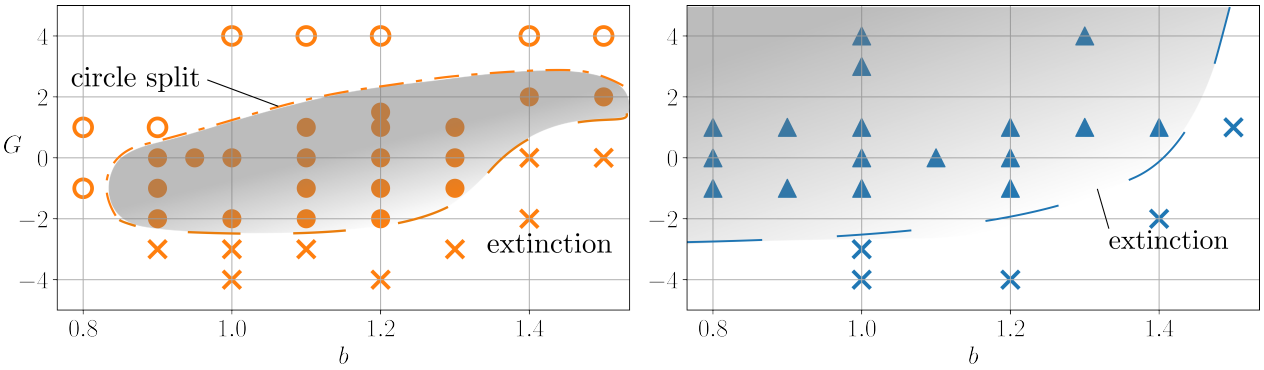

Figure 4.9: Parametric space of stable circular flames (filled circles) and double-cell flames (triangles). Extinction of both cases (crosses) and break-up of circular flames (empty circles) delimit the regions of stable cases (shadowed).

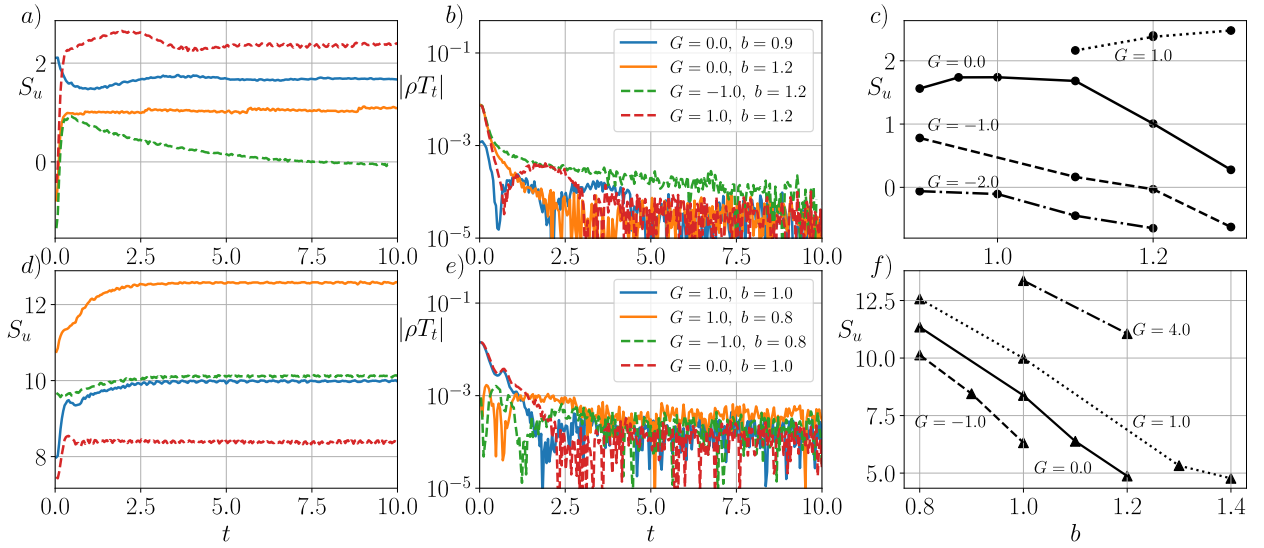

Figure 4.10: Evolution of the propagation velocity (a,d), the transient term (b,e), and the steady speed of propagation S_u as a function of b for several G (c,f) of numerical simulations of isolated circular flames (a,b,c) and two-cell flame (d,e,f) cases.

the evolution of the propagation velocity of both configurations is depicted along the initial transient before reaching the stationary value for different combinations of b and G. Circular flames (top panels) display lower propagation speeds than double-cell ones (bottom panels), anticipated by the increase in convective effects. The middle column presents the evaluation of the transient effect, the unsteady term of the energy equation, as a convergence indicator to the steady-state propagation. $|\rho T_t| = \sum_i^N \left(|\rho \partial T/\partial t|_i\right)/N$ marks the acceleration decay, where i represents the elements of a regular mesh where the solution has been interpolated. Finally, on the right column, the propagation speed for the discrete cases analyzed along this section are gathered. It can be noticed that greater propagation speeds S_u are obtained for lower heat losses, decreasing b parameter, and higher buoyancy effects, increasing the gravitational constant G. In the same way, initiations of simulations of two-cell flames evolve towards faster propagation when b is reduced and G is increased.

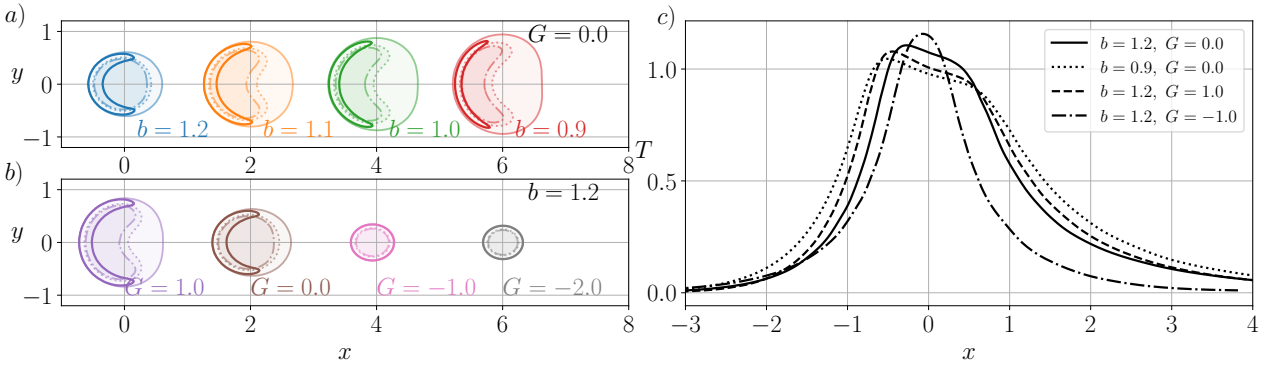

Figure 4.11: Isolated circular flames. Morphology of isocontourns depending on the heat loss parameter (a) and the gravitational constant (b). Temperature distribution (c) of different cases along the $x-$axis.

Concerning this buoyancy effect, the $x-$momentum eq. (3.39) involves the gravitational acceleration as $(\rho - 1)G$. Hence, a positive value of this parameter $G > 0$, for upward propagation, leads to a buoyancy force in the negative direction of the $x-$axis. Considering the divergence eq. (4.2), the effect of this positive coefficient $G\partial\rho/\partial x$ creates an extra compression effect in the front part of the flame, where the density gradient is negative, and an expansion in the rear part. These regions are crucial for modifying the propagation velocity and altering the relevance of the convective term in the outcome of different solutions. Note that the propagation velocity can become $S_u \lesssim 0$ for $G < 0$, which implies downward-facing slowly propagating flames that are lifted by buoyancy. Additionally, transverse heat losses introduce a reduction in flame size in this very weak limit, owing to the sink term bT. This effect also results in greater front curvatures and slightly higher peak temperatures, which affect the reaction rate, buoyancy effects, and the propagation velocity. Therefore, the competition of these effects leads to a highly nonlinear dependence of the final propagation speed, as shown by $S_u(b)$ for $G = 1$ in fig. 4.10 (c).

Finally, the influence of the parameters on the morphology of the front of single circular flames is shown in fig. 4.11 (a, b) through the reaction rate isolines of $0.9 \times \Omega_{\max}$ (solid lines), and temperature isocontours at $T = 1.02$ (dashed), $T = 1$ (dot-dashed) and $T = 0.9$ (dotted). The role of b involves the competition between the enhancing of the combustion process through increasingly curved fronts and the inherent temperature reduction, which is complemented with a contraction effect due to local cooling. Therefore, an increase in b helps to counteract the effect of thermal expansion and makes the structure smaller. As shown in this figure, the flame evolves from a hemicircular shape to a ring shape that progressively becomes smaller until it disappears due to flame extinction. An equivalent contribution to the size and shape of the reaction kernel is produced by the variation of G, decelerating the structure as it is diminished. The superadiabatic temperature region is concentrated at the leading edge of the structure, as depicted in fig. 4.11 (c) along the x-axis, and moves at the center when modifying the parametric space towards extinction events.

On the two-cell side, fig. 4.12 provides the separation and size of the mirroring cells for various combinations of (b, G), with reaction-rate isocontours (solid lines), and temperature isolines at $T = 1.2$ (dashed), 1 (dot-dashed) and 0.9 (dotted). It is remarkable that closer and more

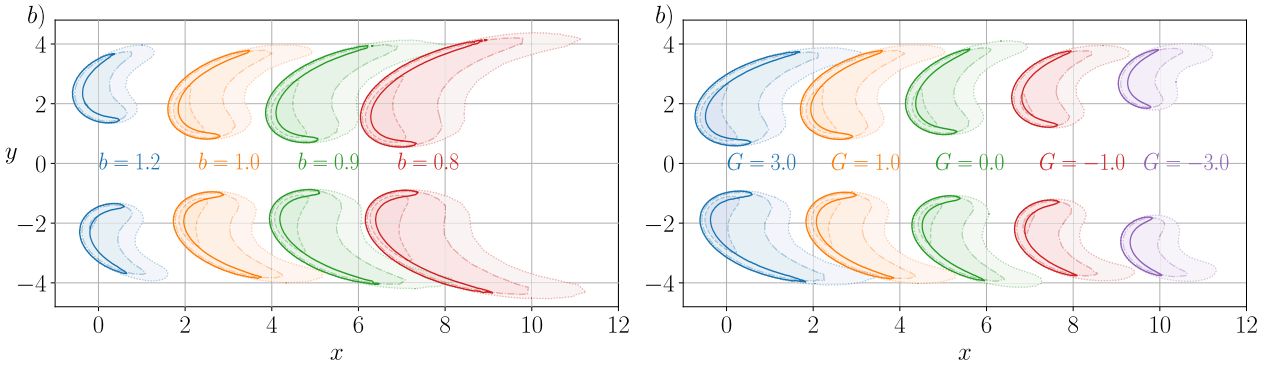

Figure 4.12: Two-cell flame cases temperature isocontours. (a) Heat-loss coefficient variation $b = [1.2, 1, 0.9, 0.8]$ with $G = 1$. (b) Variation of the buoyancy coefficient $G = 3, 1, 0, -1, -3$ at constant $b = 1$.

elongated cells are found when lowering b or increasing G, as a sign of larger propagation velocities and, thus, enhanced convective effects.

4.3 Bi-stability remarks

As a concluding highlight of the steady-state study, two well-distinguished stable configurations representative of very lean hydrogen premixed flames are characterized. Specifically, circular and double-cell reaction fronts are found in quasi-planar scenarios with pronounced heat losses. The physical mechanisms that produce different flame regimes are the increase in convective effects and in reactive front size, which can be altered through modified heat losses or appropriately directed buoyancy forces. A major role of convection and local thermal expansion effects are also identified to grant the symmetric double front appearance. Acceleration of the flame via the aforementioned mechanisms drive the circular front to an unsteady splitting scenario. The actual parametric region of existence is found to be different for each of the configurations.

Finally, both solutions can be obtained under some equal combinations of the heat loss and buoyancy parameters $[b, G]$ when different initial conditions are applied. The history of reactive problems in confined configurations subject to major conductive heat losses is key to predict the arising of either one of these propagating regimes. These results granted further research regarding the transient evolution of each configuration from characteristic ignition events and experimental studies on the validation of the regions of existence (Palomeque-Santiago et al., 2024), which later confirmed the multiplicity of solutions predicted here.

In non-linear systems, the presence of multiple solutions typically arises from the equilibrium of competing physical mechanisms. In combustion theory, solution uniqueness fades away in one dimensional planar flames due to factors like competing non-linear chemical reactions, molecular diffusion, heat losses, or phase-change processes, (Clavin et al., 1987, Bonnet, 1995). Fixed-point multiplicity can also be observed in higher dimensional simulations or experimental combustion setups, often linked to hysteresis loops in dynamical systems, such as thermo-acoustic coupling (Etikyala and Sujith, 2017), flame edges (Daou et al., 2003), droplet

combustion (Carpio et al., 2020), and cool flames (Reuter et al., 2016). In these previous examples, solution multiplicity is unveiled by slowly modifying the controlling parameter. Typically, the experiment or simulation starts below a critical value when the system is at a stable steady state. As the value of this parameter is increased, the systems bifurcates and either starts oscillating or evolves to achieve a different steady state. If the experiment is repeated reducing the value of the parameter from a larger initial value, the systems evolves following a different path in which the unsteady solution is not observed or the steady solution is different. Further reduction of this parameter to reach the critical value would give a sudden transition to return to the initial fixed point. Throughout all these examples, the evolution of the system is determined by its initial state and the bi-stability of the system is only observed in the hysteresis region. Outside this region, both solutions were never observed simultaneously.

Chapter 5

Transient dynamics

The multiplicity of solutions is a side-product of the initial study in chapter 4, that later calls for the explanation of the originating process of each structure. This chapter is devoted to the analysis of the history and transient of the flow field, considered as the main key to predict the arising of either one of the configurations (Domínguez-González et al., 2024). A study of initiation transients reproducing ignition events is first proposed, which explores the unsteady dynamics of the reactive kernels. These ignition events are then addressed from a causality perspective to identify the different pathways to the double-cell or isolated structures.

After a first description of the two steady isolated configurations, the circular and the double-cell flames, the parametric study for heat-loss parameter and gravitational constant variations shows that both configurations seem to coexist under the same set of parameters. Contrarily, previous limited sets of experiments observed only the double structure for downward propagation and the circular case for upward propagation (Veiga-López, Kuznetsov, et al., 2020). A bi-stable behavior is here predicted, and evolution towards one or another configuration depends solely on the history of the flow during ignition.

Keeping this in mind, a set of ignition cases, which are prescribed through different initial conditions, are proposed to extract information from the set of transient dynamics. The transient examples are a casuistic set claiming to represent real possibilities during the flow history. The following study aims to identify the main events in the transients that lead to one or another configuration.

This time a wider absolute domain than the previous one is used to analyze the ignition transient. A novel implementation of an in-house GPU pseudospectral method is used with Fourier-Fourier discretization of 2048^2 modes in a squared and periodic computational domain. Its dimensionless size is $L \times L = 30\pi \times 30\pi$, which, in turn, provides a minimum resolution of 15-point flame thickness. The temporal discretization employs the third-order Runge-Kutta temporal integration from Spalart et al., 1991, although a review with other suitable integrators can be found in Kassam and Trefethen, 2005. The time step used in the simulations is dt = 1e -6, which is reaction-rate limited in a standard 3/2-dealiased grid. The reaction term Ω involves transcendental functions of the evolution variables and, thus, it cannot be properly dealiased in a pseudospectral algorithm. The approximation to the fully

dealiased reaction term can be improved by increasing amounts of zero-padding, (Canuto et al., 2007). However, we observed no appreciable difference when transitioning from a 3/2 dealiasing to a 3-fold one, which justifies the use of the most cost-effective option in the following cases. The use of a Fourier-collocation method ensures accurate calculation of the convective and diffusive derivatives, even close to the limit of the grid resolution, as the dispersion-relation of the discretized operators is optimal. This type of discretization is widely used in simulations of the turbulent Navier–Stokes equations (Jiménez, 2018b), where the dissipative scale is often much smaller than the domain length scales. In the present code, the smallest scale is found on the gradients of the temperature, which are captured by the spectral derivative operator with approximately the same resolution as the temperature itself. This is important in the present simulations, as the bifurcation dynamics are expected to depend on the local convection-diffusion-reaction balance. For a deeper view of the temporal discretization, appendix B can be consulted.

5.1 Ignition cases

The numerical experiments consist on the initialization of the same horizontal configurations ($G = 0$) of quasi-2D domain (fixed b) and the same lean hydrogen-air mixture (fixed q), changing the initial condition for the ignition process. This is represented through a hot spot with a depletion of species concentration applied to the center of the domain. The imposed temperature field ignites the mixture and triggers a transient evolution of the reactive front in the stagnant-gas fixed reference frame.

To accomplish the goal, two initial conditions are created for the temperature and species field. They are prescribed in polar coordinates since point-like ignition events are represented. In particular, an exponential decaying temperature along the radial coordinate and a lobular modulation is used,

$$T_i = T_0 \exp\left\{-0.1r^2\left[1 + \frac{\cos(N\theta)}{2}\right]\right\}, \tag{5.1}$$

$$Y_i = 1 - \exp\left\{-0.1r^2\left[\frac{\cos(N\theta)}{2}\right]\right\}, \tag{5.2}$$

where $r = \sqrt{x^2 + y^2}$ and $\theta = \arctan(y/x)$, where two new parameters related to the ignition event are introduced. N corresponds to the number of lobes while T_0 refers to the initial temperature peak for the temperature function. Since the exponential part of the initial-condition functions is built to be azimuthally periodic, the peak temperature T_0 is a direct indicator of the amount of deposited energy and the initial thermal expansion. The number of lobes N, represents the spatial distribution of energy concentration. By giving a set of $[N,\ T_0]$, the deposited energy and spatial perturbations are prescribed. Taking a fixed value of the thermo-chemical parameters set $[q,\ \beta,\ b]$, while varying the ignition new parameters N and T_0, different transients are forced to occur. Figure 5.1 shows four sample initiations through the temperature field (color map) and reaction rate isocontours (white lines) at a time instant right after the initial condition $t = 0.01$, for increasing lobe number N.

These regular ignition events are not intended to accurately emulate a real-life scenario, where

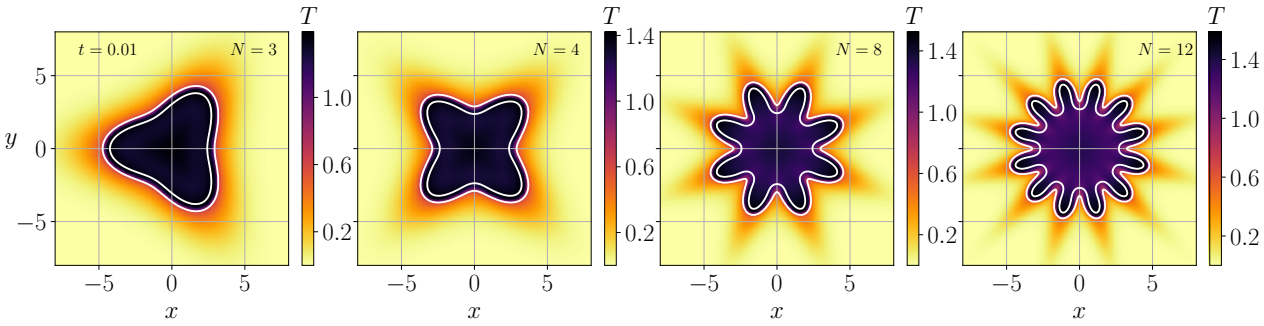

Figure 5.1: Initialization example for $[q = 5,\ b = 1.0,\ T_0 = 1.5]$ at $t = 0.01$ varying the number of lobes $N \in [3,\ ,4,\ 8,\ 12]$.

Table 5.1: Results of the parametric analysis, including splittings (s), oscillations (o) and extinctions (e), to produce circular (c) flames, merging to double-cell (d) kernels or unstable (u) fronts.

			N			
q	b	T_0	3	4	8	12
2	0.5	1.1	s – **c**	s, o – **c**	s – **e**	s – **c**
2	0.7	1.1	s – **c**	s – **c**	s – **c**	**c**
2	1.0	1.1	**c**	**c**	**e**	**c**
5	1.0	1.1	s, o – **d**	s, o – **d**	s – **d**	s – **d**
5	1.0	1.5	s – **d**	s, o – **u**	s, o – **d**	**c**
5	1.0	1.8	s, o – **d**	s, o – **u**	s – **d**	**c**

purely axisymmetric temperature profiles or parameters like the number of lobes cannot be controlled. However, this approach serves as a simple generator of numerical tests to study the simplest main building blocks that can draw the evolution toward each steady propagating structure: flame geometry and local flow properties. In addition, these blocks can imitate local experimental perturbations of the real-life ignition process. Moreover, this type of ignition does not require thermo-diffusive and hydrodynamic instabilities to develop, inducing a quick corrugation and splitting of the initial front in manageable computational times.

Conversely, fig. 5.2 shows six examples of central ignition cases with fixed ignition parameters $N = 3,\ T_0 = 1.1$, changing the thermo-chemical ones. The flame shape at different instants is superimposed to provide visual evolution of the propagation. The last time instant is printed in each panel, t_{end}. A fixed heat release parameter $q = 5$ is prescribed (top row) with increasing heat losses b (left-to-right), to compare with analogous variations for $q = 2$ (bottom row). In general, it is seen that weaker propagation is achieved as we decrease the heat release, representative of leaner conditions, with longer evolution times. Likewise, the increase of the heat loss parameter promotes quenching areas and delays propagation in the same way. Overall, coherently reproducing the same trends already covered in the previous chapter.

Table 5.1 presents the numerical experiments carried out classified by the parameters $[q,\ b,\ N,\ T_0]$. As seen in the table, the peak temperature is varied in an interval of

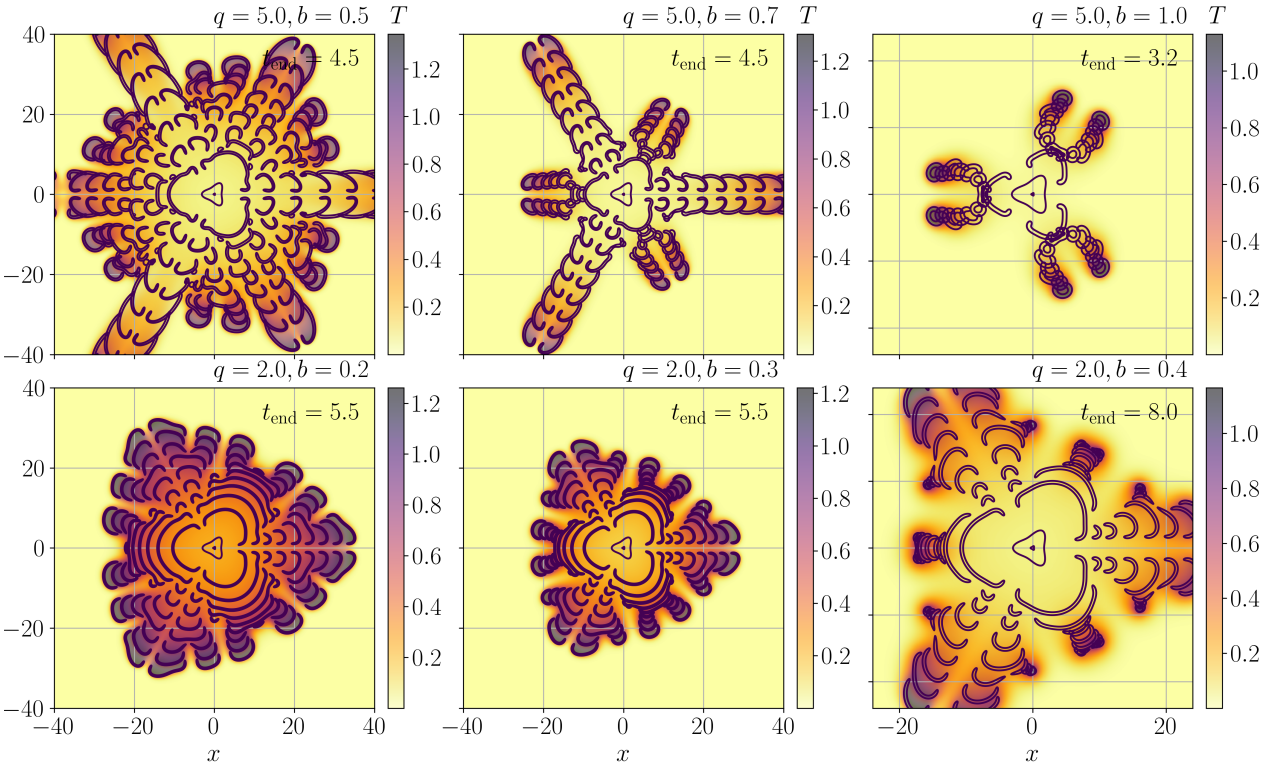

Figure 5.2: Superimposed snapshots of transient examples for six simulations with fixed ignition parameters $N = 3$, $T_0 = 1.1$, varying thermo-chemical ones, q and b.

$T_0 \in [1.1,\ 1.5,\ 1.8]$ while the lobe numbers are chosen to be $N = [3,\ 4,\ 8,\ 12]$. Several events of the dynamics that prescribe the final state are identified: oscillations of the main front (o); splitting (s) that may form circular flames (c) or a double structure (d) after a merging process; unsteady flame propagation (u); and extinctions (e). Figure 5.3 shows the comparison between twelve different simulations, the three last rows in table 5.1. Each panel is devoted to a fixed number of lobes, with three different sectors depicting the behavior of different initial peak temperatures T_0 (color code). The thermo-chemical parameters are fixed to $q = 5$ and $b = 1$, where the bistable behavior was previously confirmed. It can be observed that different interactions are found varying the ignition parameters so that both steady solutions, the circular isolated and the double-cell, are produced.

5.2 Flow segmentation

Since the object of study is the dynamics and interaction of the flame kernels, the analysis of post-ignition dynamics requires the definition of the flame structure. A structure is a region of the field in which a variable of interest is above a certain threshold in each specific case. As a generic example of flow segmentation, the root-mean-square function $\text{rms} = UV = f(z)$ (being U and V the flow perturbation components) is a good indicator for a structure in the turbulent flow of a liquid through a channel. Assuming an ergodic process where all directions are homogeneous except for the channel height. The *rms*, in this case, locates structures

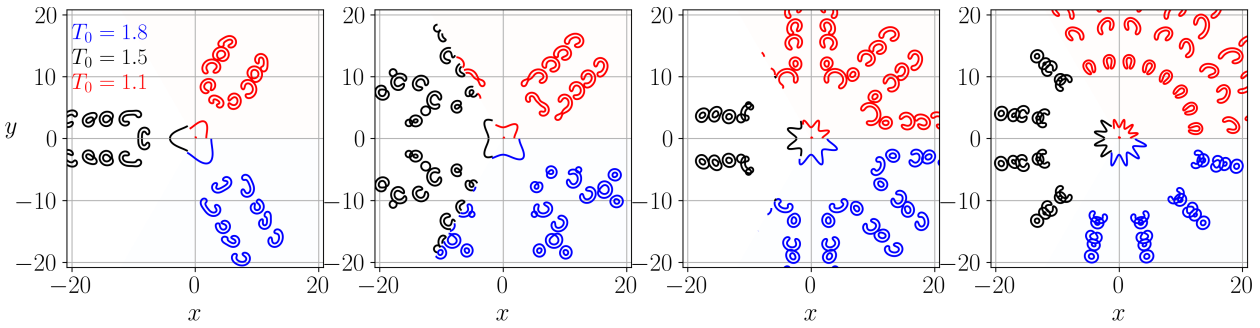

Figure 5.3: Transient examples for fixed thermochemical parameters varying the ignition parameters. Different temperature peak in different colors, placed in different sectors of the space graph $T_0 = 1.1$ (red), $T_1 = 1.5$ (black) and $T_0 = 1.8$ (blue); four different graphs, from left to right, for the four options of number of lobes $N = 3,\ 4,\ 8,\ 12$.

all along the transverse coordinate, not only in the central part of the channel. Once the variable of interest is identified, a threshold must be set, which opens up a whole scientific area of field segmentation. Once the variable of interest is identified, the next step is to set a threshold value. This introduces a scientific challenge, opening the door to the broad field of segmentation studies. For example, plotting the ratio of the maximum structure volume to the total volume as a function of the threshold value often results in a bathtub-shaped curve, with high volume ratios at both small and large thresholds. Choosing an appropriate threshold is crucial to avoid the segmentation of large structures that percolate the entire domain. Optimal thresholds typically lie at intermediate values, minimizing the volume ratio. Additionally, studying the influence of the threshold on the statistical properties of the structures is essential. This could involve categorizing results based on different fluctuation levels. Finally, structure detection for any given segmentation method must be complemented by a robust identification algorithm. This algorithm should connect structures across different time instants, treating them as the same object. It achieves this by traversing the field and identifying corresponding regions over time (Jiménez, 2018a).

These foundational ideas, widely used in turbulence research, will form the basis for the analysis of our data.

In our reactive problem, a percolation threshold based on a fixed value of the reaction rate is used to segment the field. Although a transient process is under study, the homogeneous character of data enables the use of fixed threshold values, taking into account that the main goal is the identification and tracking of different flame kernels. Regarding the segmentation variable, the reaction rate represents adequately the flame front. Other flow variables such as temperature or species mass fraction could also define the kernel structures, but the chemical production term presents sharper gradients that grant a neat separation of the two tips of the double structure. This fact will help to study the evolution of independent kernels into double structures through merging and reorientation processes. Regarding the exact value of the threshold, fig. 5.4 offers a visual reference, showing different possible cut-off levels, $\Omega/\rho = [0.5,\ 5,\ 50]$ for circular (left panels) and double-cell solutions (right panels). $\Omega/\rho = 5$ is chosen to approximately provide a representative shape of the flame fronts. The highest value does not detect flames in its weakest form or the lateral reaction in the intense cases,

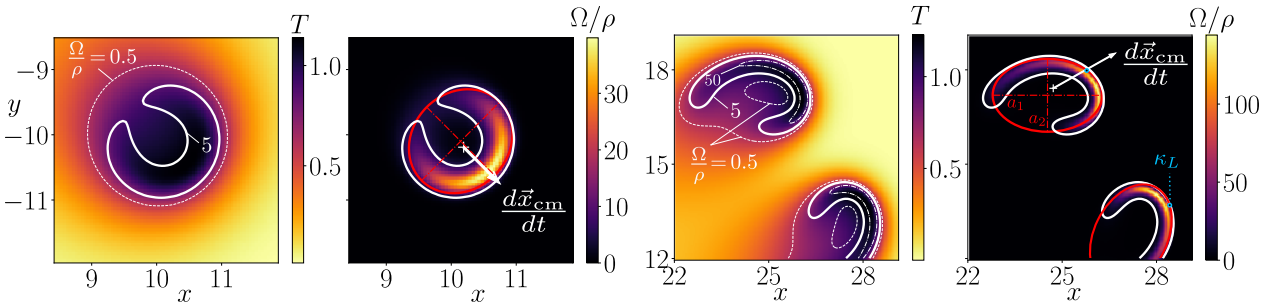

Figure 5.4: Sample temperature map and reaction-rate thresholds in a circular (left) and double flame (right) for $\Omega/\rho = [0.5,\ 5,\ 50]$. Reaction-rate maps include the detection threshold (white contour), ellipse fitting (red) and propagation direction (white arrow).

while the lowest threshold includes wide areas where the species and temperature values show that the production term is barely acting.

Once the field is segmented at every integrated time step, the kernels are identified and tagged. Then, a tracking system can provide the temporal evolution for a variable linked to each flame kernel. This part involved the development of an in-house tracking code. The main idea is that the structures in the binarized segmented fields between two consecutive time steps can be coherently labeled, making use of an adjacency matrix. Given that a particular element is identified all over the computed time, variables associated to this structure can be analyzed along its evolution. The fronts are followed over time, providing the displacement of their centroids $\mathbf{x}_{\mathrm{cm}}(t)$, associated propagation direction, and time evolution of spatial-averaged variables inside the structure (mean, maximum and minimum temperature and species). Moreover, each flame is fitted with an ellipse in a least-squares sense, which enables the approximate calculation of their front curvature,

$$\kappa(\theta_e) = \frac{1}{a_1^2 a_2^2}\left(\frac{\cos^2(\theta_e)}{a_1^2} + \frac{\sin^2(\theta_e)}{a_2^2}\right)^{-\frac{3}{2}}, \tag{5.3}$$

with a_1 and a_2 the semi-major and semi-minor axis respectively, and θ_e the parametric angle of the ellipse. Therefore, the maximum curvature is aligned with the semi-major axis, $\kappa_{\max}(0) = a_1/a_2^2$, and the minimum curvature $\kappa_{\min}(\pi/2) = a_2/a_1^2$ oppositely. In particular, the curvature at the point of the ellipse aligned with the structure's direction of propagation, κ_L, is analyzed as additional morphological information of the front dynamics. It should be noted that both substructures in double-cell cases are separately fitted with two ellipses, with the corresponding information in the following sections applying to each of them. Appendix C gives a deeper explanation on how the clustering process works and the methodology to draw a temporal evolution of the variables.

5.3 Symmetry-breaking routes

The steady-state propagation for each pair of ignition parameters $[N,\ T_0]$ is achieved after a transient process, which is dominated by the aforementioned specific dynamics such as oscillations, splittings and merging events. Modifications of the energy deposition intensity

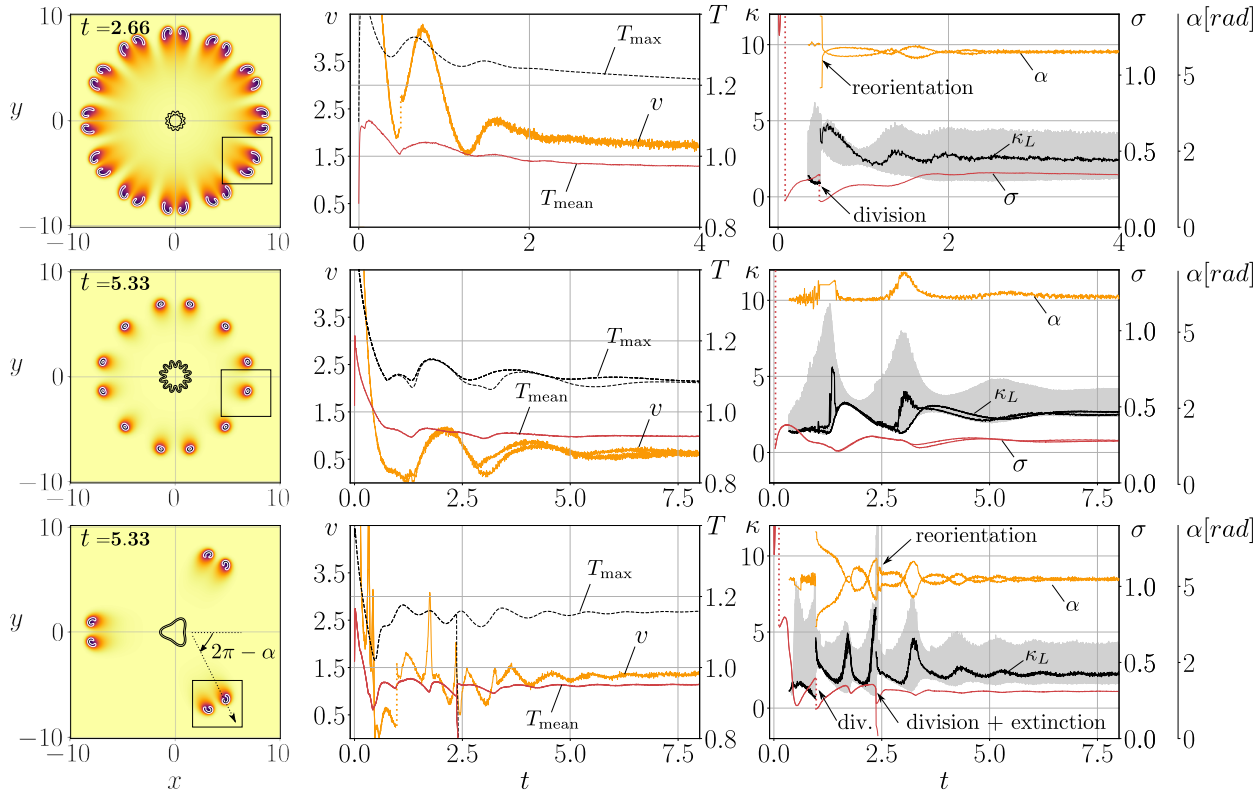

Figure 5.5: Structure evolution comparison between: $T_0 = 1.1,\ N = 12$ (top row), $T_0 = 1.5,\ N = 12$ (middle row) and $T_0 = 1.5,\ N = 3$ (bottom row) for $q = 5,\ b = 1$. Instantaneous temperature field (colormap $T \in [0, 1.1]$) with black isocontours of initial structures at $t = 0.01$ (left). Temporal evolution of the mean and maximum temperature and propagation velocity (center). Evolution of area σ, curvature κ_L and propagation angle α (right).

by T_0, and geometry through the number of lobes N of the initialization, force different cascades of events. Figure 5.5 tracks and analyzes in detail three ignition cases for fixed thermo-chemical parameters $q = 5$ and $b = 1$. Each row presents a simulation case $N = 12$, $T_0 = 1.1$ (top), $N = 12$, $T_0 = 1.5$ (mid), and $N = 3$, $T_0 = 1.5$ (bottom). Left-column panels depict the temperature field at a characteristic computational time when the steady solution is reached, with superposed reaction-rate contours at $t = 0.01$ to depict a stage of early initialization. The temporal evolution of some flow variables associated with each detected kernel appears in the central column, T_{mean} (red), T_{max} (black dashed) and the propagation velocity v (orange) of the centroid. Last, the areas of the detected structures, σ (red), are calculated via the sum over the regular physical mesh of the segmented region meeting the aforementioned threshold $\Omega/\rho > 5$. Their curvature regarding ellipse fitting $[k_{\text{min}},\ k_{\text{max}}]$ (gray envelope), and propagation direction k_L (black solid) through definition of the propagation angle α (orange) are presented in the right-column panels.

The vast information contained in fig. 5.5 enables the identification of flame divisions, oscillations, partial extinctions, merging, and either circular or double solutions. Top-row panels show the formation of double-cell flames with $T_0 = 1.1$ and $N = 12$, which can be compared

with the evolution towards circular flames in mid-row panels for an increase in initiation temperature $T_0 = 1.5$ and equal number of lobes. Note that the latter generates a stronger initial expansion that can be identified from the larger radius of early-stage front (black isocontours at $t = 0.01$) in the left panels. This effect blows the reaction kernels to colder regions in the radial direction at different rates. Therefore, although a noticeably lower T_{mean} for $t \lesssim 0.5$ is observed in the $T_0 = 1.1$ case at the top-central panel, the mean temperature of fragmented structures with $T_0 = 1.5$ decays faster below $T_{\text{mean}} = 1$. That temperature decrease also translates into a nearly complete deceleration of the burning rate and a slower propagation of the weaker circular type, as compared by $v(t)$ in the central-column panels.

Oppositely, double-cell structures in top panels of fig. 5.5 are formed after a splitting event at $t \simeq 0.5$, characterized by a discontinuity in area evolution $\sigma(t)$ in the right panel. Later, a reorientation process on the propagation direction $\alpha(t)$ of two neighboring structures is produced. The longitudinal curvature κ_L of the double cells, lies somewhere in between the maximum and minimum available values as a consequence of the tilted nature of the elliptic fitting. However, the circular fronts of the mid-row panels show a strong coupling of the propagation direction with the semi-minor axis. The intensity of the initial expansion, controlled here through T_0, produces different final stages owing to the relative convective field induced during the transient.

Additionally, the ignition shape effect on the local environment of the transient flames is explored via number of lobes N, paying attention to the dynamics of interaction between kernels. The generation of double cells with $N = 3$ and $T_0 = 1.5$ is shown in the bottom row of fig. 5.5, in contrast with circular fronts of the aforementioned simulation with $N = 12$. The initial fragmentation of the flames from the starting tri-lobular front produces kernel areas $\sigma(t \simeq 0)$ three times larger than for $N = 12$. This difference shapes the subsequent evolution of the $N = 3$ case towards a second splitting event at $t \simeq 1$ in the bottom-right panel. In this case, an oscillatory reorientation can be noted from $\alpha(t)$, which merges towards the double-cell parallel propagation owing to a small seeding and partial extinction at $t \simeq 2.5$.

The characteristic size of the front after the initial expansion also plays an important role in the number, frequency and sequence of splittings, which usually produce fragments that start to separate and require additional interactions to form a double-cell structure. The history of this transient dynamics is defined by subtle details that modify the propagation direction and determine the final stable form of the front.

The key processes that separate the pathways of formation of each stable structure are mainly affecting the spatial distribution of the fronts and the local velocity field. The appearance of circular flames is preceded by nearly symmetric front splittings with respect to the propagating direction. These characteristic events are typically represented by a strong transverse deformation that gives way to the break-up via a local stagnation point. The stretched part of the front extinguishes, while the remaining fragments travel outwards separating apart and gaining curvature as nearly circular isolated fronts. For instance, the first fragmentation from the lobular structure is of this kind in most cases analyzed. In contrast, double cells require the adequate parallel propagation of two isolated kernels, which originate from splitting events or different precursors, producing two stable coupled flames that benefit from a hot region of their twin structure nearby. In fact, two different mechanisms

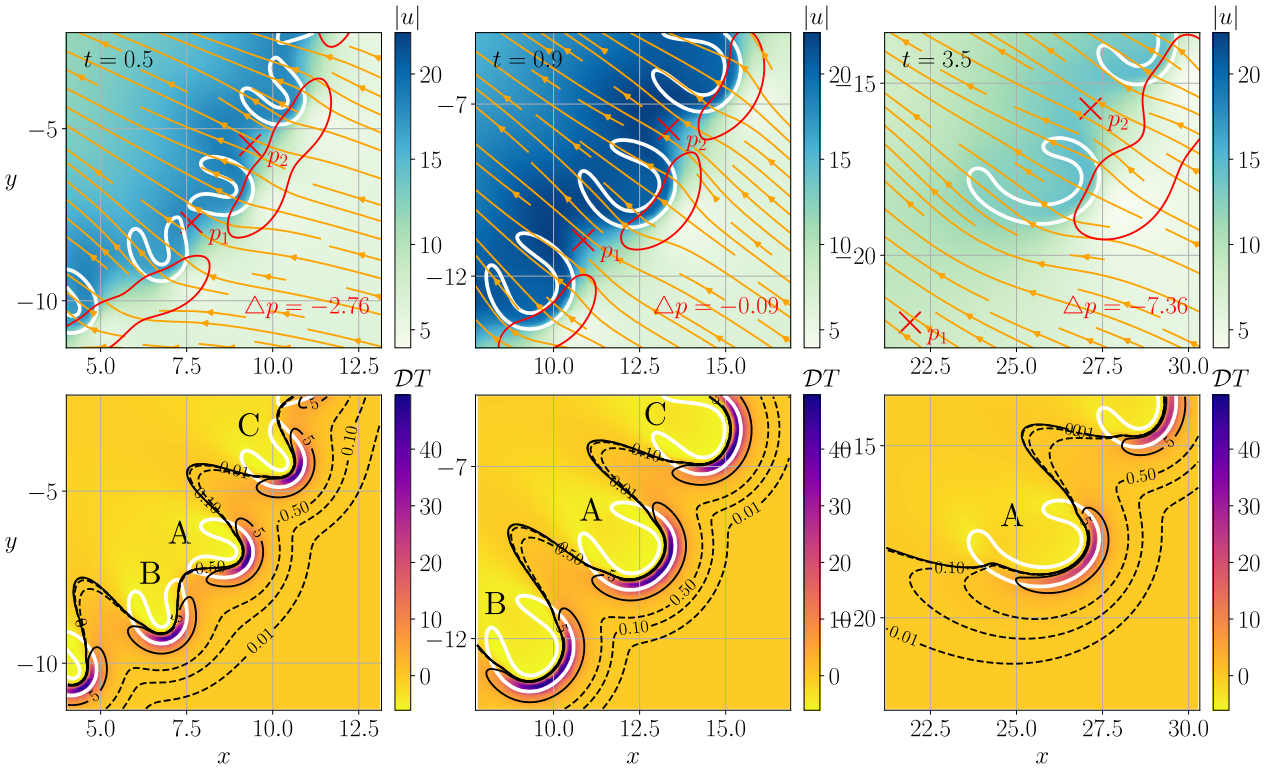

Figure 5.6: Merging transient snapshots of (Ω/ρ)-threshold structures in white contours for $q = 5$, $b = 1$, $N = 12$ and $T_0 = 1.1$. (Top) Velocity magnitude in flame reference frame and streamlines (orange) with pressure isolines (red). (Bottom) Material derivative of the temperature field.

of reorientation are here identified and analyzed: the lateral interaction with neighboring flames; and seeding oscillatory dynamics.

First, the reorientation process through confinement is depicted in fig. 5.6 over the instants $t = [0.5, 0.9, 3.5]$, for the case $q = 5$, $b = 1$, $T_0 = 1.1$ and $N = 12$. The local velocity field and streamlines (orange) in the flame reference frame are plotted together with isocontours of local pressure minima (red) in left panels. The midpoints between structures are marked with red crosses and the pressure difference, $\triangle p = p_2 - p_1$, is evaluated. Moreover, the material derivative of temperature $\mathcal{D}T$, LHS of eq. (3.37), is shown in right panels with a few reference values in black contours ($\mathcal{D}T = 0$ solid black) to describe the evolution of the reaction rate and, thus, the detected structures (white).

The evolution starts with flame subdivisions, which travel apart after splitting (top row). Note that the divided front $(A - B)$ forms a greater pressure spot than the region within the adjoining flame $(A - C)$, so the fragments start to diverge (note the streamline direction) due to the pressure gradient and greater $\mathcal{D}T$ near the neighboring structure. At the intermediate stage, fig. 5.6 (mid row), the central structure (A) has approached the adjoining flame (C) and experiences a nearly symmetrical flow and temperature field, with very subtle variations due to the history and distance between kernels. These almost negligible variations in pressure $(\triangle p \simeq 0.1)$ and temperature break the symmetry of the evolution and force the coupling in

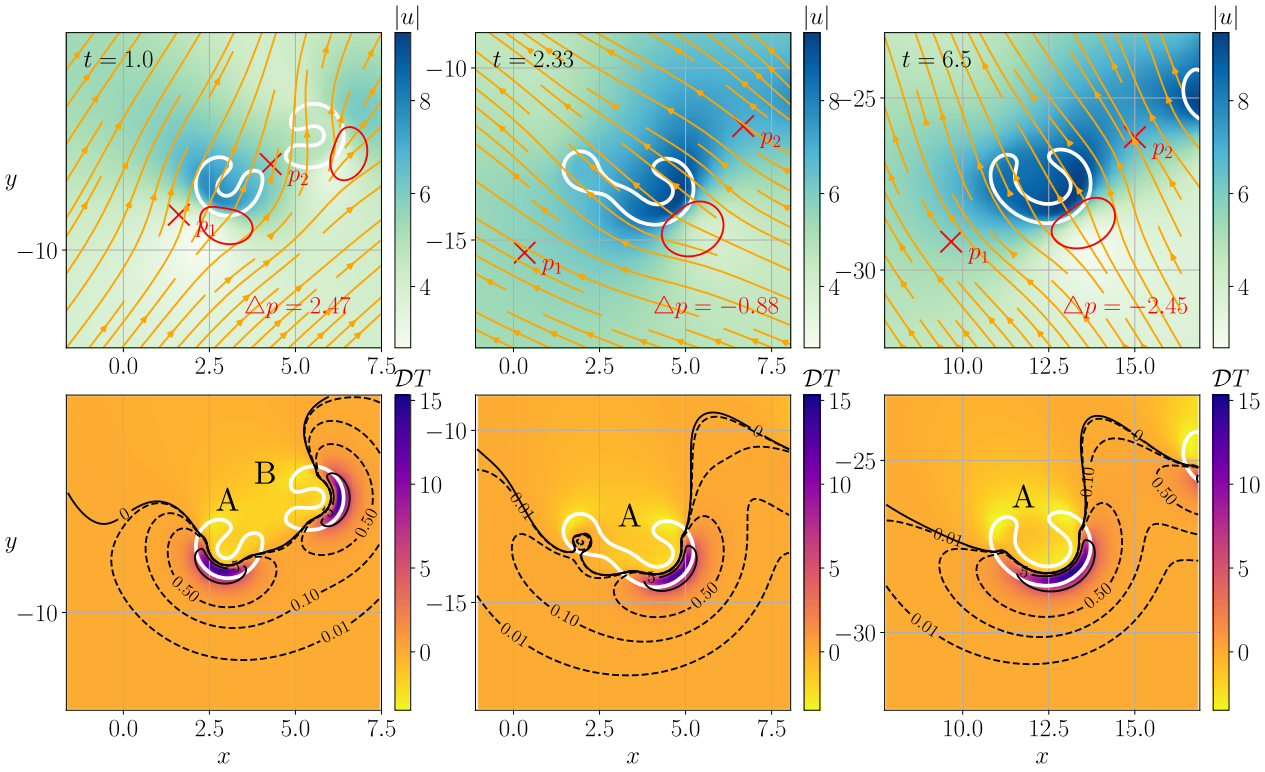

Figure 5.7: Oscillatory transient along three snapshots of Ω/ρ-threshold structures in white contours for $q = 5$, $b = 1$, $N = 3$ and $T_0 = 1.5$. See fig. 5.6 caption for top and bottom panels.

the propagation direction with the upper flame (bottom row) originated from a different lobe.

However, other unsteady processes, such as flame oscillation and seeding can generate similar double structures from the fragments of a common precursor lobe. In fact, fig. 5.7 shows this kind of transient for $q = 5$, $b = 1$, $N = 3$ and $T_0 = 1.5$ at instants $t = [1, 2.3, 6.5]$. First, the lobe breaks in two fronts that tend to separate (top row). In the absence of a neighboring structure the reorientation is based in the preference of propagation towards the warmer region between the fragments. This progressive turning continues until a piece of the structure's tail, much smaller than the precursor flame, is detached producing a local modification of the flow field (mid row). The extinction of that seeding pushes slightly the isolated flames apart, via small transverse gradients of pressure and temperature. This reorientation mechanism is produced cyclically (see bottom-right panel in fig. 5.5) until parallel propagation with its twin structure is achieved $\alpha_A = \alpha_B$. The competition between reorientation and cooling, through off-plane conductive heat losses and heat release, should define a threshold in the separation distance of fragments were merging cannot be ensured and circular kernels that drift apart are recovered.

All things considered, the formation of double flames are conditioned not only by the adequate composition of front shape and flow field, but also by a high sensitivity to the heat transfer problem. Intense enough response needs to be ensured through the balance of heat release to losses in the evolving local field. Small enough values of q and large values of b can only grant

the generation of circular flames in absence of splitting or oscillating transients, in accordance with previous results.

5.4 Irregular ignition cases

Regular ignition patterns have been instrumental to understand the role of transient dynamics in the formation of the characteristic stable kernels. However, these sets of simulations form either one or the other of the two possible solutions after the unsteady initiation. Therefore, irregular ignition conditions are proposed to force the bi-stable behavior in the same simulation. Analogous central ignition configurations based on a hot spot and a corresponding species depletion are used, though altering the lobular shape by superposition of sinusoidal functions of a series of lobe numbers whose phase shift is constructed from pink noise signals. This introduces the necessary stochastic component in the initial conditions,

$$T(t=0) = T_0 \exp\left\{-\frac{r^2}{10}\left[1 + \sum_{i=1}^{m} \frac{\cos(N_i\theta + 2\pi\varepsilon_i)}{2}\right]\right\}, \tag{5.4}$$

$$Y(t=0) = 1 - \exp\left\{-\frac{r^2}{10}\left[1 + \sum_{i=1}^{m} \frac{\cos(N_i\theta + 2\pi\varepsilon_i)}{2}\right]\right\}, \tag{5.5}$$

which describe the irregular initialization in these cases. Particularly, a number m of different modes defines the size of the array N_i, including the values of the number of lobes of each mode $N_i = [2,\ 5,\ 10,\ 15,\ 20,\ 25,\ 30]$, where $\epsilon_i \in [0,\ 1]$ is a computer-generated random shift of each mode. Figure 5.8 shows four irregular ignition cases, where the random function ϵ is varied. Double structures are easier to observe, their higher propagation velocity makes the circular kernels to lag behind, immersed in the wake of combustion products and undergoing extinction events due to fuel lack. The isolated circular flames captured in these simulations are favored by fortuitous initial distributions that leave enough unburnt space on the sides of the kernel.

Finally, fig. 5.9 highlights the irregular character of ignition required for the development of multiplicity of stable solutions. The initialization from regular lobes with $N = 8$ (left) and $N = 12$ (center) may form different isolated and steady propagating structures, double and circular respectively. However, an irregular composition of modes (right) following the aforementioned strategy gives rise to both types of kernels on the same run. The irregularities during the ignition process produce the necessary variations in the flow field to facilitate the emergence of both single and double flames over the same thermo-chemical parameters. The segmentation process described above yields similar results to the ones displayed in fig. 5.5, although one single line in the temporal progression of the irregular case cannot be expected.

These kind of initial profiles are more representative of the actual initiations of experimental configurations, where sparks and glow-plug irregularities may induce perturbed initial reaction fronts that can be fragmented into several types of kernels. In fact, these ideas have been proposed to be tested and validated experimentally, driving new experiments that confirm these observations in horizontal Hele-Shaw chambers with lean hydrogen-air mixtures (Palomeque-Santiago et al., 2024).

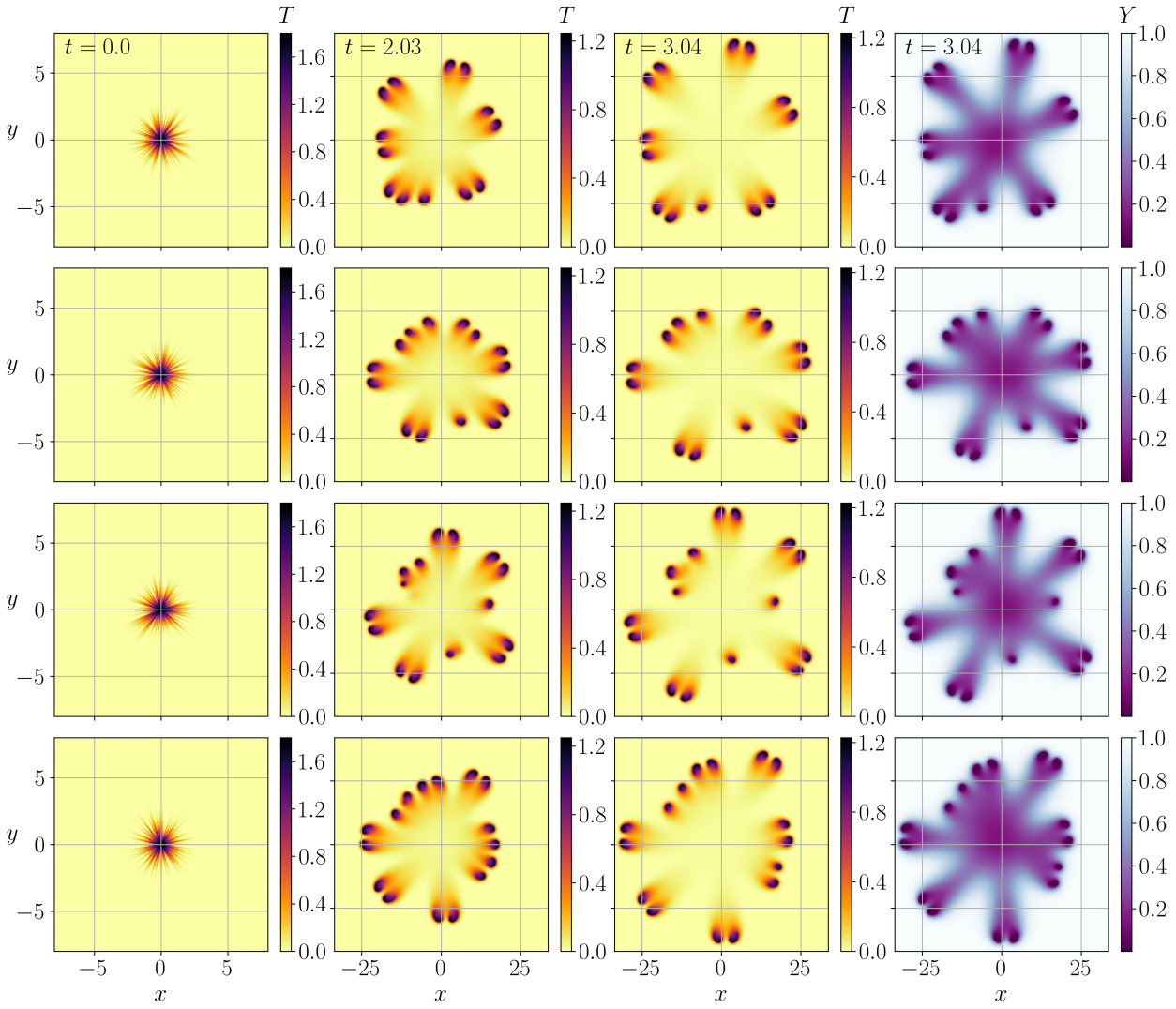

Figure 5.8: Time evolution of four irregular initiation cases (rows), for $T_0 = 1.8$ and azimuthal modes of lobes $N_i = [2,\ 5,\ 10,\ 15,\ 20,\ 25,\ 30]$ with random noise shifts, and fixed thermo-chemical parameters $q = 5,\ b = 1$. Three instants displayed $t = [0,\ 2.03,\ 3.04]$

5.5 Flame propagation over forced perturbation velocity fields

Another type of transient flow is computed from the forced superposition of a fictitious velocity field, not evolving in time, to the regular central ignition. Therefore, the resulting field is composed by a main flow velocity **u** owing to the physical equations through the flame-induced thermal expansion, and the additional velocity fluctuation field **U**.

Several scenarios of base field velocity fluctuation have been computed, and two sample cases are presented here. The first one, case A, represents a moderate-intensity large-scale fluctuation compared to the flame thickness and is presented on the left-side panels of fig. 5.10. In contrast, right-side panels depict case B, which is a small-scale and hight-

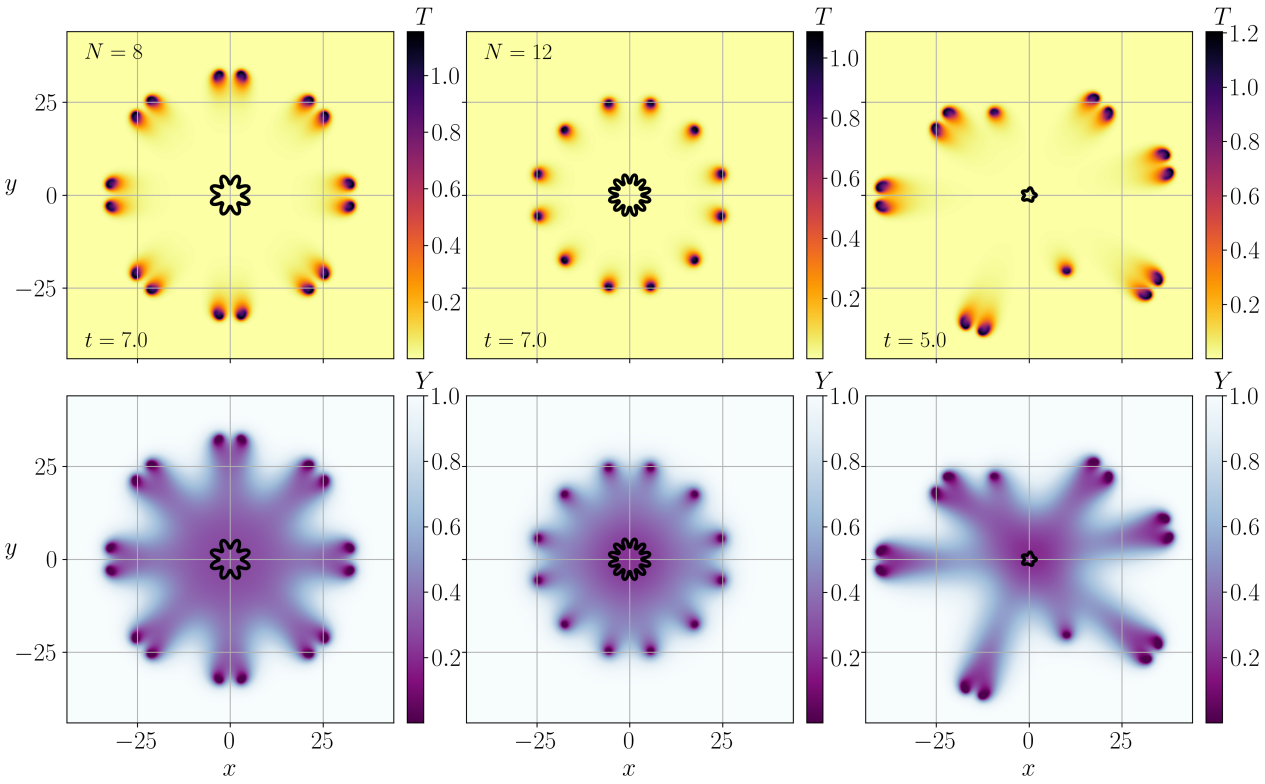

Figure 5.9: Numerical simulations for $q = 5$, $b = 1$ and different initiation conditions with $T_0 = 1.8$, and $N = 8$ (left), $N = 12$ (center), and irregular composition of modes $N_i = [2, 5, 10, 15, 20, 25, 30]$ (right) distributions. Dimensionless temperature profiles at selected instants are shown (top) together with the reactive species field (bottom).

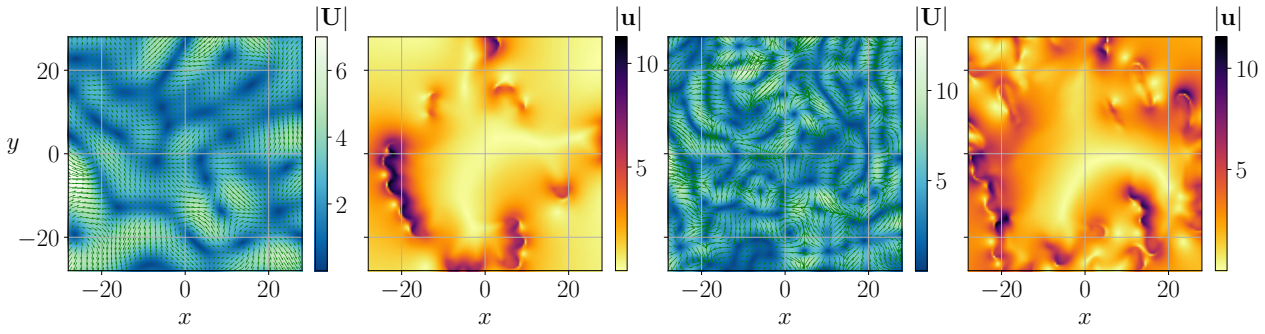

Figure 5.10: Perturbation cases A (left panels), and B (right panels). Modulus of the fluctuation velocity field $|\mathbf{U}|$ in blue color map, green arrows mark the perturbation direction. Orange color map for the modulus of the velocity field as computed from the thermal expansion $|\mathbf{u}|$.

intensity fluctuation scenario with larger velocity values than the thermal-expansion speed $\mathbf{u}$ calculated at a specific time instant of the simulations. Details of the forcing fields are given in Table 5.2. First, the turbulent kinetic energy $k = 0.5\,(U_x + U_y)$ and its dissipation rate $\epsilon = 1/\rho\,(\partial U_x/\partial y + \partial U_y/\partial x)$ are provided. The Kolmogorov scales can then be related

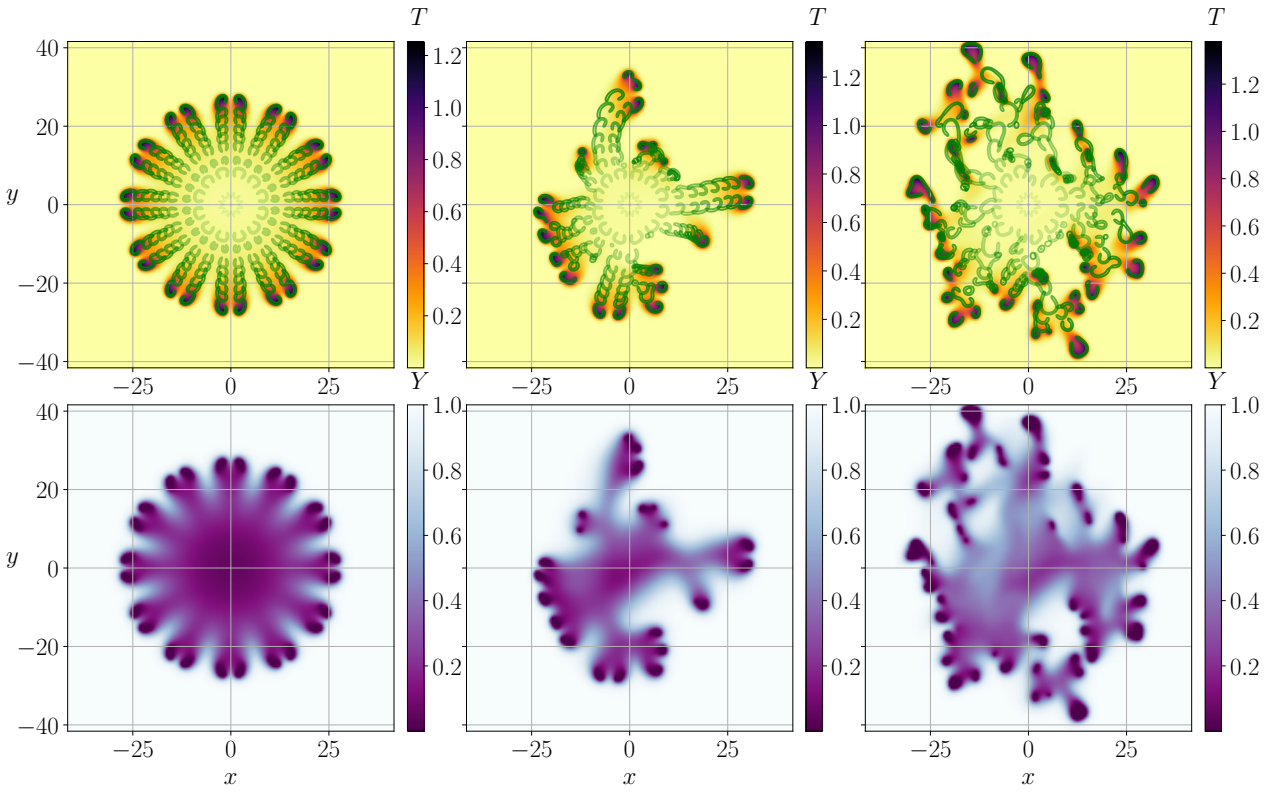

Figure 5.11: Temperature (top) and species mass fraction (bottom) comparison between a regular base case without forced perturbation velocity field(left), case A (center) and case B (right) for $q = 5,\ b = 1,\ T_0 = 1.1,\ N = 12$ at time step $t = 2.5$.

Table 5.2: Fluctuation field characterization data for case A and case B at $t = 2.5$.

	k	ϵ	u_k	η_k	τ_k	$\lvert U\rvert_{\max}$	$\lvert U\rvert \,/\, \lvert u\rvert_{\max}$
Case A	3	0.17	0.64	1.55	2.4	7	0.63
Case B	9	2.17	1.21	0.82	0.68	12.97	1.28

to the characteristic problem scales, such as the planar flame velocity and the thermal thickness. In addition, the chemical characteristic time prescribed by Arrhenius 1-step kinetics is $t_{\text{chem}} = (2\text{Le}/\,(1+q)^2\,\beta^2)(\delta_T/S_l) = 1.2e-05$, which enables the definition of Damköhler and Karlovitz numbers. Specifically, for case A, $\text{DaA} = 1.43 \times 10^6,\ KA = 5 \times 10^{-6}$, and for case B, $\text{DaB} = 3.44 \times 10^5,\ KA = 1.8 \times 10^{-5}$.

Figure 5.11 shows the comparison of temperature (top) and species (bottom) distributions between three simulation cases at $t = 2.5$, with an evolution of the isocontours of reaction rate for specific intermediate times. Namely, a regular transient without velocity perturbation forcing (left column), case A (central column) and case B (right column) of these two cases. The perturbation intensities are large enough to create changes in the flow direction. In both cases, the flame continues to dominate the dynamics regardless of the fluctuation velocity field, and the laminar character of the kernel is not lost with turbulent scales not altering the flame structure (small Karlovitz numbers). The role of the fluctuation velocity field imposed is to act

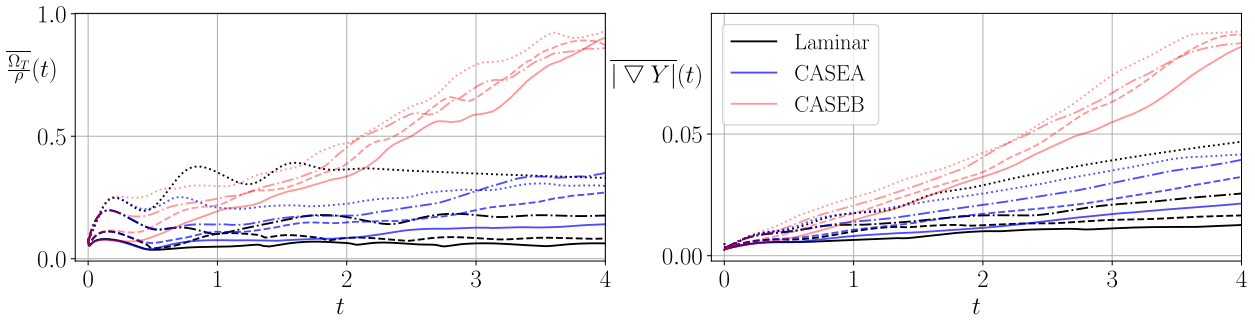

Figure 5.12: Temporal evolution of the averaged consumption rate (left), and the norm of the species gradient (right). Comparison between laminar (black), case A (blue) and case B (red). Lobular ignition is applied with $N = 3$ (continuous), $N = 4$ (dashed), $N = 8$ (dash-dot) and $N = 12$ (dotted).

as an advection guide along which the flames are sliding, since the characteristic scale of the fluctuation does not interact with the flame. For the weak forcing of case A, the appearance of a canonical double-cell structure at $[x, y] = [-20, 0]$ is observed in fig. 5.11 (center). However, if the 'turbulent' imposed field is intense enough, the two steady configurations are lost and a chaotic spatial kernel disposition is observed for case B (right). In this case, the velocity perturbation drives the transient propagation and interaction between the isolated kernels.

The fluctuation component promotes successive splitting and interactions between the kernels, driven by inertial forces. In general, the chaotic pattern that the kernels follow is produced by the fluctuation fields, which promotes a more spatially extended burning. The structures spread covering more part of the domain, enhancing the mixing process, as noticed by the extensive purple area of consumed reactants in fig. 5.11 (bottom).

Finally, fig. 5.12 displays the temporal evolution of the averaged consumption rate and the norm of species gradient of the entire domain as a measure of the dissipation rate. The unperturbed laminar case, case A and case B are compared, with $N = [3,\ 4,\ 8,\ 12]$. In general, an increase is observed for both indicators in time, its growth increasing from laminar to case A to case B. The perturbation in the velocity field excites the reactive kernels, also promoting a higher level of mixing behind the wake. Nevertheless, the initiation with $N = 12$ is a particular case, where the strong thermal expansion of the ignition in the unperturbed laminar configuration gives rise to a front that, although fractured, propagates radially following a structured and connected pattern that leaves little amount of unburnt domain, see fig. 5.11. Therefore, in moderate distances, as defined by the present numerical domain, certain unperturbed spatial arrangements of kernel structures can burn faster than 'turbulent' fields where the advected spatial arrangement of flame fronts is more randomly disposed.

5.6 Transient dynamics remarks

The numerical experiments in this work reveal distinct paths in the formation of stable lean hydrogen premixed flames in presence of heat losses. The importance of symmetry-breaking mechanisms is highlighted during the dynamical evolution of the flames and a wide variety of

events is identified, in the form of structure splitting, oscillation, reorientation and seeding. In addition, the stable propagation outcomes are conditioned by the details of the transient process, which are very responsive to perturbations in the flame shape, local temperature and pressure/velocity field. These perturbations can arise anytime from multiple origins during the evolution history after ignition. Therefore, circular and double cell fronts are both feasible from realistic non-ideal scenarios, characterized by uncontrolled random initiations that cannot ensure the absence of perturbation noise. Specially, the pathway to double-cell flames requires a first splitting and a subsequent reorientation process of individual flames either by seeding-oscillation or lateral interaction with confining neighboring flames. In addition, flow perturbations can promote a variability of events that lead to similar isolated flames while preserving the overall properties of canonical kernels, which is key to point out their stable nature. Nevertheless, very intense perturbations can cause the disruption of the structures and lead to complete unordered and unsteady flame patterns.

Recent experimental studies by Elyanov et al., 2024 examine ignition transients in a narrow horizontal gap. Several series of infrared images are presented, varying the channel height (related to the heat-loss parameter) and the hydrogen volume fraction in the mixture (associated with the heat-release parameter). Despite the use of spark ignition, highly symmetrical patterns are observed, closely resembling those presented earlier in this chapter.

Chapter 6

Scales of circular flames

The numerical simulations presented above provide valuable insights into the primary processes governing the propagation of weak premixed hydrogen flames. However, an additional theoretical study is conducted in this chapter to deepen our understanding of these specific flame structures. An asymptotic analysis of the governing equations applied to the circular case proves to be instrumental in revealing the leading scales of the problem at hand. In fact, the nearly axisymmetric configuration facilitates the theoretical description through a low-Péclet $\mathrm{Pe} \ll 1$ analysis, where diffusion is considered to be dominant. In addition, the presence of major heat losses is highlighted here, deeply marking the structure outcome.

First, the disparity of scales inherent to the problem is exploited to develop a theoretical description based on asymptotic expansions of the flow field. Distinct physical effects dominate in specific locations, either the far convective field or the near diffusion-controlled field. Then, analytical solutions for the different flow regions are asymptotically matched within an overlap layer, where convergence to the same functional form is achieved.

Secondly, closure conditions are examined to derive a theoretical prediction of the problem. The circular isolated kernel is generally characterized by its radius, propagation speed, and front temperature $\left[r'_k,\ S'_u,\ T'_f\right]$. Previous numerical results in chapters 4 and 5 indicate that these quantities are directly influenced by specific thermo-chemical parameters related to the heat release, Q, conductive heat losses, b, and diffusive transport properties, Le.

This propagating configuration is thus characterized by one additional unknown compared to the quiescent spherical flame ball, namely, the drifting velocity. However, the number of physical conditions to be applied at the reaction layer remains the same as in the spherical problem (Fernández-Tarrazo et al., 2011). For this reason, the solution results in a relation of possible combinations between size and velocities instead of a unique flame-circle structure.

6.1 General assumptions

The Reynolds number, based on the drift velocity S'_u and the characteristic radius δ'_k is assumed to be small, consistent with the circular symmetry of the flame morphology. A ring-shaped reaction front requires a sufficiently strong diffusive effect, in charge of providing

unburnt mixture to the rear side of the flame. This refilling process relies on mass diffusion with negligible convective transport effects. Hence, the associated Péclet number is expected to be small, $\mathrm{Pe} = S'_u \delta'_k / D'_T \ll 1$, the central hypothesis of this analysis. Our previous numerical studies on the stable propagation of these structures result in Péclet numbers of order unity (Domínguez-González et al., 2023). In addition, experimental evidence in Palomeque-Santiago et al., 2024 shows isolated flame cells with radii of the order of 0.5 cm moving over a stagnant mixture at speeds about 5 cm/s, involving moderate Péclet numbers $\mathrm{Pe} \simeq 10$. Although it may not be much smaller than unity, a diffusion-controlled flow regime is observed in both cases. This is a well-known fact from asymptotic analyses, that convective effects are still negligible with respect to diffusive effects for order-unity and moderate values of the controlling parameter, as in the perfectly laminar Stokes flow over a sphere with $\mathrm{Re} < 22$, (Taneda, 1956).

Regarding the combustion process, we shall make us of the large-activation energy limit $\beta \gg 1$, for which the flame thickness tends to zero. The flame front is reduced to a discontinuity that separates the inner burnt part and the outer unburnt gas mixture. In addition, the set of equations is expressed in terms of polar coordinates, where the reactive front corresponds to a boundary located at a specific radius $r' = r'_k$ for the circular-flame hypothesis.

6.1.1 Narrow-channel formulation

The mathematical formulation follows a similar approach to that quasi-two-dimensional model developed in chapter 3. The polar coordinates take full advantage of the symmetry of the configuration and, since the object of study is a steady configuration, non-stationary terms are neglected in the flame-moving reference frame. Flow properties like viscosity and thermal diffusivity will be considered constant, with a Prandtl number $\mathrm{Pr} = \mu'/\rho' D'_T \sim \mathcal{O}(1)$. Moreover, the mass diffusivity coefficient of the deficient species (hydrogen) D'_i defines a low effective Lewis number value, $\mathrm{Le} = D'_T/D'_i = 0.3$.

For convenience, a different scaling of the dimensionless variables is introduced. The new characteristic length scale in the (x', y') plane is the yet-unknown circular flame radius r'_k, such that the dimensionless in-plane coordinates are $x = x'/r'_k$ and $y = y'/r'_k$. Nevertheless, the transverse coordinate is referred to the channel height, $z = z'/h'$. Velocities are referred to the propagation speed of the flame structure, $\mathbf{v} = \mathbf{v}'/S'_u$. Dimensionless gas density and temperature are respectively $\rho = \rho'/\rho'_u$ and $T = (T' - T'_u)/(T'_f - T'_u)$, where T'_f is the flame temperature and subscript $-u-$ denotes upstream values. The flame temperature is also unknown but it can reach near-adiabatic values in the combined presence of heat losses and preferential diffusion with a low Lewis number. In turn, the adiabatic temperature T'_a is prescribed by the heat released per unit mass of fuel burnt Q, which reads in dimensionless form $q = QY'_u/(c_p T'_u) = (T'_a - T'_u)/T'_u$ and is a function of the equivalence ratio ϕ through the mass fraction of unburnt fuel in the mixture Y'_u. Nevertheless, the naturally arising version of this controlling parameter in the following dimensionless formulation is

$$\tilde{q} = \frac{T'_a - T'_u}{T'_f - T'_u}. \tag{6.1}$$

It will be shown in the analysis that the differences between adiabatic and flame temperatures,

$(T_f' - T_u')/(T_a' - T_u') = 1 + \epsilon$, should remain small ($\epsilon \sim \mathcal{O}(\beta^{-1}) \ll 1$).

The quasi-two-dimensional formulation for the transverse-averaged flow variables is recovered in the narrow channel limit $(r_k'/h')^2 \gg 1$. The steady-state momentum equation can be rewritten as,

$$\rho \mathbf{v} \cdot \nabla \mathbf{v} = -\left(\frac{r_k'}{h'}\right)^2 \frac{\mathrm{Pr}}{\mathrm{Pe}} \left(\nabla p + 12\mathbf{u}\right), \tag{6.2}$$

with the hydrodynamic pressure adequately scaled in advance

$$p = \frac{\mathrm{Pe}}{\mathrm{Pr}} \frac{p'}{\rho_u' S_u'^2 \left(\frac{r_k'}{h'}\right)^2}. \tag{6.3}$$

The reader shall recall that the momentum equation is dominated by transverse viscous effects and the in-plane velocity components exhibit parabolic profiles $\mathbf{v} = 6z(1-z)\mathbf{u} + \mathbf{e}_x$ in the flame-moving reference frame. Therefore, $\int \mathbf{v} dz = \mathbf{u} + \mathbf{e}_x$ represents the unknown volumetric flow rate per unit line, which does not depend on the transverse coordinate z. Dominant viscous stresses can be directly computed as $\partial^2 \mathbf{v}/\partial z^2 = -12\mathbf{u}$.

In the viscous limit $\mathrm{Pe}/\mathrm{Pr} = \mathrm{Re} \ll 1$, the momentum equation in the near field, at distances $\mathbf{x} \sim \mathcal{O}(1)$, renders the relation $\mathbf{u} = -\nabla p/12$, where pressure acts as a potential of the velocity (volumetric flow rate). In the far field, at distances $\mathbf{x} \sim \mathcal{O}(\mathrm{Pr}/\mathrm{Pe}) \gg 1$, the mass flow rate equals $\rho \mathbf{v} = 1\mathbf{e}_x$. All things considered, we shall prove in the following that although the local velocity field may differ substantially from the homogeneous far-field inflow, the description of the weak circular flame remains unaltered.

The $z-$integrated quasi-two-dimensional equation of species and equation of energy in the (x, y) plane read,

$$\rho(\mathbf{u} + \mathbf{e}_x) \cdot \nabla Y = \frac{1}{\mathrm{PeLe}} \nabla^2 Y - \Omega, \tag{6.4}$$

$$\rho(\mathbf{u} + \mathbf{e}_x) \cdot \nabla T = \frac{1}{\mathrm{Pe}} \left(\nabla^2 T - \tilde{b} T\right) + \tilde{q}\Omega. \tag{6.5}$$

The heat flux from the hot gas through the walls surface depends on the heat-loss parameter

$$\tilde{b} = \left(\frac{r_k'}{\delta_T'}\right)^2 b = \left(\frac{r_k'}{\delta_T'}\right)^2 \left(\frac{\delta_T'}{h'}\right)^2 2\frac{\lambda_w h'}{\lambda h_w'}, \tag{6.6}$$

which arises naturally from the transverse integration process of the energy conservation equation presented in chapter 3. Nevertheless, the new heat-loss parameter $\tilde{b}$ is proportional to the unknown flame radius squared, owing to the new scaling. Contrarily, b can be considered fixed and collects the properties linked to the setup as presented in previous chapters. Off-plane conductive heat losses are thus proportional to the dimensionless temperature jump $\tilde{b}T$.

The three dimensionless controlling parameters appearing in the equations: off-plane conductive heat losses, dimensionless heat release, and Péclet number $[\tilde{b},\ \tilde{q},\ \mathrm{Pe}]$; involve the three unknowns of the problem $[r_k',\ S_u',\ T_f']$.

6.2 Asymptotic analysis

Considering the low-Péclet limit, eqs. (6.4) and (6.5) are controlled by diffusion effects in the flow field close to the flame $r = r'/r'_k \sim \mathcal{O}(1)$, with negligible convection terms. For the far field $r \sim \mathcal{O}(\mathrm{Pe}^{-1})$, the convective effect is noticeable, though the flow field is unperturbed by the flame cell. This asymptotic scaling analysis provides the separation of regions and behavior of the fluid variables.

6.2.1 Near-field description

In the large activation energy limit, the reaction region is reduced to a thin surface of vanishing thickness as $\beta \to \infty$. The flame sits at $r = 1$ and separates two inert regions, with reactive mixture on one side ($r > 1$) and hot products on the other ($r < 1$). Therefore, the mass and heat transport problems, describing the flow outside the reaction sheet, correspond to eqs. (6.4) and (6.5) with zero reaction rate ($\Omega = 0$). The solution to the diffusion-controlled zone requires the integration of the energy and species conservation equations as $\mathrm{Pe} \ll 1$, namely

$$\frac{1}{r}\frac{\partial}{\partial r}\left(r\frac{\partial Y}{\partial r}\right) + \frac{1}{r^2}\frac{\partial^2 Y}{\partial \theta^2} = 0, \tag{6.7}$$

$$\frac{1}{r}\frac{\partial}{\partial r}\left(r\frac{\partial T}{\partial r}\right) + \frac{1}{r^2}\frac{\partial^2 T}{\partial \theta^2} - \tilde{b}T = 0. \tag{6.8}$$

First, the axisymmetric boundary conditions $\partial T/\partial r = \partial Y/\partial r = 0$ at $r = 0$, and $T-1 = Y = 0$ at the flame $r = 1$, hold for the burnt subdomain. Therefore, the analytic profiles of temperature and species are

$$T = \frac{\mathrm{I}_0\left(\sqrt{\tilde{b}}r\right)}{\mathrm{I}_0\left(\sqrt{\tilde{b}}\right)}; \quad Y = 0; \quad \text{for the inner burnt area } r < 1, \tag{6.9}$$

where I_0 is the zero-th order modified Bessel function of the first kind. Additionally, the unburnt region of the near field must reach $T - 1 = Y = 0$ at $r = 1$, and $T = Y - 1 = 0$ as $r \to \infty$, for free-stream conditions. Radial integration yields

$$T = \frac{\mathrm{K}_0\left(\sqrt{\tilde{b}}r\right)}{\mathrm{K}_0\left(\sqrt{\tilde{b}}\right)}; \quad Y = C_1 + C_2 \ln(r); \quad \text{for the outer unburnt area } r > 1, \tag{6.10}$$

with K_0 the zero-th order modified Bessel function of the second kind. However, this is known as the classic two-dimensional counterpart of the spherical flame ball, which involves an invalid solution for the integration constants C_1, C_2 that cannot satisfy the far field decay of species concentration in a stagnant field. Although conductive heat losses in the energy equation warrant a mathematical solution to the two-dimensional problem, the equation of species conservation calls for an additional physical term that allows the circumvention of the logarithmic miss-match, namely a drift of the reaction structure.

Most interesting, it allows the presentation of the analogy to Stokes' paradox in the following section, involving a logarithmic buildup at infinity, (Lagerstrom, 2013, pp. 106-118 & pp. 222-226). Therefore, small perturbations included through convection terms in the far-field region, $\zeta = r\mathrm{Pe} \sim \mathcal{O}(1)$, are needed to account for the adequate decay of temperature and species that match free-stream conditions.

6.2.2 Far-field description

This far region is located around $r \sim (\mathrm{PeLe})^{-1}$, and introduction of the stretched radial coordinate $\zeta = r\mathrm{PeLe}$ yields a parameter-free equation of species affected by homogeneous convective terms, $\rho\mathbf{v} = \mathbf{e}_x = \cos\theta\mathbf{e_r} - \sin\theta\mathbf{e}_\theta$. The far-field re-scaled equation reads,

$$\cos\theta\,\frac{\partial Y}{\partial\zeta} - \sin\theta\,\frac{1}{\zeta}\frac{\partial Y}{\partial\theta} = \frac{1}{\zeta}\frac{\partial}{\partial\zeta}\left(\zeta\frac{\partial Y}{\partial\zeta}\right) + \frac{1}{\zeta^2}\frac{\partial^2 Y}{\partial\theta^2}, \tag{6.11}$$

Analytical solutions can be found for this equation (Hieber and Gebhart, 1968), of the form

$$Y = C_3 - C_4\exp\left(\frac{\zeta}{2}\cos\theta\right)\{\mathrm{K}_0(...), \mathrm{I}_0(...)\} \tag{6.12}$$

where K_0 and I_0 describe the regions $r > 1$ and $r < 1$ respectively, and their arguments include the stretched coordinate ζ. So far, only one of the two integration constants can be determined, $C_3 = 1$, from the far-field boundary condition, $Y(\zeta \to \infty) = 1$. The remaining constant must be obtained through matching with the near-field solution where the boundary condition at the flame, $Y(r = 1) = 0$, applies.

An analogous study of the temperature distribution can be offered, with $\xi = r\mathrm{Pe}$ and the re-scaled conservation equation,

$$\cos\theta\frac{\partial T}{\partial\xi} - \sin\theta\frac{1}{\xi}\frac{\partial T}{\partial\theta} = \frac{1}{\xi}\frac{\partial}{\partial\xi}\left(\xi\frac{\partial T}{\partial\xi}\right) + \frac{1}{\xi^2}\frac{\partial^2 T}{\partial\theta^2} - \frac{\tilde{b}}{\mathrm{Pe}^2}T. \tag{6.13}$$

The analytic solution to this equation can also be written in an equivalent form to the species mass-fraction variable, with Pe and $\tilde{b}$ included in the arguments of the modified Bessel function,

$$T_{\mathrm{far}} = C\exp\left(\frac{1}{2}\xi\cos\theta\right)\mathrm{K}_0\left(\sqrt{\frac{1}{4} + \frac{\tilde{b}}{\mathrm{Pe}^2}}\xi\right). \tag{6.14}$$

6.2.3 Asymptotic matching

The description of the near- and far-field solutions is required for the development of asymptotic expansions and subsequent matching. First, the species expansions are considered

$$Y_{\mathrm{near}} = f_0(\mathrm{PeLe})\tilde{Y}_0(r) + f_1(\mathrm{PeLe})\tilde{Y}_1(r) + ... + g_0(\mathrm{PeLe})\hat{Y}_0(r,\theta) + g_1(\mathrm{PeLe})\hat{Y}_1(r,\theta) + ... \tag{6.15}$$

$$Y_{\mathrm{far}} = F_0(\mathrm{PeLe})\mathcal{Y}_0(\zeta,\theta) + F_1(\mathrm{PeLe})\mathcal{Y}_1(\zeta,\theta) + ... \tag{6.16}$$

which are built based on different series of functions: $\tilde{Y}_i$ and $\hat{Y}_i$ are the axisymmetric and non-axisymmetric functions of the near region; and $\mathcal{Y}_i$ the functions of the far region. These series represent the solution of eqs. (6.11) and (6.7) to different orders described through the pre-multiplier factors f_i, g_i and F_i that depend on the value of PeLe. Integration of the near-field symmetric part when PeLe $\ll 1$ provides again the logarithmic solution

$$\tilde{Y}_i = \tilde{C}_{1_i} + \tilde{C}_{2_i} \ln r.$$

For the first order-term $f_0 = 1$ and $\tilde{C}_{1_0} = 0$, owing to the boundary condition at the flame $Y(r = 1) = f_i \tilde{Y}_i = 0$. Subsequent terms of the inner series also require $\tilde{C}_{1_i} = 0$. However, $\tilde{C}_{2_i}$ will be determined from the far-field matching.

Regarding the convective region, all terms in eq. (6.12) are relevant to the leading order, and solutions take the form

$$\mathcal{Y}_i = \mathcal{C}_{3_i} + \mathcal{C}_{4_i} \exp\left(\frac{1}{2}\zeta \cos\theta\right) K_0\left(\frac{1}{2}\zeta\right),$$

where I_0 functions have been discarded to satisfy a bounded value at infinity. First-order terms comply with the boundary condition at infinity $Y(r \to \infty) = F_i \mathcal{Y}_i = 1$, so that $F_0(\mathrm{PeLe}) = 1$ and $\mathcal{C}_{3_0} = 1$. It must be noted that the following-orders first constant $\mathcal{C}_{3_i} = 0$, given that the second term, $\exp(\zeta/2 \cos\theta)\mathrm{K}_0(\zeta/2)$, goes to zero as $\zeta \to \infty$.

The matching approach involves the expression of the far-field solution particularized for $\zeta \ll 1$, where the azimuthal dependence is lost, and expanded in power series (Abramowitz and Stegun, 1964),

$$Y_{\mathrm{far}} \simeq 1 - \mathcal{C}_{4_0}\left[\ln(\mathrm{PeLe}) + \left(\ln\left(\frac{1}{4}\right) + \gamma\right) + \ln(r)\right] + F_1(\mathrm{PeLe})\mathcal{C}_{4_1}\left[\ln(\mathrm{PeLe}) + \left(\ln\left(\frac{1}{4}\right) + \gamma\right) + \ln(r)\right] + \ldots \quad (6.17)$$

being γ the Euler constant and recovering the dimensionless space variable $r = \zeta/(\mathrm{PeLe})$ for the coupling with the near region. Comparing the same order terms of the inner and outer solution, the pre-multiplier factors and the remaining integration constants are obtained. Expansion series for the inner and outer regions thus read,

$$Y_{\mathrm{near}} = \left[-\frac{1}{\ln(\mathrm{PeLe})} + \frac{\left(\ln\left(\frac{1}{4}\right) + \gamma\right)}{(\ln(\mathrm{PeLe}))^2} - \frac{\left(\ln\left(\frac{1}{4}\right) + \gamma\right)^2}{(\ln(\mathrm{PeLe}))^3} + \ldots\right] \ln(r) + \ldots \quad (6.18)$$

$$Y_{\mathrm{far}} = 1 + \left[\frac{1}{\ln(\mathrm{PeLe})} - \frac{\left(\ln\left(\frac{1}{4}\right) + \gamma\right)}{(\ln(\mathrm{PeLe}))^2} + \frac{\left(\ln\left(\frac{1}{4}\right) + \gamma\right)^2}{(\ln(\mathrm{PeLe}))^3} - \ldots\right] \exp\left(\frac{1}{2}\zeta\cos\theta\right) K_0\left(\frac{1}{2}\zeta\right) \quad (6.19)$$

It is rapidly seen that the terms in braces of the expansions above yield a geometric series whose summation is finite. Therefore, they can be rewritten as,

$$Y_{\mathrm{near}} = -\frac{\ln r}{\ln(\mathrm{PeLe}) + \ln\left(\frac{1}{4}\right) + \gamma}, \quad (6.20)$$

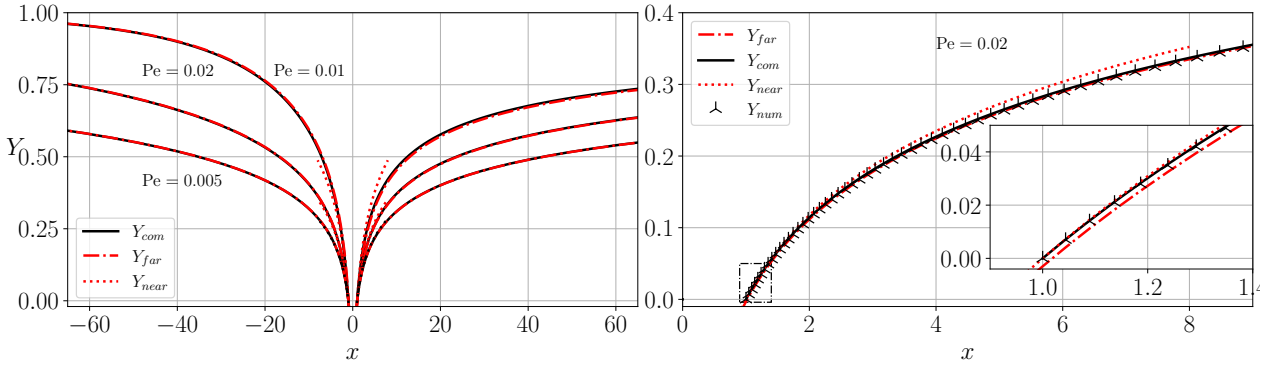

Figure 6.1: Left panel: Species concentration axial profiles for Pe $\in [0.005,\ 0.02,\ 0.01]$ comparing the complete solution (solid), far-field expansion (red dash-dotted) and near-field approximation (red-dotted). Right panel: zoom view, comparison between the analytical solutions and the numerical integration of the equation

$$Y_{\text{far}} = 1 + \frac{\exp\left(\frac{1}{2}\zeta\cos\theta\right)\mathrm{K}_0\left(\frac{1}{2}\zeta\right)}{\ln\left(\mathrm{PeLe}\right) + \ln\left(\frac{1}{4}\right) + \gamma}. \tag{6.21}$$

Finally, a complete analytical distribution of species can be obtained as a solution of eq. (6.11), out of the reaction sheet,

$$Y_{\text{com}} = 1 - \exp\left(\frac{1}{2}(r-1)\mathrm{PeLe}\cos\theta\right)\frac{\mathrm{K}_0\left(\frac{1}{2}r\mathrm{PeLe}\right)}{\mathrm{K}_0\left(\frac{1}{2}\mathrm{PeLe}\right)}. \tag{6.22}$$

Results are compared along the longitudinal axis in the left panel of Fig. 6.1 for various Péclet numbers and Le = 0.3. The right panel shows an additional comparison of the complete solution (solid black) with the numerical integration (symbols) of eq. (6.11) with Pe = 0.02 and Le = 0.3. The inset zoom shows that the near-field series perfectly agrees with the numerical solution at $x = 1$, where no azimuthal dependence has been required to match this order ($g_0 = 0$). This series progressively diverges from the complete profile for increasing distances, where the far-field expansion provides a great agreement with the complete result and convective effects in the wake of the structure impose a non-negligible azimuthal dependence. Specifics of the numerical integration can be found in Appendix D.

An analogous methodology is followed for the temperature variable, which is expressed in terms of the near- and far-field expansions,

$$T_{\text{near}} = f_0(\mathrm{Pe})T_0(r) + f_1(\mathrm{Pe})T_1(r) + ... + g_0(\mathrm{Pe})\hat{T}_0(r,\theta) + g_1(\mathrm{Pe})\hat{T}_1(r,\theta) + ..., \tag{6.23}$$

$$T_{\text{far}} = F_0(\mathrm{Pe})\mathcal{T}_0(\xi,\theta) + F_1(\mathrm{Pe})\mathcal{T}_1(\xi,\theta) + ... \tag{6.24}$$

The order of magnitude of the different f_i and g_i in the near-field temperature have to match F_i, that arise in the far-field solutions. The conductive heat-loss sink term in the energy conservation equation, $-\tilde{b}T$, remains the only difference enabling the near-field axisymmetric temperature distribution in eqs. (6.9) and (6.10). These approximate solutions do not involve

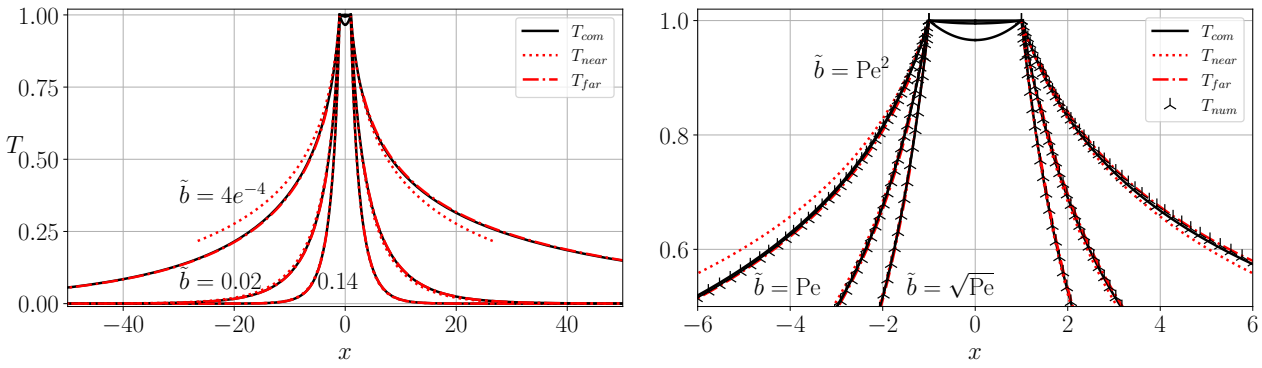

Figure 6.2: Longitudinal cut (y=0) comparison for a fixed $\mathrm{Pe} = 2 \times 10^{-2}$ and $\tilde{b} = \left[\sqrt{\mathrm{Pe}},\ \mathrm{Pe},\ \mathrm{Pe}^2\right]$. Complete solution (solid), near-field expansion (dotted), far-field expansion (dot-dashed) and numerical solutions (symbols).

further difficulties associated with incompatibility of boundary conditions, contrarily to the species distribution. The analytical solution for temperature in the far-field region, $\xi \sim \mathcal{O}(1)$, reads

$$T_{\mathrm{far}} = F_0(\mathrm{Pe}) \exp\left(\frac{1}{2}\xi\cos\theta\right) \mathrm{K}_0\left(\sqrt{\frac{1}{4} + \frac{\tilde{b}}{\mathrm{Pe}^2}}\xi\right), \tag{6.25}$$

where the infinity-unbounded I_0 function is discarded again as temperature must decay to zero far away from the flame. Whenever heat losses are non-negligible as in the configuration at hand, the K_0 function is dominated by the term within the square root, $\tilde{b}/\mathrm{Pe}^2$, for $\mathrm{Pe} \ll 1$. This far-field profile evolves towards the flame region as $\xi \ll 1$, with the limiting behavior of the K_0 function when its argument goes to $(\sqrt{\tilde{b}}r)$, and the exponential function approximates to

$$\exp\left(\frac{1}{2}\xi\cos\theta\right) \simeq 1 + \frac{1}{2}\xi\cos\theta + \frac{1}{8}\xi^2\cos^2\theta + \mathcal{O}(\xi^3)$$

First-order matching with the near-field solution implies that $F_0 = [\mathrm{K}_0(\sqrt{\tilde{b}}r)]^{-1}$. This solution practically agrees with the complete solution of eq. (6.13),

$$T_{\mathrm{com}} = \exp\left(\frac{1}{2}(r-1)\mathrm{Pe}\cos\theta\right) \frac{\mathrm{K}_0\left(\sqrt{\frac{1}{4} + \frac{\tilde{b}}{\mathrm{Pe}^2}}\mathrm{Pe}\, r\right)}{\mathrm{K}_0\left(\sqrt{\frac{1}{4} + \frac{\tilde{b}}{\mathrm{Pe}^2}}\mathrm{Pe}\right)}. \tag{6.26}$$

However, an arbitrarily large value of the heat-loss parameter $\tilde{b}$ can produce a fast enough temperature decay to render the convective corrections at the far field unnecessary. Use made of Taylor series, the characteristic length associated with complete temperature decay due to heat losses can be estimated as $r_b \sim \mathcal{O}(\tilde{b}^{-1/2})$. Furthermore, convective corrections from the exponential term enter at distances $r_c \sim \mathcal{O}(\mathrm{Pe}^{-1})$ where the thermal wake arises. If $\tilde{b} \gg \mathrm{Pe}^2$, as expected in the low-Péclet limit and proven below, then $r_b < r_c$ and convective effects are unnoticeable at a cold homogeneous far field.

Figure 6.2 shows the comparison of complete (solid), near-field (dotted), far-field (dot-dashed) and numerical (symbols) temperature distributions for a fixed Pe and several values of $\tilde{b}$.

Very small values of the latter, of the order of Pe^2 confirm an important disagreement of the axisymmetric near-field description with the complete solution. However, heat losses as small as $\tilde{b} \sim \mathcal{O}(\mathrm{Pe})$ already provide a great agreement and independence of the angular coordinate near the flame surface.

The distributions of species and temperature fields so far are uncoupled between them and prescribed by scalar transport only. However, these distributions must be compatible with the reactant consumption and heat generation, which are linked through the chemical reaction of the mixture addressed in the following section.

6.3 Flame jump condition

The reaction-sheet approximation is characterized by the large value of the dimensionless activation energy, $\beta \gg 1$. In that infinitely thin region, a jump condition must be imposed between the burnt ($r < 1$) and unburnt ($r > 1$) zones. The specific relation is obtained from the first integration between $r = 1^+$ and $r = 1^-$ of the reaction-diffusion layer upon combination of species and energy equation to rule out the reaction rate. The local heat flux and production at the flame is then related to the diffusive feed of reacting species,

$$\left.\frac{\partial T}{\partial r}\right|_{r=1^-} - \left.\frac{\partial T}{\partial r}\right|_{r=1^+} = \frac{\tilde{q}}{\mathrm{Le}} \left.\frac{\partial Y}{\partial r}\right|_{r=1^+}. \tag{6.27}$$

Taking the analytic expressions of Y and T obtained above at the near-field region, which apply in the proximity of the flame, we can rewrite

$$\frac{\mathrm{I}_1\left(\sqrt{\tilde{b}}\right)\sqrt{\tilde{b}}}{\mathrm{I}_0\left(\sqrt{\tilde{b}}\right)} + \frac{\mathrm{K}_1\left(\sqrt{\tilde{b}}\right)\sqrt{\tilde{b}}}{\mathrm{K}_0\left(\sqrt{\tilde{b}}\right)} + \frac{\tilde{q}}{\mathrm{Le}}\left[\frac{1}{\ln\left(\mathrm{PeLe}\right) + \ln\left(\frac{1}{4}\right) + \gamma}\right] = 0. \tag{6.28}$$

The jump condition results in a relation for $\tilde{b}$ and Pe that involves $\tilde{q}$ and Le. Characteristic longitudinal profiles of temperature and species that satisfy the flame-sheet jump condition at $r = 1$ can be found in Fig. 6.3 (left) for $\mathrm{Pe} = 0.02$. In particular, the value of the heat-loss parameter recovered is $\tilde{b} = 0.04$, with $\mathrm{Le} = 0.3$ and $\tilde{q} = 1$. The contour lines in Fig. 6.3 (right) indicate that the temperature field (red contours) is practically unaffected by convection due to the fast decay produced via off-plane heat losses and producing nearly circular isocontours, while the mass fraction distribution (dashed contours) develops a noticeable elongation as a wake of lower concentration of reactants owing to the far-field convective effects.

The relation between a range of $\tilde{b}$ and a collection of Pe, describe the possible combinations of heat losses and convective-to-diffusive relevance for the steady circular flame configuration. In addition, an order-of-magnitude analysis for $\tilde{b}$ can be extracted from eq. (6.28). First, the ascending series for small arguments of the first two terms therein are used to write,

$$\frac{I_1(\eta)\cdot\eta}{I_0(\eta)} \simeq \frac{\eta^2}{2} - \frac{\eta^4}{16} + \frac{\eta^6}{96} + o\left(\eta^8\right)$$
$$\frac{K_1(\eta)\cdot\eta}{K_0(\eta)} \simeq -\frac{1}{\ln(\eta) + \gamma - \ln(2)} + o\left(\eta^2\right)$$

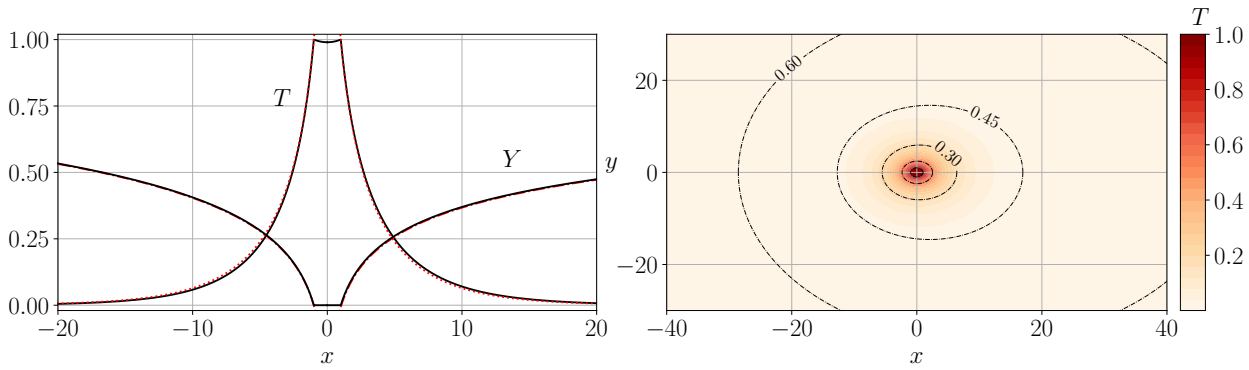

Figure 6.3: Temperature and species concentration theoretical distributions for Pe = 0.02 and $\tilde{b} = 0.04$ (fulfilling the jump condition). On the left the longitudinal cuts at y=0; on the right, a top view of the variable profiles, temperature contour field (red colormap) and species contour levels (dashed lines).

so that the three terms involved in the jump condition are respectively of the order

$$\sim \tilde{b}, \sim \frac{1}{\ln\left(\sqrt{\tilde{b}}\right) + \gamma - \ln(2)}, \sim \frac{\tilde{q}/\mathrm{Le}}{\ln(\mathrm{PeLe}) + \ln\left(\frac{1}{4}\right) + \gamma}$$

Finally, it should be noted that, in the low-Péclet limit, the obtained relative heat losses $\tilde{b}$ are also smaller than unity, and since $\tilde{b}\ln(\sqrt{\tilde{b}}) \ll 1$, the first term relative to burnt gases temperature derivative can be neglected. This means that for a small heat-loss parameter the burnt region would display a nearly constant temperature distribution in a first approximation. Equating the last two terms of the jump condition

$$\frac{\tilde{b}}{4} \simeq \left(\frac{\mathrm{PeLe}}{4}\right)^{\frac{2\mathrm{Le}}{\tilde{q}}} . \tag{6.29}$$

Figure 6.4 shows the pairs $[\mathrm{Pe}, \tilde{b}]$ with different order-unity values of $\tilde{q} = [0.8, 1, 1.2]$ and Le = 0.3 as obtained from the analytical expressions derived above (solid line), numerical computations (symbols) and scaling (dot-dashed). Here, the reader should recollect that $\tilde{b} \propto r_k'^2$ and $\mathrm{Pe} \propto r_k' S_u'/D_T'$. Furthermore, this scaling shows that a small value of $\tilde{b} \sim \mathcal{O}(\mathrm{Pe}^{0.6})$ is expected, but still larger than $\sim \mathcal{O}(\mathrm{Pe})$ in the low-Péclet limit. Therefore, heat-losses play a significant role in the near-field region and promote a fast decay of temperature, rendering far-field azimuthal corrections unnecessary as stated in the previous section.

This first condition at the flame imposes a relation between the three controlling parameters of the physical problem $[\mathrm{Pe}, \tilde{b}, \tilde{q}]$, given that the value of the Lewis number of the mixture is considered fixed. In fact, it relates the unknowns of size, velocity and flame temperature involved in the definition of these parameters. However, the specific solution of the inner reaction layer in the limit of large but bounded $\beta \gg 1$ can be obtained from the rigorous analytic integration of the reactive problem (Kurdyumov, 2019). This additional information sets the actual flame temperature T_f', which must remain near the adiabatic value, $T_f \simeq 1$ (with $\epsilon \ll 1$ as stated above) and, therefore, the dimensionless parameter $\tilde{q}$ is obtained.

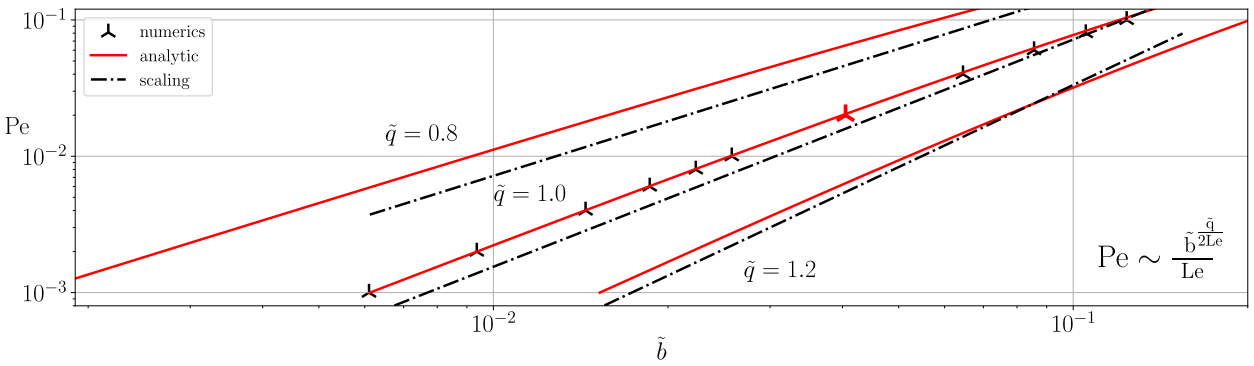

Figure 6.4: Péclet and heat-loss relation as provided from the closure of the jump condition at the flame. Numerical results (symbols) together with analytical solutions (red solid) and order-of-magnitude scaling (dot-dashed) are compared. The pair $\mathrm{Pe} = 0.02$ and $\tilde{b} = 0.04$ for $\tilde{q} = 1$ is shown in fig. 6.3 is marked with a red symbol.

Finally, there is a direct relation between the size and speed through the combination Pe and $\tilde{b}$, as depicted in fig. 6.4. A good agreement is found between the scaling, analytic relation and simplified numerical computation of the set of asymptotic equations.

It should be noted that, in the first instance, all the pairs found along the resulting line are viable solutions of the circular type. There is no reason to favor one combination over the others as a possible steady-state configuration. Therefore, a stability analysis is desirable to further investigate this result, which provisionally suggests that the ignition history may play a key role in determining the size and propagation speed.

6.4 Asymptotic analysis remarks

The flow structure of the steady isolated circular flame can be analyzed from the expansions developed through this chapter. The analytical descriptions for the species and temperature fields have been obtained in two-dimensional polar coordinates (r, θ) for nearly axisymmetric flames in the low-Péclet limit. Figure 6.5 displays a sketch of the quasi-planar structure of the circular isolated configuration (left) and the adiabatic planar counterpart (right).

First, both fluid variables are controlled by diffusion effects in the near field, and a mathematical description as a function of the radial coordinate is obtained when imposing a circular reaction front at $r = 1$. Moreover, the presence of heat losses and their effect over the energy conservation equation is paramount in determining the temperature field distribution. The conductive heat-loss effect forces a sharply decaying profile in the radial direction, which is well captured by the axisymmetric function of eq. (6.10). The characteristic distance of temperature decay $r_b \sim \mathcal{O}\left(\tilde{b}^{-1/2}\right)$, is smaller than the expected thermal diffusion distance of the planar flame $\delta_T \sim (\mathrm{Pe}^{-1})$, ruling out far-field effects on the temperature distribution.

Moreover, the larger species characteristic length, in which mass diffusivity acts, brings convection into play. The far field of hydrogen species is dominated by convective effects at distances of the order of $(\mathrm{PeLe})^{-1} \gg 1$. This information is used for asymptotic matching of

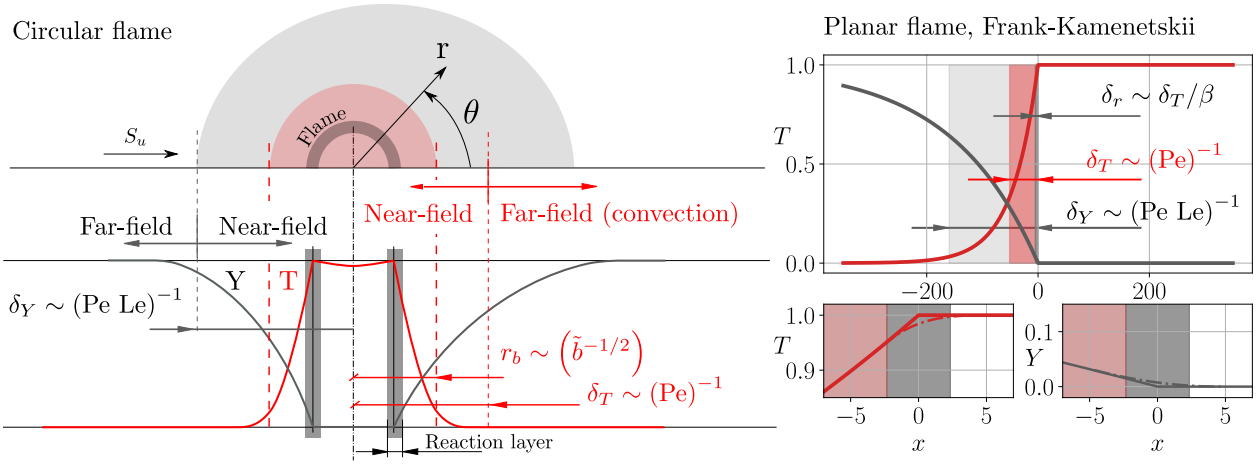

Figure 6.5: Circular flame structure sketch (left), top view and longitudinal cut along the symmetry axis. Flame-sheet model for adiabatic planar flame (right), general view of the temperature and species distribution and inner inner reaction layer zoom-in (bottom).

the near-field species logarithmic profiles with the homogeneous infinite field. Therefore, the resulting species distribution in eq. (6.21) is not exactly axisymmetric, developing a subtle wake of products.

Finally, the large activation energy limit renders an inner diffusion-reaction layer whose characteristic thickness is of the order of $\beta^{-1} \ll 1$. An analytic expression for the jump condition at the infinitely thin flame can be derived, use made of the simplified near-field profiles. This expression provides the relation between T and Y that must hold for physical consistency of the burning structure. Finally, the study of the reaction region can be extended to provide not only the scaling but a closure to the problem with the actual flame temperature, as a function of the chemical kinetics modeling.

The main highlight of this structure analysis is the combined effect of mass diffusivity and heat losses. The characteristic structure of the adiabatic planar flame on fig. 6.5 (right), following the Frank-Kamenetskii asymptotic model, is strongly modified by the cool-down effect of heat losses through the walls. Therefore, the thermal distance is reduced with respect to the planar counterpart, and the chemical reaction is only sustained thanks to preferential diffusion effects over curved fronts, with mass diffusivity acting intensively at much larger distances than the characteristic cooling length.

In conclusion, the theoretical expansions derived here are accurate enough for a preliminary description of a circular quasi-two-dimensional lean premixed hydrogen flame, that propagates in a low Péclet regime between two parallel plates in presence of transversal conductive heat losses. Therefore, provided the thermophysical properties of the problem and the chemical kinetics model, the relation between the propagation velocity and size of the circular kernel can be calculated.

The asymptotic description for the circular flame, presented in this section, was developed in collaboration with Prof. Antonio Sánchez after a three-month stay in the summer of 2022 at the University of California, San Diego (UCSD).

Chapter 7

Composition-space modeling

Numerous scientific studies aim to reduce the computational requirements of complex physical flows, which may involve prohibitively expensive simulations requiring hundreds of thousands of computational hours (T. Lu and Law, 2009), even when employing simplified chemical kinetics. Flamelet reduced techniques have been proven useful in modeling the reaction process when incorporating flow stretch and turbulent effects (Van Oijen et al., 2016). These techniques tabulate the main outcome of fluid variables as a function of specific progress variables typically related to the composition or mixture fraction of the gas. In turn, an exact derivation of the equations when transformed from the physical space to the composition space was recently provided by Scholtissek et al., 2020.

This chapter is devoted to the investigation of such techniques in the composition space to offer a deeper understanding of the balance between differential diffusion, curvature and heat losses, and derive further reduced models in the context of lean hydrogen-air deflagrations. This is achieved via a transformation of the independent variables into composition space. By comparing the balance of terms in reduced models, both for planar flames and for a generic kernel from previous quasi-2D simulations, it is observed that a reaction-diffusion state is recovered to the leading order. Meanwhile, 'extra' conductive heat losses are primarily balanced by the preferential diffusion term associated with curvature to the following order. The limitations of the classical flamelet manifolds are pointed out and a basic model is derived to capture the coupling between the effects of curvature and heat losses, aiming to explain the arising of weak reaction kernels.

Specifically, the composition frame is first presented, identifying various terms related to the physical processes involved and their directionality. In fact, the equations involve the reaction rate and transport terms linked to convection and diffusion in local-flame normal and tangential directions. After that, a non-adiabatic planar (one-dimensional) flame model is described as a first benchmark. Later, the methodology is applied to the quasi-2D confined lean premixed flames studied in this thesis. All together, a practical piece of information is obtained for the understanding of the controlling mechanisms and for future derivation of extended turbulent combustion models.

7.1 Composition-space equations

The set of conservation equations in physical space can be projected into the composition space, based on the species mass fraction scalar Y. This description is here followed for the temperature distribution and the modulus of the gradient of species $g_Y = |\nabla Y|$. The different terms from the energy and species conservation equations will be projected to a new local coordinate system $\{\mathbf{n},\ \boldsymbol{\tau}\}$, in which the normal vector follows the species gradient and the tangential unity vector forms a right dihedral

$$\mathbf{n} = \frac{-\nabla Y}{|\nabla Y|}, \qquad \boldsymbol{\tau} = [-n_y,\ n_x]\,. \tag{7.1}$$

Through this particular definition, the independent variables are transformed from the spatial coordinates, $\{T,\ Y\}(x, y; t)$, to the local curvilinear coordinates prescribed through the composition of the mixture $\{T,\ g_Y\}(\mathbf{n}(x, y; t), \boldsymbol{\tau}(x, y; t); t)$. This definition enables the expression of first derivatives,

$$\nabla T = (\nabla T \cdot \mathbf{n})\,\mathbf{n} + (\nabla T \cdot \boldsymbol{\tau})\,\boldsymbol{\tau} = \underbrace{\frac{\partial T}{\partial Y}\nabla Y}_{\text{normal}} + \underbrace{\frac{\partial T}{\partial \tau}\boldsymbol{\tau}}_{\text{tangential}}\,, \tag{7.2}$$

$$\nabla Y = (\nabla Y \cdot \mathbf{n})\,\mathbf{n} + (\nabla Y \cdot \boldsymbol{\tau})\,\boldsymbol{\tau} = \underbrace{\nabla_n Y \mathbf{n}}_{\text{normal}}, \tag{7.3}$$

and the second derivatives,

$$\nabla^2 T = \nabla \cdot (\nabla T) = \frac{\partial^2 T}{\partial n^2} + \frac{\partial T}{\partial n}\nabla \cdot \mathbf{n} + \frac{\partial^2 T}{\partial \tau^2} + \frac{\partial T}{\partial \tau}\nabla \cdot \boldsymbol{\tau} = \underbrace{\frac{\partial^2 T}{\partial Y^2}|\nabla Y|^2 + \frac{\partial T}{\partial Y}\nabla^2 Y}_{\text{normal}} + \underbrace{\frac{\partial^2 T}{\partial \tau^2} + \frac{\partial T}{\partial \tau}\nabla \cdot \boldsymbol{\tau}}_{\text{tangential}}, \tag{7.4}$$

$$\nabla^2 Y = \nabla \cdot (\nabla Y) = \nabla \cdot (-\mathbf{n} g_Y) = -g_Y \nabla \cdot \mathbf{n} - \mathbf{n}\nabla g_Y = -g_Y \nabla \cdot \mathbf{n} + \mathbf{n} \cdot [(\mathbf{n} \cdot \nabla)\nabla Y] \tag{7.5}$$

$$= \underbrace{-g_Y \kappa + g_Y \frac{\partial g_Y}{\partial Y}}_{\text{normal}}, \tag{7.6}$$

where $\kappa = \nabla \cdot \mathbf{n}$ is the local curvature of the coordinate system, and it can be observed that there is no tangential contribution to the species gradient and its second derivatives since the normal vector is defined from the species gradient itself.

7.1.1 Temperature equation

In order to rewrite the energy conservation equation in the new base, the material derivative of the temperature can be expressed as

$$\frac{DT}{Dt} = \frac{\partial T}{\partial t} + \mathbf{u} \cdot \nabla T = \frac{\partial T}{\partial t_Y} + \frac{\partial T}{\partial \tau}\frac{D\tau}{Dt} + \frac{\partial T}{\partial n}\frac{Dn}{Dt} = \frac{\partial T}{\partial t_Y} + \frac{\partial T}{\partial \tau}\frac{D\tau}{Dt} + \frac{\partial T}{\partial Y}\frac{DY}{Dt}, \tag{7.7}$$

where $\partial/\partial t_Y$ is the unsteady term as computed from the moving reference frame of the species field evolution. In turn, the species conservation equation can be used to substitute the species material derivative, DY/Dt, to yield

$$\frac{DT}{Dt} = \frac{\partial T}{\partial t_Y} + \frac{\partial T}{\partial \tau}\frac{D\tau}{Dt} + \frac{\partial T}{\partial Y}\left(\frac{\nabla^2 Y}{\rho \mathrm{Le}} - \frac{\Omega}{\rho}\right). \tag{7.8}$$

Therefore, the temperature evolution equation in the composition space can be rewritten in terms of the normal and tangential directions,

$$\begin{aligned}\frac{\partial T}{\partial t_Y} = &\frac{1}{\rho}\frac{\partial^2 T}{\partial Y^2} g_Y^2 + \frac{1}{\rho}\frac{\partial T}{\partial Y}\left(1 - \frac{1}{\mathrm{Le}}\right) g_Y \left(\frac{\partial g_Y}{\partial Y} - \kappa\right) \\ &- \frac{\partial T}{\partial \tau}\frac{D\tau}{Dt} + \frac{1}{\rho}\frac{\partial^2 T}{\partial \tau^2} - \frac{1}{\rho}\frac{\partial T}{\partial \tau}\nabla\cdot\tau + \frac{\Omega}{\rho}\left(1 + \frac{\partial T}{\partial Y}\right) - b\frac{T}{\rho}.\end{aligned} \tag{7.9}$$

7.1.2 Species gradient equation

The definition $g_Y = |\nabla Y| = -\mathbf{n}\cdot\nabla Y$ can be used to write the following identity for the time derivative of the gradient of species,

$$\begin{aligned}\frac{\partial g_Y}{\partial t} = \frac{\partial(-\mathbf{n}\cdot\nabla Y)}{\partial t} = \frac{\partial}{\partial t}\left(\frac{\nabla Y\cdot\nabla Y}{|\nabla Y|}\right) = \\ = -\frac{\nabla Y\cdot\nabla Y}{|\nabla Y|^2}\frac{\partial|\nabla Y|}{\partial t} + 2\frac{\nabla Y}{|\nabla Y|}\cdot\frac{\partial \nabla Y}{\partial t} = -\frac{\partial g_Y}{\partial t} - 2\mathbf{n}\cdot\frac{\partial \nabla Y}{\partial t}.\end{aligned} \tag{7.10}$$

Therefore, the material derivative $Dg_Y/Dt = \partial g_Y/\partial t + \mathbf{u}\cdot\nabla g_Y$ can be composed from the previous identity and the species conservation equation to substitute $\partial Y/\partial t$, use made of the additional identity $\nabla g_Y = \nabla|\nabla Y| = -(\mathbf{n}\cdot\nabla)\nabla Y$, to yield

$$\begin{aligned}\frac{Dg_Y}{Dt} = -\mathbf{n}\cdot\nabla\left(\frac{\partial Y}{\partial t}\right) + \mathbf{u}\cdot\nabla g_Y = -\mathbf{n}\cdot\nabla\left(-\mathbf{u}\cdot\nabla Y + \frac{\nabla^2 Y}{\rho\mathrm{Le}} - \frac{\Omega}{\rho}\right) + \mathbf{u}\cdot\nabla g_Y = \\ = -g_Y\mathbf{n}\cdot[(\mathbf{n}\cdot\nabla)\mathbf{u}] - \mathbf{n}\cdot\nabla\left(\frac{\nabla^2 Y}{\rho\mathrm{Le}} - \frac{\Omega}{\rho}\right) = -g_Y a_N + g_Y\frac{\partial}{\partial Y}\left[\frac{g_Y}{\rho\mathrm{Le}}\left(\frac{\partial g_Y}{\partial Y} - \kappa\right) - \frac{\Omega}{\rho}\right],\end{aligned} \tag{7.11}$$

being a_N the normal flow strain rate, part of the velocity gradient expressed in an orthogonal coordinate system attached to the species iso-contour,

$$\begin{aligned}a_N = \mathbf{n}\cdot[(\mathbf{n}\cdot\nabla)\mathbf{u}] = n_x\left(n_x\frac{\partial u_x}{\partial x} + n_y\frac{\partial u_x}{\partial y}\right) + n_y\left(n_x\frac{\partial u_y}{\partial x} + n_y\frac{\partial u_y}{\partial y}\right) \\ = n_x^2\frac{\partial u_x}{\partial x} + n_x n_y\frac{\partial u_x}{\partial y} + n_y n_x\frac{\partial u_y}{\partial x} + n_y^2\frac{\partial u_y}{\partial y}.\end{aligned} \tag{7.12}$$

The evolution equation for g_Y in composition space can be then derived from the definition of material derivative

$$\frac{\partial g_Y}{\partial t_Y} = \frac{Dg_Y}{Dt} - \frac{DY}{Dt}\frac{\partial g_Y}{\partial Y} = -g_Y a_N + g_Y\frac{\partial}{\partial Y}\left[\frac{g_Y}{\rho\mathrm{Le}}\left(\frac{\partial g_Y}{\partial Y} - \kappa\right) - \frac{\Omega}{\rho}\right] - \frac{DY}{Dt}\frac{\partial g_Y}{\partial Y}, \tag{7.13}$$

where the different terms can be grouped in various effects, after substitution of DY/Dt with the right hand side of the species conservation equation,

$$\begin{aligned}
\text{reaction rate}: \quad & -g_Y \frac{\partial}{\partial Y}\left(\frac{\Omega}{\rho}\right) + \frac{\partial g_Y}{\partial Y}\frac{\Omega}{\rho} = -g_Y^2 \frac{\partial}{\partial Y}\left(\frac{\Omega}{\rho g_Y}\right) \\
\text{curvature}: \quad & -g_Y \frac{\partial}{\partial Y}\left(\frac{g_Y}{\rho \mathrm{Le}}\kappa\right) + \frac{g_Y}{\rho \mathrm{Le}}\kappa\frac{\partial g_Y}{\partial Y} = -g_Y^2 \frac{\partial}{\partial Y}\left(\frac{\kappa}{\rho \mathrm{Le}}\right) \\
\text{remaining diffusion}: \quad & g_Y \frac{\partial}{\partial Y}\left(\frac{g_Y}{\rho \mathrm{Le}}\frac{\partial g_Y}{\partial Y}\right) - \frac{1}{\rho \mathrm{Le}} g_Y \frac{\partial g_Y}{\partial Y}\frac{\partial g_Y}{\partial Y} = g_Y^2 \frac{\partial}{\partial Y}\left(\frac{1}{\rho \mathrm{Le}}\frac{\partial g_Y}{\partial Y}\right)
\end{aligned}$$

to yield the final equation for the gradient of species,

$$\boxed{\frac{\partial g_Y}{\partial t_Y} = -g_Y a_N + g_Y^2 \frac{\partial}{\partial Y}\left(\frac{1}{\rho \mathrm{Le}}\frac{\partial g_Y}{\partial Y}\right) - g_Y^2 \frac{\partial}{\partial Y}\left(\frac{\kappa}{\rho \mathrm{Le}}\right) - g_Y^2 \frac{\partial}{\partial Y}\left(\frac{\Omega}{\rho g_Y}\right).} \tag{7.14}$$

7.2 Non-adiabatic planar flame model

First, a one-dimensional flame model is created as a base tool for the test of the aforementioned contributions. In particular, the planar flame conservation equations can be readily extended with an analogous heat-loss linear sink term through parameter b, use made of the same non-dimensional variables of the 2D case presented in chapter 3,

$$m\frac{\partial T}{\partial x} = \frac{\partial^2 T}{\partial x^2} + \Omega - bT, \qquad m\frac{\partial Y}{\partial x} = \frac{1}{\mathrm{Le}}\frac{\partial^2 Y}{\partial x^2} - \Omega, \tag{7.15}$$

where $m = \rho u_x$ is the mass flow rate. The same chemical reaction rate is used, which is recalled here for convenience,

$$\Omega = \rho^2 \beta^2 (1+q)^2 \frac{Y}{2 s_L^2 \mathrm{Le}} \exp\left(\frac{\beta(T-1)}{1 + \frac{q}{1+q}(T-1)}\right). \tag{7.16}$$

The typical procedure to solve the system of eqs. (7.15) is to prescribe a fixed temperature value at a specific position of the $x-$coordinate domain and solve for the eigenvalue m. It should be noted that the value $s_L^2 = 1.05$ appearing in the reaction rate expression provides unity dimensionless mass flow rate ($m = 1$) for the adiabatic planar flame with $b = 0$.

The solution of the planar flame problem is depicted in the left panel of fig. 7.1 for $\mathrm{Le} = 1$, including the temperature, species and reaction rate distributions over the spatial coordinate. Increasing values of the parameter $b \in [0,\ 0.005,\ 0.01,\ 0.015,\ 0.018]$ produce lower temperatures and reaction rates (increasing transparency of curves). Additionally, the right panel of fig. 7.1 displays the planar-flame information for variables T, $g_Y = |dY/dx|$ and $g_T = |dT/dx|$ on the composition space, namely over the independent variable Y. This is the characteristic representation provided in the context of turbulent combustion modeling through flamelet manifolds. First, it can be noted that the dependence between T and Y remains practically linear for increasing values of b, where a small discrepancy is found between the temperature and species gradient given that heat losses act only on the energy equation.

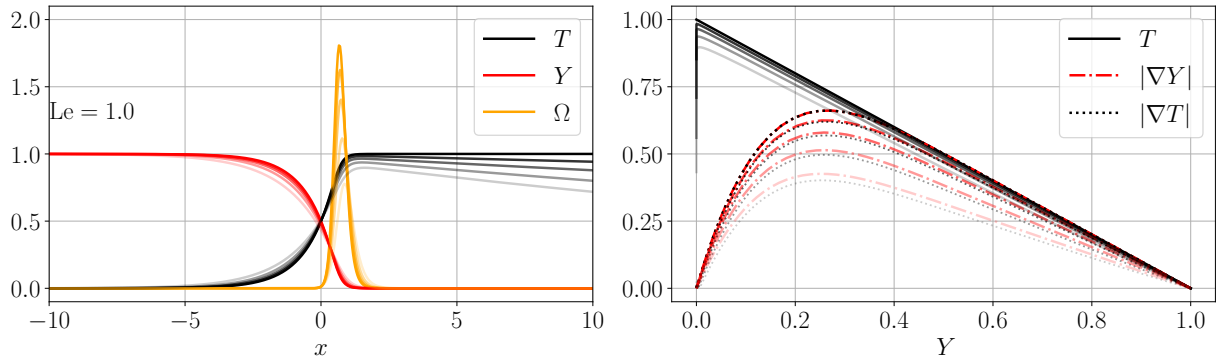

Figure 7.1: Non-adiabatic planar flame with Le = 1. Temperature, species and reaction rate (left). Conditional averages on the composition space of temperature, temperature gradient and species gradient. Heat losses variation $b \in [0,\ 0.005,\ 0.01,\ 0.015,\ 0.018]$ (increasing transparency).

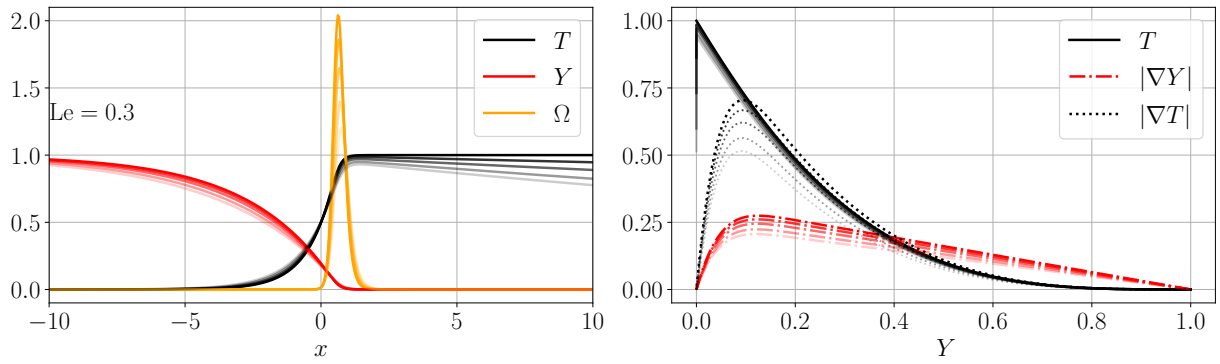

Figure 7.2: Le = 0.3 case. See caption in fig. 7.1.

Some modifications must be take into account when incorporating highly diffusive fuel properties. The left panel of fig. 7.2 displays the analogous spatial distributions of temperature and species for the planar flame with Le = 0.3. In this case, the differential diffusion effect, owing to the non-unity Le number, makes a difference in the species distribution at the preheated region, and the production term Ω is slightly reinforced keeping the temperature close to the adiabatic value. However, increasing values of b also produce the obvious temperature decay. This differential diffusion effect is more noticeable in the composition space shown in the right panel of fig. 7.2, where the solid black line $T(Y)$ does not keep the equi-diffusional linear trend, and the temperature and species gradients show obvious differences in their distribution.

The variation of heat loss values, shown in the graphs with increasing transparency, is gathered in table 7.1 including the corresponding mass flow rate eigenvalues. These reactant consumptions of the premixed flames decay consistently with increasing b, as flames subject to greater heat losses must propagate with weaker intensities. In addition, the m parameter in the table shows that the flame propagation velocity for the Le = 0.3 case is larger as it should be expected for a more diffusive deficient fuel. The reinforcement of the combustion process due to the differential diffusion in the planar flame, in absence of curvature effects, has

	b	0	0.005	0.010	0.015	0.018
Le = 1.0	m	1.004	0.946	0.873	0.769	0.630
Le = 0.3	m	1.077	1.022	0.957	0.873	0.802

Table 7.1: 1D mass flow rate eigenvalues for different heat loss parameters.

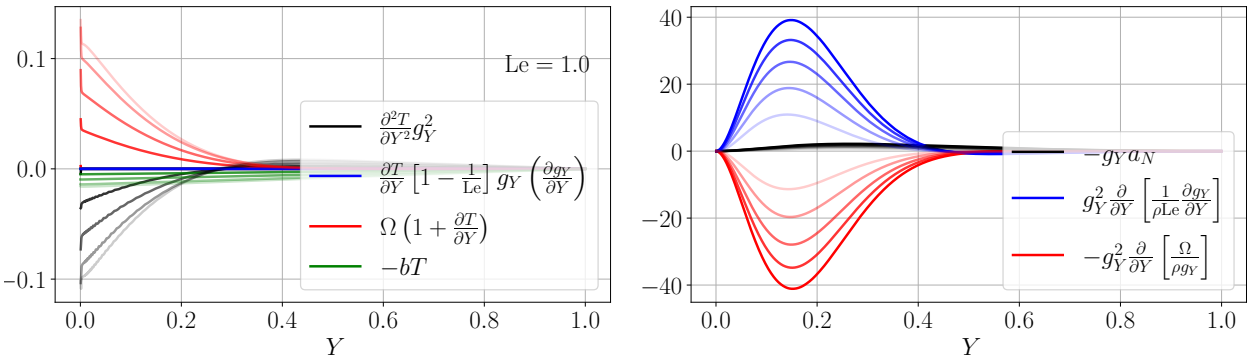

Figure 7.3: Evaluation of terms in composition space of temperature eq. (7.17) (left) and species gradient eq. (7.18) (right) for a planar flame with Le = 1. Heat losses variation $b \in [0,\ 0.005,\ 0.01,\ 0.015,\ 0.018]$ (increasing transparency).

an alternative direct consequence, the maximum value of heat losses sustained by the flame under non-unity Lewis numbers is slightly higher than in the equi-diffusional case. However, a first comparison shows that the maximum heat-loss parameter b sustained by the planar flame is two orders of magnitude smaller than those found in the two-dimensional cases presented in chapter 4, highlighting the expected key role of curvature in preserving these structures. Additional information about the one-dimensional model computation can be consulted in appendix E.

The evaluation of the role of different physical terms is studied in the composition-space eqs. (7.9) and (7.14) in absence of tangential and curvature effects ($\kappa = 0$). The steady-state character of the 1D problem in the flame reference frame allows to further remove the temporal evolution term $\partial(\,)/\partial t_y$. In fact, the normal projection of the temperature and species gradient reads,

$$0 = \frac{\partial^2 T}{\partial Y^2} g_Y^2 + \frac{\partial T}{\partial Y}\left(1 - \frac{1}{\mathrm{Le}}\right) g_Y \frac{\partial g_Y}{\partial Y} + \Omega\left(1 + \frac{\partial T}{\partial Y}\right) - bT, \tag{7.17}$$

$$0 = -g_Y a_N + g_Y^2 \frac{\partial}{\partial Y}\left(\frac{1}{\rho \mathrm{Le}} \frac{\partial g_Y}{\partial Y}\right) - g_Y^2 \frac{\partial}{\partial Y}\left(\frac{\Omega}{\rho g_Y}\right). \tag{7.18}$$

Initially, the Le = 1 flame is depicted in fig. 7.3 , where the overall balance in temperature eq. is provided through the reaction and first diffusion term, as the $(1 - \mathrm{Le}^{-1})$ factor is ruled out in equi-diffusional fuels, with negligible action of the heat-loss mechanism (left panel) and null reaction term in the absence of heat losses when $\partial T/\partial Y = -1$. Moreover, the species gradient budget (right panel) is also ensured through the reaction-diffusion competition. For the Le = 0.3 case, the terms are shown in fig. 7.4, with additional contribution to the reaction-diffusion structure through differential diffusion (blue), which shifts the reaction (red) to lower fuel species concentration values (left panel). Finally, it can be observed that the

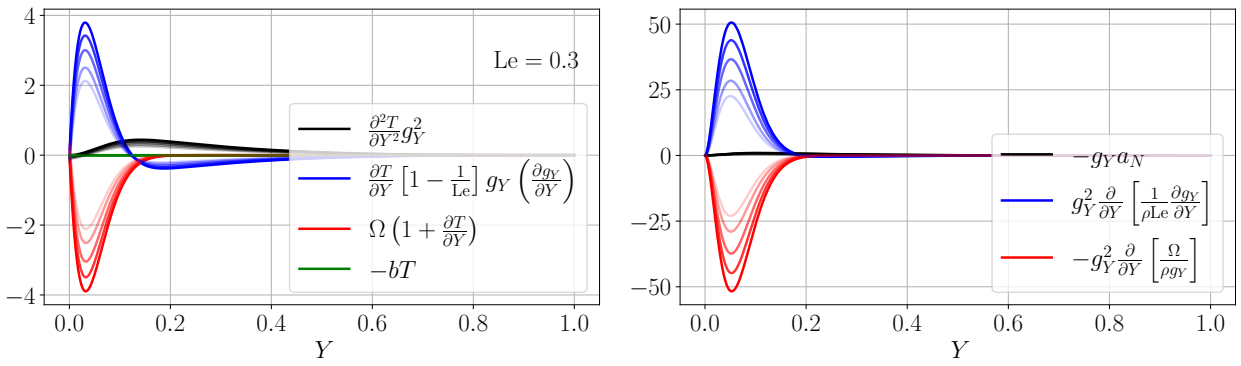

Figure 7.4: Le = 0.3 case. See caption in fig. 7.3.

balance of species gradient is only subtly altered through the strain process (right panel). It should be noted again that neither of the cases can sustain order-unity heat-loss parameters as observed in the quasi-2D computations, with $b \simeq 0.02$ already inducing extinction of the planar flame.

However, the main goal is to verify that larger heat losses can be sustained due to flame curvature effects in the 2D case, enhancing preferential diffusion. As a preamble, we shall evaluate the additional curvature effect of eqs. (7.9) and (7.14) on top of the resulting profiles of the planar non-adiabatic flame, mainly balanced through reaction and diffusion. Simultaneously, the evaluation of a higher b term is considered to achieve the zero budget of curvature and conductive heat losses. Figure 7.5 depicts the heat loss and curvature terms in composite space considering the base distribution of variables, $T(Y)$ and $g_Y(Y)$ from the planar flame solution of fig. 7.4, when incorporating $b = 1$ and different variations of $\kappa(Y)$. To do so, a given input can be provided for curvature when approximated by the inverse of the radius in the nearly axysimmetric diffusion-dominated species field, related to the scaling information obtained in chapter 6, where $Y \sim C\ln(r)$. Therefore, $\kappa \simeq -1/r \sim -\kappa_0/\exp(Y)$, with different values tested in the set $\kappa_0 = [-0.2,\ -0.4,\ -0.5,\ -0.6,\ -0.8]$. The left panel of fig. 7.5 displays the curvature effect term on the temperature equation as a function of the composition space (blue dotted), together with the extra heat losses term (green). The global balance of both effects (black) is offered for discussion on budget closure. The extra heat loss term for the temperature equation seems to be balanced for most of the composition space with an appropriate curvature contribution, except in the near-flame region ($Y \simeq 0$). Therefore, some additional arrangements may be required to correctly close the budget in 2D realistic configurations, namely tangential effects. The right panel, shows the additional curvature term in the species gradient equation of order $\sim \mathcal{O}(1)$, which is much smaller than the dominant reaction-diffusion effects identified in fig. 7.4 (right). For this reason, we will mainly focus on the extensions to the energy equation in the following discussion.

After these preliminary calculations, it is observed that the curvature would be able to balance the second-order effects of high heat losses for a large part of the species range. However, an additional adjustment is needed for the area where the species tend to zero. In next section, these main ideas extracted from the one-dimensional model are actually evaluated on a two-dimensional simulation.

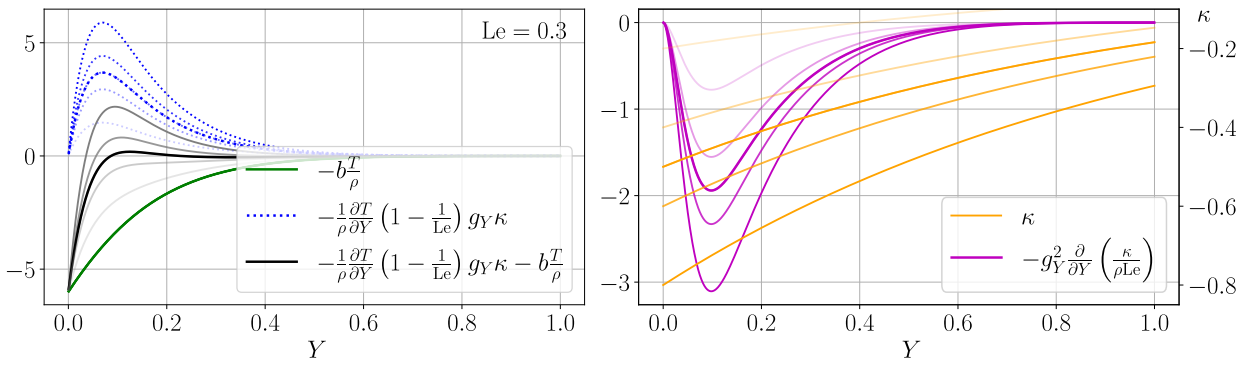

Figure 7.5: Le = 0.3, energy composition equation on the left, species gradient norm composition equation on the right. Extra heat losses term in green $b = 1$, curvature term in blue for six κ values, $\kappa_0 = [-0.2,\ -0.4,\ -0.5,\ -0.6,\ -0.8]$, $\kappa = \kappa_0/\exp(Y)$; sum in black. Highlight in solid $\kappa_0 = -0.5$, balancing the losses term for part of the domain. On the right orange axis the curvature distributions.

7.3 Two-dimensional data

The different terms in the composition-space temperature eq. (7.9) are here analyzed using data from a transient simulation. Particularly, the fixed velocity field perturbation of case B, as detailed in chapter 5, is used with $b = 1$ and $q = 5$. Figure 7.6 (left) presents a visualization of the species mass fraction field at a late time step, $t = 4$, during the unsteady propagation of the dividing reactive front. The red cross identifies the detailed isolated flame kernel shown in the central and right panels. The central panel shows the misalignment between the iso-contours of temperature (orange) and species (white), pointing out the region of the domain susceptible to suffering from major tangential effects. The right panel displays the local coordinate system, normal (white arrows) and tangential directions (red arrows), used to project the composition space equations. In addition, the last panel shows the direction of the temperature gradient (gray arrows) to highlight the difference of alignment in scalars. It should be noted that the normal $\mathbf{n}$ is not defined when the scalar field is constant, as in the unburnt region $Y = 1$ or inner burnt area $Y = 0$ of the circular kernel.

Next, the different terms derived from the temperature eq. (7.9) in composition space are evaluated for the example case in fig. 7.7, where their spatial distributions are presented at the zoom-in region. As a general trend, a balance between diffusion and reaction is observed. These two terms are of the order of $\sim \mathcal{O}(10^2)$, two orders higher than the rest. Moreover, some terms appear to be localized to certain specific areas of the flow. In particular, the tangential terms are present in the rear part of the configuration, even though they are small, they act in the area of misalignment of temperature and species isocontours, which is caused by the diffusion refill of species behind the isolated kernel and the conductive heat losses.

In order to close the budget of the energy equation and analyze the balance of the different terms involved, we shall present the information computed and displayed over the 2D data through a scatter of values and conditional averages in the composition space, see fig. 7.8. Each physical process is happening in different parts of the domain with varying intensities. However, same values of Y can be found at the rear and front regions, owing to the reactant

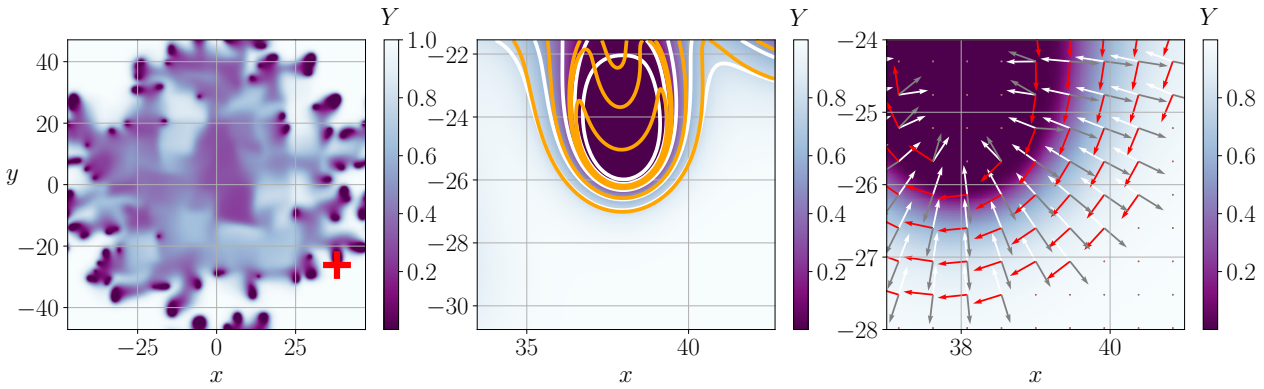

Figure 7.6: Species mass fraction with velocity fluctuations for case B. Complete domain at $t = 4$ (left) and selected kernel under study (cross). Zoom-in of the corresponding field with iso-contours (center) for temperature $T = [0.02,\ 0.2,\ 0.8,\ 0.9,\ 1.1]$ (orange), and species $Y = [0.005,\ 0.05,\ 0.3,\ 0.6,\ 0.8]$ (white). Local vector fields (right) of normal $\mathbf{n}$ (white), tangent $\boldsymbol{\tau}$ (red) and local unitary vector following ∇T (gray).

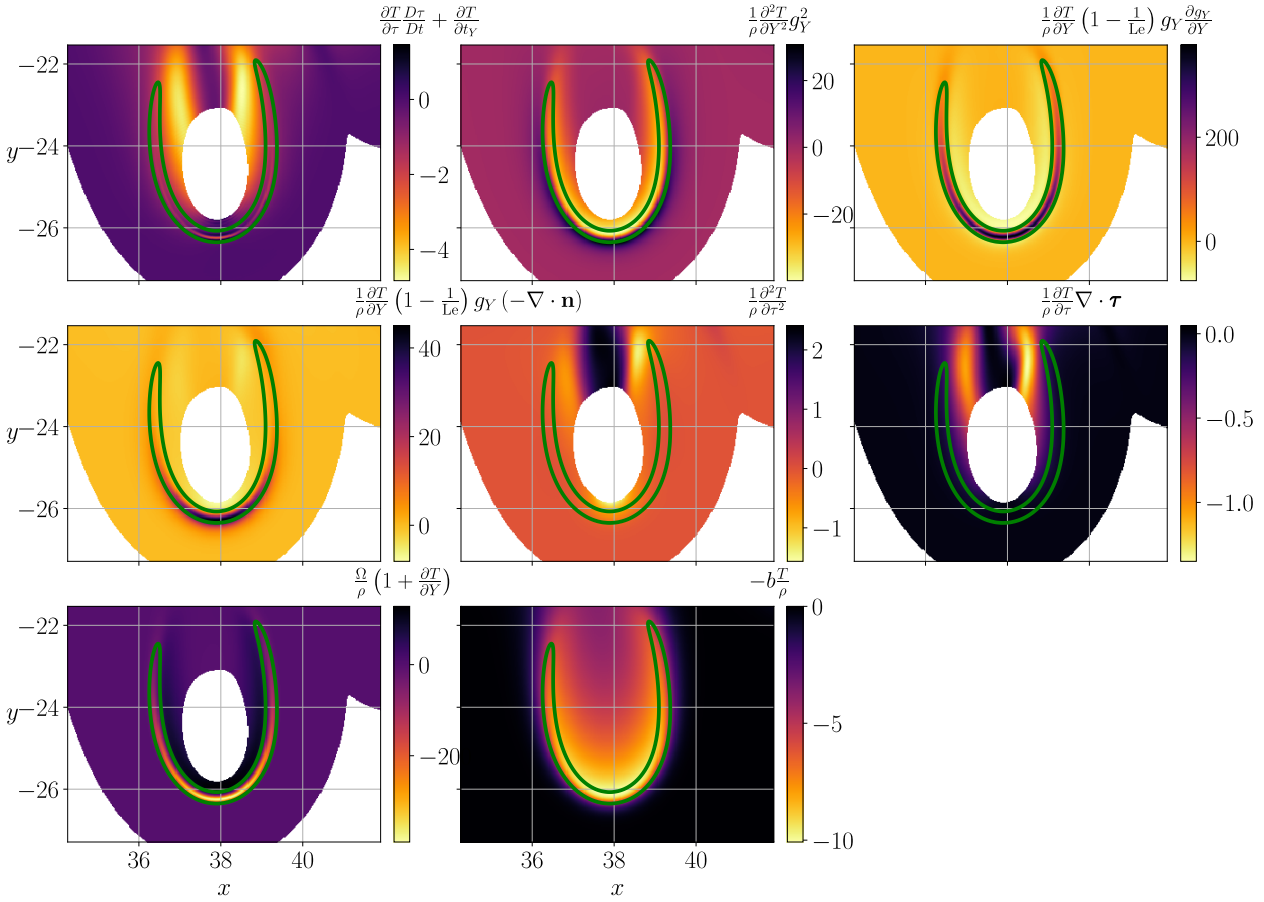

Figure 7.7: Equation (7.9) terms evaluated in physical space for the 2D case at $t = 2.5$. Green contour $\Omega/\rho = 5$ for visual reference of the flame front at the zoom-in region.

refill over burnt wakes of isolated kernels. Therefore, there is a noticeable dispersion in the scatter graphs in fig. 7.8, showing that variability of regimes for the same values of Y.

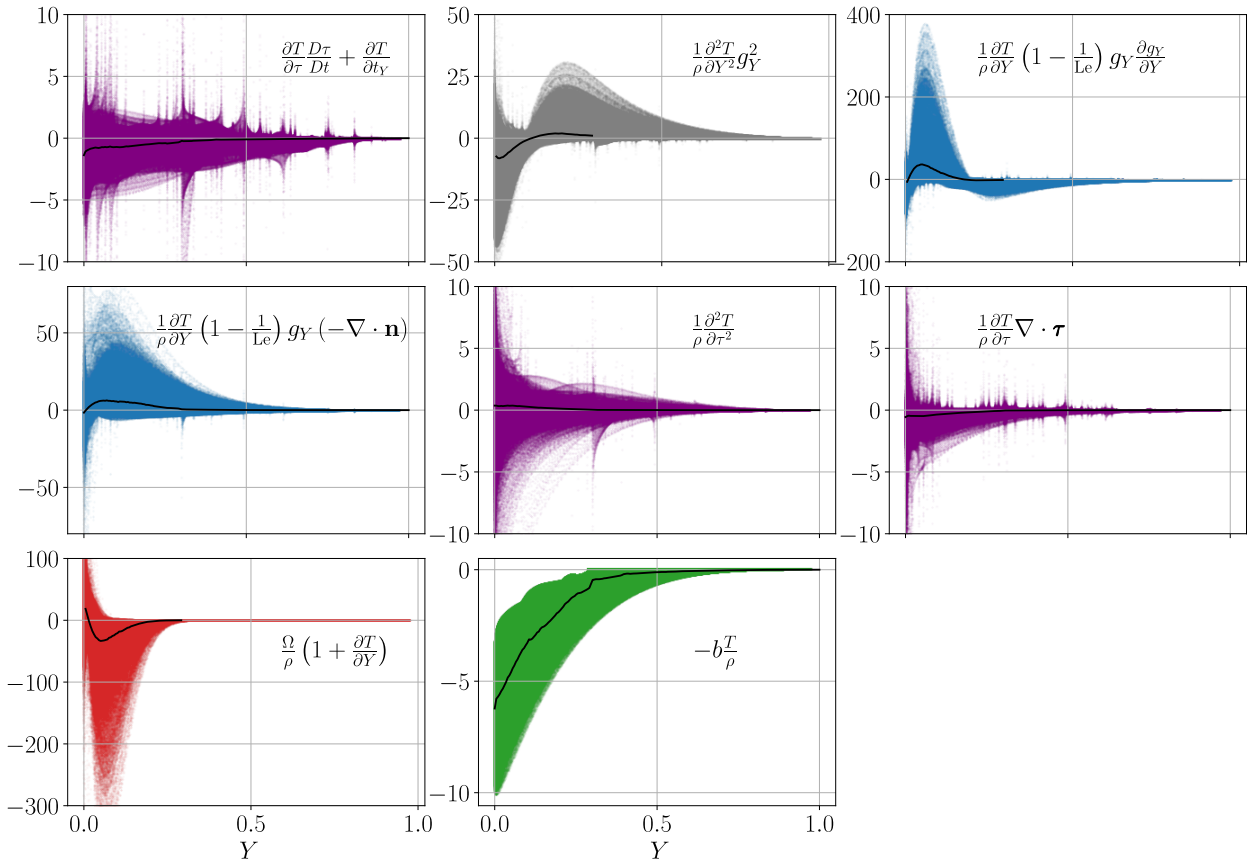

Figure 7.8: Evaluation of eq. (7.9) terms in composition space from the 2D simulation. Background scatter for the value of each particular point of the simulation, with the superimposed conditional average (black solid lines).

In fact, fig. 7.9 shows how different regions of the domain contribute to the conditional mean through segmentation of the domain. First, a strongly reacting layer is defined for $\Omega > 15$ (coral lines) to capture the intense leading front surfaces, characterizing the flame tip areas. Due to the superadiabatic temperature therein, higher values for the production and diffusion terms are found. In addition, a change in tendency can be noted for the first diffusion term (top-left panel). Moreover, the second segmentation of the field in areas of $1 < \Omega < 15$ (yellow lines) is representative of the tails of the flame fronts, lateral regions of higher species concentration values accompanied by a loss of intensity in the reaction rate compared to the tip. Finally, the region of low species gradient $g_Y < 0.1$ (blue lines) locates the areas where the refilling process and heat losses dominate, be the inner part of the kernels configuration. However, the unsegmented total mean seems to be bounded to similar values to those of the planar-flame model due to overall domain averaging processes, see discussion below.

First, the well-differentiated areas of the flame tip can be analyzed use made of the symmetry axis in the propagation direction of each isolated flame. Figure 7.10 (left) displays the spatial distribution of temperature, species and reaction rate through the tip region of the example kernel, where a strong flame front characterized by the superadiabatic temperature can be noticed. Compared to the planar case shown in fig. 7.2, the temperature region above unity

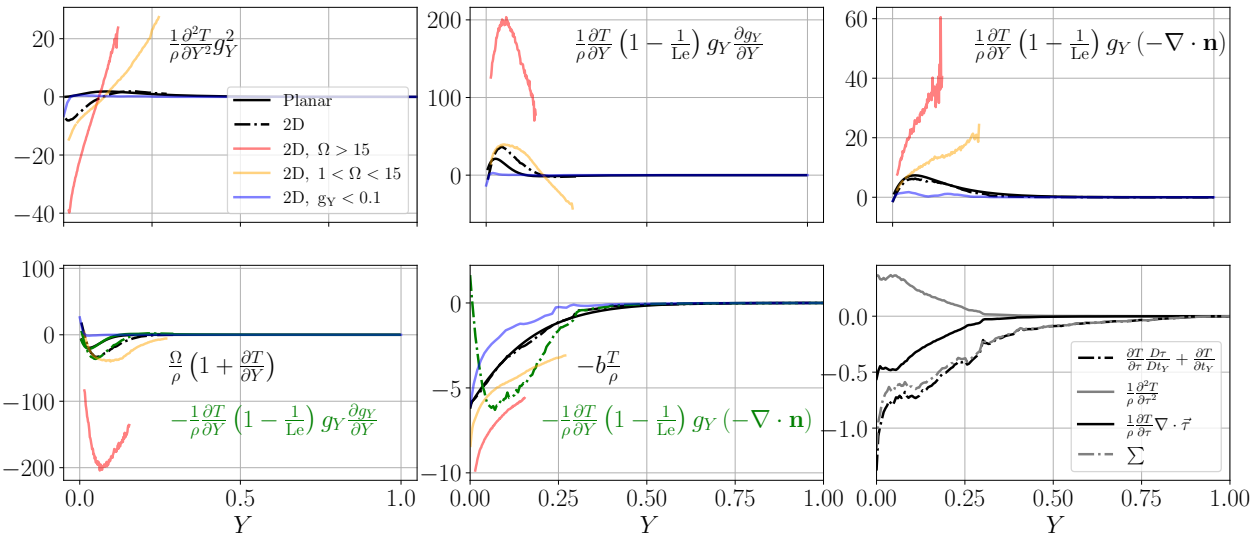

Figure 7.9: Conditional average comparison between the two-dimensional case and the planar-flame model. Segmentation of the results for $\Omega > 15$, $\Omega \in (1 - 15)$ and $g_Y < 0.1$. Coloring follows the label displayed in the first graph.

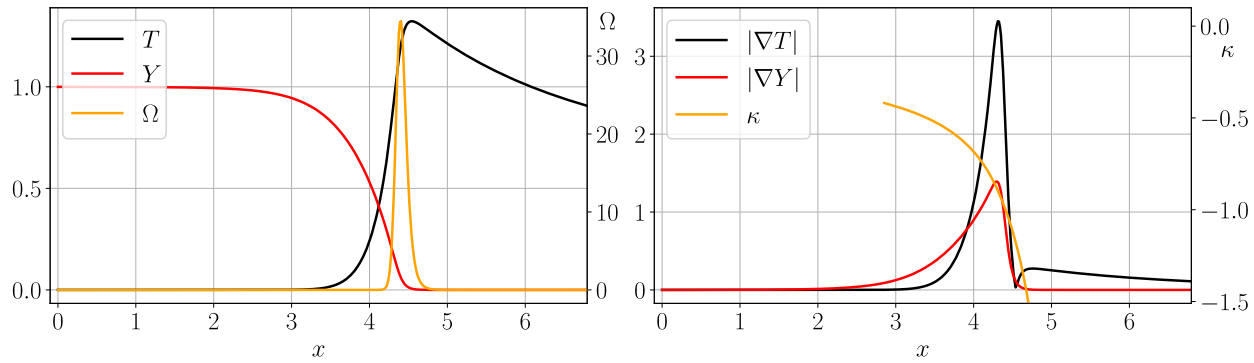

Figure 7.10: Longitudinal profiles along the symmetry axis of the selected main front in the 2D simulation. Flame-tip distribution over physical space.

found here gives rise to a higher production term (left) and sharper gradients (right). The curvature profile is also displayed, $\kappa = \nabla \cdot \mathbf{n}$, though only defined at places where the species gradient is above a certain minimum value.

Translated into the composition space, the energy equation terms are drawn in fig. 7.11. The reader shall note that although the unsteady terms depicted in the right panel (dot-dashed) are indicative of the transient motion, the order of magnitude is much smaller than the other dominating terms of the budget. In addition, those diffusive and production terms display higher orders of magnitude than the ones obtained for the planar flame in fig. 7.4. In addition, tangential terms play a minor role, already expected from their subtle presence at the two-dimensional fields displayed in fig. 7.7 around the flame-tip area.

In a first-order approximation, since the tangential terms are small, the tip region should be reproducible from the planar model of eq. (7.17), considering the normal contributions

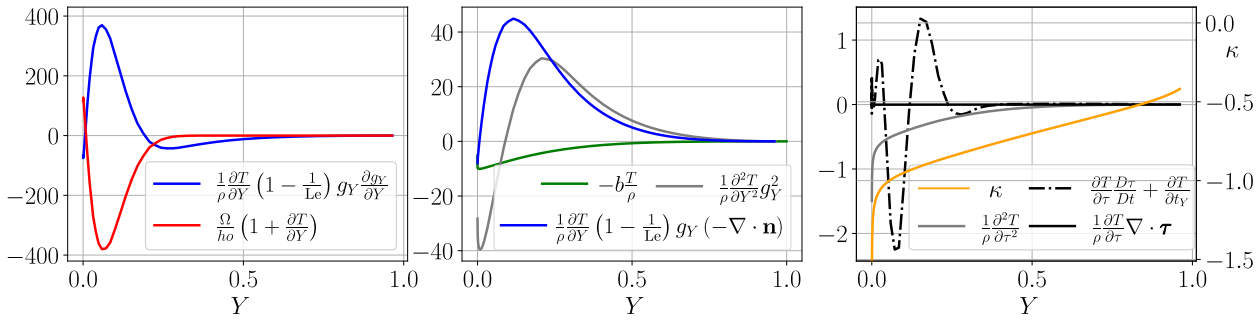

Figure 7.11: Composition-space distributions of the energy equation terms as evaluated from the flame-tip data over the symmetry axis shown in fig. 7.10.

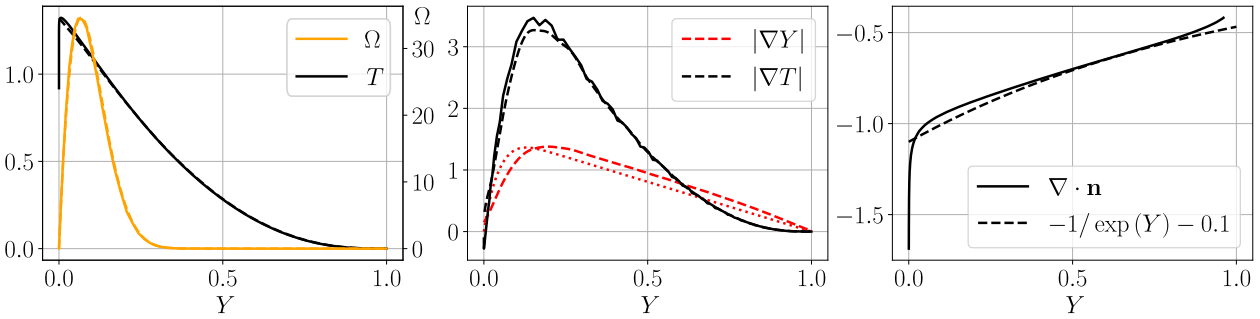

Figure 7.12: 2D longitudinal cut through the symmetry axis, to the first main front, compared to the one-dimensional planar composition model. The added curvature term corresponds to $\kappa = -1/\exp(Y) - 0.1$

supplemented with the extra diffusion curvature term, which can be retained from the complete derivation,

$$0 = \frac{\partial^2 T}{\partial Y^2} g_Y^2 + \frac{\partial T}{\partial Y}\left(1 - \frac{1}{\mathrm{Le}}\right) g_Y \left(\frac{\partial g_Y}{\partial Y} - \kappa\right) + \Omega\left(1 + \frac{\partial T}{\partial Y}\right) - bT. \tag{7.19}$$

Since the curvature term at the norm gradient equation is not too high, the profile remains similar to the planar one, this time multiplied by a factor related to the increase of the production term in eq. (7.14), and linked to the properties of the superadiabatic region. The solution is converged with prescribed boundary conditions $T(1) = 0$ and $T(0) = T_{\max}$ matched with the estimations. The computation consists of a pseudotransient integration in the composition space, use made of a RK4, taking into account the selected curvature distribution $\kappa(Y)$ and progressively increasing the heat-loss parameter from the planar solution with $b = 0$ to the selected value, $b = 1$, in the following results. Further information about the numerical computation can be consulted in the appendix E.

Figure 7.12 compares the actual distributions in composition space extracted from the two-dimensional data over the symmetry axis (solid lines) with the 1D-curvature-model energy eq. (7.19) in dashed lines. The distribution of the norm of the species gradient g_Y employed here for the computation is the one extracted from the simulation data (solid red in the middle graph), with negligible changes expected if including the planar-model distribution (dashed red). The curvature parameter κ is fixed to an exponential due to the logarithmic

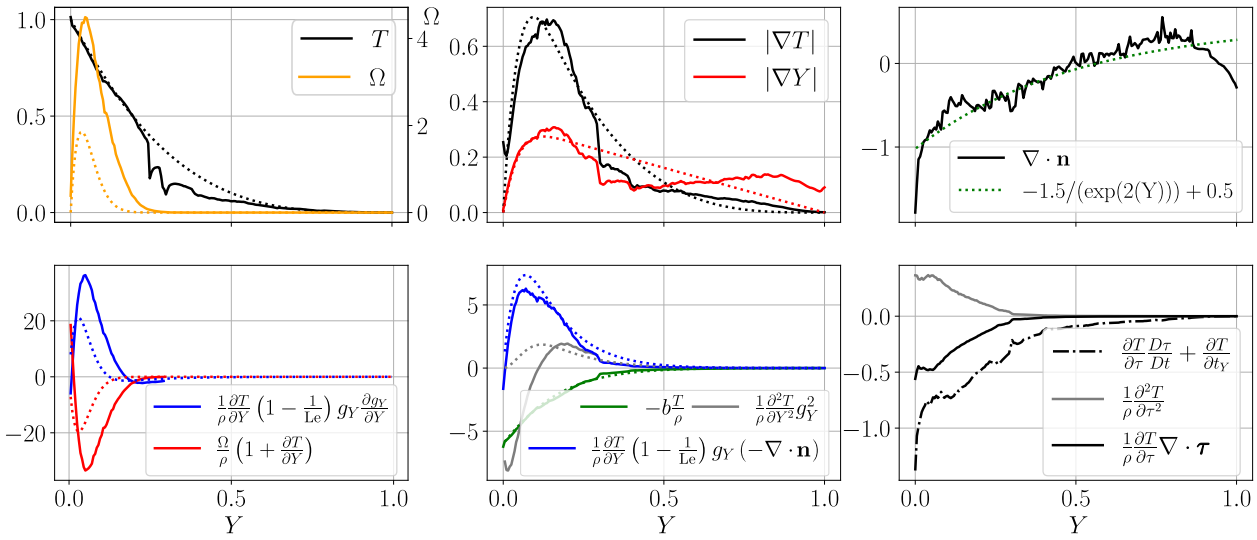

Figure 7.13: Conditional means of the variables (top) and energy equation terms (bottom) as evaluated from the complete 2D simulation in comparison to the planar-flame model in composition space with a curvature distribution (dashed), and equal heat-loss coefficient $b = 1$.

character of the species variation. The main trends are completely recovered qualitatively, corroborating that tangential terms do not play a determining role here and that the extended planar-flame model with curvature and heat losses is able to characterize the flame-tip region.

Finally, the overall conditional mean curves evaluated from the whole domain are displayed in fig. 7.13, and compared to the planar-flame model with curvature developed above. It should be noted that both data sets show a good agreement for a fit of the averaged curvature $\kappa = -1.5/\exp(2Y) + 0.5$. However, non-negligible changes in the importance of the reaction-diffusion balance can be detected, while mostly closing the budget of the rest of terms. A finite discontinuity, or step, is observed in the temperature and gradients distributions. As seen in fig. 7.14, the step is located at $Y \simeq 0.25$, which indicates the maximum values of species concentration with noticeable combustion processes, both tip ($\Omega > 15$) and lateral fronts ($1 < \Omega < 15$). To the right of the step only diffusion processes apply, both at the front and rear parts of the structure, with unburnt preheated mixture and the cold refilling of the wake respectively. The conditional average of those two distinguished regions produces a reduction in the mean temperature and grandients, conforming the aforementioned step.

7.4 Composition-space remarks

The complete description of the energy and species conservation equations in composition space has proven useful to highlight the dominant physical mechanisms acting at different regions of the reactive domain. A characteristic one-dimensional model can be developed for adequate representation of the tips of the flame front, which account for the curvature effect to overcome strong heat losses. In addition, the spatial distribution of normal and tangential contributions is identified, helping to provide further understanding on the refilling processes

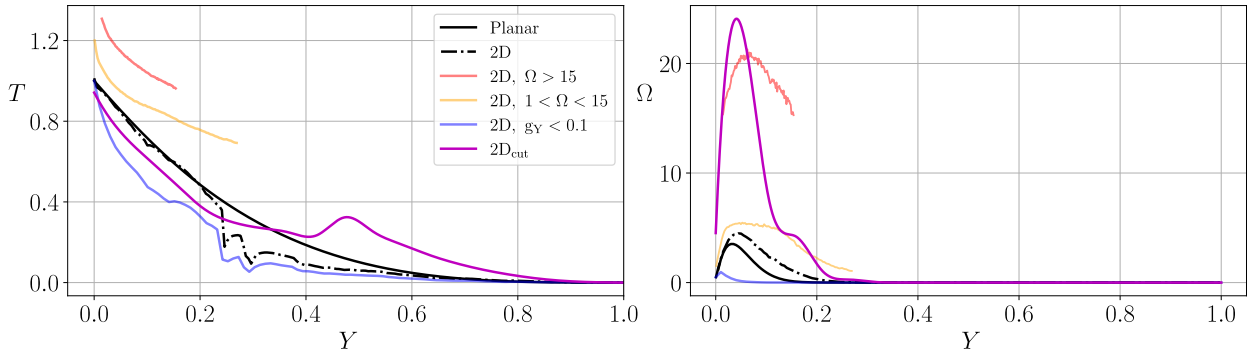

Figure 7.14: Mean conditional comparison between the two-dimensional case and the planar-flame model. Segmentation of the results for $\Omega > 15$, $\Omega \in (1 - 15)$ and $g_Y < 0.1$. Coloring follows the label displayed in the first graph.

of the wakes of products. Finally, it should be noted that the conditional average agreement with a planar base case in absence of curvature requires further study in order to confirm the physical arguments of the coincidence. In turn, we should point out the main idea of this section, which proves that a good fit of the conditional averages with a simple planar flame does not ensure the correct reproduction of disparate dynamics that show extremely disperse scatters of behaviors for the same independent variable of potential tabulation Y. Therefore, new grounds for additional studies are granted in order to correctly model the segmented regions of the flow.

This section addressing the analysis in composition space was developed in collaboration with Prof. Luc Vervisch after a two-month research visit in the summer of 2024 at L'Institut National des Sciences Appliquées (INSA) in Rouen, France.

Chapter 8

Discussion

This chapter focuses on the physical interpretation of the findings presented throughout this work. Key results are highlighted, emphasizing their relevance to the underlying configurations and illustrating the common thread that unifies and lends cohesion to the overall outcomes.

Scale separation analysis is a powerful tool that has achieved significant success in classical fluid dynamics. This technique is employed here to provide clearer insights into the processes and mechanisms involved in the formation of weak isolated flames propagating over lean hydrogen-air mixtures. Specifically, the studies presented in this document are based on the simplified formulation of very narrow channels, which adequately reduces the configuration to a quasi-two-dimensional benchmark. Geometrical and thermo-physical considerations are explored to develop reduced models for premixed combustion and heat transfer. This simplifications facilitate some theoretical analyses and reduce the computational cost of simulations while accurately reproducing the behaviors found in experimental Hele-Shaw chambers, the configuration addressed in this work. However, it should be noted that the simplified mathematical modeling used in this thesis is not applicable outside of these partially confined scenarios.

First, the results obtained through the initial numerical simulations (chapter 4) point out that the different behaviors observed in previous studies, two different types of isolated flame kernels, can take place under the same combination of controlling parameters. Earlier works related the appearance of double or single steady flames to buoyancy effects, conditioning the appearance of each kernel to the direction of propagation relative to the gravitational acceleration, namely upward or downward propagation (Martínez-Ruiz et al., 2019, Veiga-López, Kuznetsov, et al., 2020). Specifically, the weaker circular flame solution and the slightly more intense double-cell flame were analyzed in detail for different combinations of the buoyancy effect and intensity of relative heat losses (owing to the separation of the plates in experimental setups). The numerical simulations of this work intended to address these behaviors through the exploration of the parametric space of stable solutions. Modification of heat-release (mixture related), heat-loss (vessel related) and buoyancy (orientation related) parameters helped to identify the common grounds where the two different flame configurations can take place. In fact, an overlaping region of the parametric space for both types was found, indicating a multiplicity of stable solutions that propagate over the same mixture at different

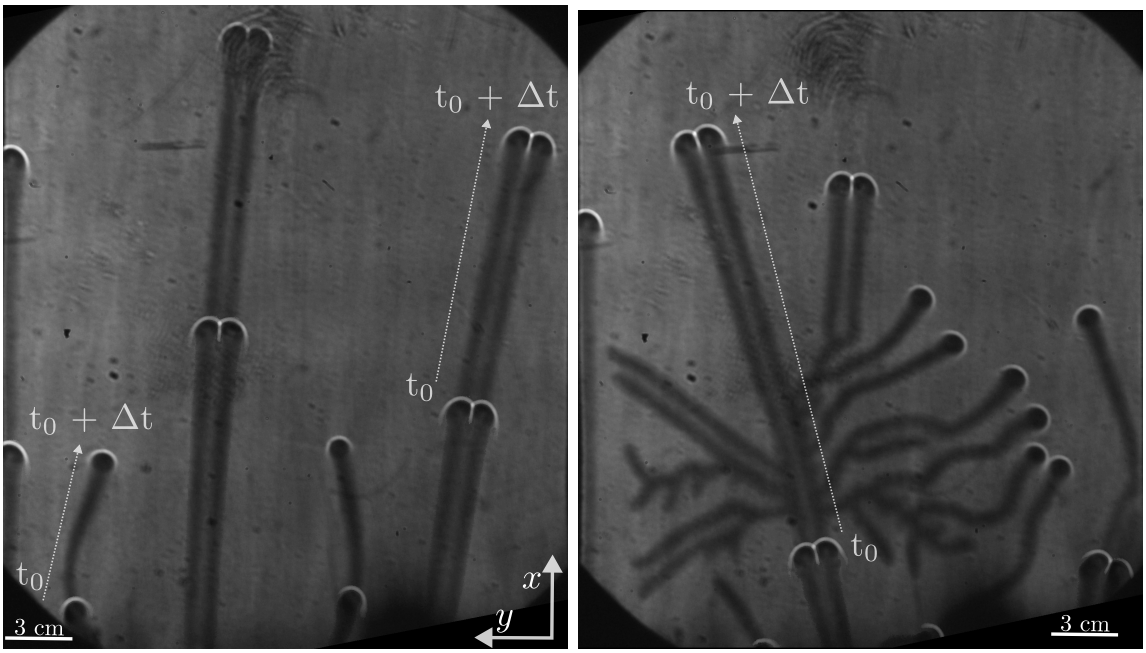

Figure 8.1: Schlieren imaging results confirming the predicted multiplicity of kernels of H_2-air mixtures in Hele-Shaw chambers, reproduced from Palomeque-Santiago et al., 2024.

speeds (Domínguez-González et al., 2023), which was never observed before.

The multiplicity of stable solutions was an unexpected outcome of the study. A subset of the common parametric space was identified for zero buoyancy effects, which drove collaborative efforts on new horizontal experimental configurations with scientific colleagues at various research institutions. Most importantly, these experiments later confirmed both predicted structure types in real scenarios and their bistable character (Palomeque-Santiago et al., 2024), see fig. 8.1. These isolated flame kernels were found within channels of $h = 4$ mm for the range of hydrogen concentration %vol. $H_2 \in [7.95 - 8.12]$, whose corresponding "ultra-lean" equivalence ratio is around $\phi = 0.206$. The scales of circular flame kernels found therein involve sizes of $\delta_k = 1.2$ cm and propagation speeds $S_u = 4$ cm/s.

Moreover, the formal presentation of both steady configurations is not restricted to their occurrence in the parametric space. The main stable structures of these types of flames is further analyzed. Specifically, two main effects that produce these weak premixed flames in confined scenarios are identified. One, the key role of large mass diffusivity of hydrogen fuel in ultra lean mixtures and, two, the conductive heat losses through the walls that form narrow gaps. The progressive increasing of the latter forces the cooling of the gas and grants the local increase of curvature of flames where differential diffusion acts to overcame this effect, enabling the reaction of mixtures below the lean flammability limit. The combined action of both effects gives rise to this type of isolated kernels. Although hydrogen is not strictly necessary for this outcome, a low-Lewis number of the fuel is required to warrant the survival of the flame through differential diffusion.

Second, a question remained open on the development of either one stable configuration or the other during the transient of initiation. Therefore, additional work on transient simulations

was developed (chapter 5) to identify the characteristic events that caused the differentiation of kernels. The results provided by different initiation conditions through tailored temperature and species profiles unveiled various mechanisms in the consolidation of circular structures, double-cell flames or complete extinction of the reactive flow (Domínguez-González et al., 2024). The splitting and merging of isolated flames point out the relevance of interactions between kernels to produce stable configurations after the transient stage. In addition, two physical aspects mark the ignition process, the initial amount of energy and the spatial distribution of its deposition. In fact, a considerable understanding of the experimental variability was achieved thanks to the introduction of irregular noise in the initiation transient, characteristic of the stochastic spark-plug ignition in real experiments. Non-regular initial conditions and interaction between kernels are required to obtain both stable solutions on the same run.

Additionally, the slow propagation speed of circular flames, confirmed in the experimental studies, and their ring-shaped reaction region, obtained from the numerical simulations, helped to directly relate these structures to the canonical flame ball problem. Therefore, a third study on the side of the theoretical discussion (chapter 6) proposed an asymptotic analysis of the circular flame structure. The methodology of this work enabled the description of different regions separated in a far field dominated by convection, a near field controlled by diffusion and heat losses, and a thin reactive layer involving the thermochemical properties of the combustion process. The scales of the characteristic planar flame construct are strongly modified owing to the effect of heat losses, which yield thermal scales much smaller than the adiabatic configuration. This fact, that remains coherent with the previous knwoledge extracted from the simulations, highlights the requirement of extra processes that enable the survival of the reaction in the thermal quenching limit.

Furthermore, the theoretical descriptions of the fluid variables enabled the imposition of constraints related to the chemical reaction, as is typically done in classical configurations (Fernández-Tarrazo et al., 2011). Although experiments and simulations yield a particular flame size, speed and temperature, the theoretical results indicate that diverse combinations of sizes and propagation speeds of the isolated structures should be attainable. The type of structure was discussed to be prescribed by the mixture and vessel conditions in the parametric space, but the quantitative properties of each kernel remain undefined. These properties should be explored then, probably depending on the ignition transient and initial amount of energy released. Nevertheless, new questions on the validity of the simplified theoretical results may arise. Specially, the incorporation of additional mechanisms to the formulation or detailed chemical models may be desirable to produce quantitative predictions in exact agreement with experiments.

Finally, the data and knowledge obtained from the wide set of studies is used to investigate some additional points. The fourth work of this project (chapter 7 involves a local analysis of the physical mechanisms and one-dimensional modeling in composition space. The results of the analysis show that there is a direct relation between the heat losses of the flow to the environment through the plates and the curvature that is induced in the flame front (or size of the circular kernel). The increase of intensity in off-plane heat transfer implies that curvature must be enhanced to sustain a local temperature that maintains the combustion process

active, as hypothesized in previous analyses. However, excessive increase of the former induces a reduced flame size that leads to complete extinction. In addition, the detailed identification of normal and tangential local effects related to preferential diffusion and curvature has helped to provide a deeper understanding of the main processes involved in the propagation of isolated structures. In conclusion, the advancing tip of the kernel acts as a planar flame with secondary curvature and heat losses effects, while the lateral tails and wake of products involve major tangential effects that remain negligible in the global picture.

Furthermore, this specific treatment of the conservation equations proves useful for the construction of simplified models. The classical planar flame model is known to be a virtual construct impossible to reproduce in real life, though of conceptual use in understanding the thermochemical properties of reactive flows. However, coherent introduction of heat losses and flame curvature effects in such a simplified benchmark, helps to reproduce a complete set of behaviors that is of great importance in describing complex flows, such as turbulent combustion scenarios, in the composition variable space. Therefore, the exploration of particular processes in well-defined scenarios is a fruitful task to improve the general knowledge and modeling with physical arguments.

All things considered, this thesis represents a coherent effort that advances the understanding of the fundamental building blocks of isolated stable flames. The well-defined kernels serve as canonical configurations, which have been instrumental in driving significant progress in the field. They also provide a comprehensive picture of the key characteristics of confined lean hydrogen flames, potentially paving the way for future studies and fostering improved understanding within the broader scientific community.

Chapter 9

Concluding remarks

The objectives of this piece of study are aligned with the transition of the power generation and transport sectors towards cleaner and sustainable strategies. The decarbonization of difficult-to-electrify applications implies that non-pollutant combustion processes are required. Keeping this in mind, several alternative fuels have been proposed in the last decades to drive this change, with hydrogen playing a major role in eliminating CO_2 emissions.

In addition to the potential challenges associated with the production, transport, and storage of hydrogen, numerous issues remain unresolved regarding its direct application in combustion systems. Specifically, the direct reaction of hydrogen and air in non-premixed flames results in extremely high flame temperatures, which reduce the efficiency of thermal devices and lead to the generation of large quantities of NO_x pollutants. Consequently, premixed combustion is preferred as it helps maintain moderate temperatures and reduce harmful emissions. However, premixed flames introduce additional complexities due to the ability of the reacting front to propagate through the mixture, making flashback and various flame instabilities significant concerns. Moreover, the presence of accidental leakage in the surroundings of hydrogen-fueled devices produces equivalent mixtures that can be ignited with very low ignition energies and give rise to hazardous propagating flames.

Numerous scientific advances have been achieved in the last decades regarding the fundamental behavior of hydrogen combustion. Nevertheless, important challenges related to the widespread use of this fuel remain unsolved, specially those related to safety issues and explosion hazards. In this dissertation, numerical and theoretical analyses of the propagation of weak hydrogen-air flame kernels have been explored, shedding some light on the understanding of the fundamentals of these structures.

All things considered, these results have widely improved the understanding of the physical causes and dynamics of such particular flames that may be object of interest among preventing strategies that tackle potential risks of hydrogen use. Although not precisely intense or destructive, these weak reactions can pass unnoticed and bring the seed of catastrophic damage to not-so-lean mixtures and not-so-small crevices. Moreover, the side products of this study can be of further relevance to part of the scientific community devoted to the use of lean premixed hydrogen flames in technological devices.

9.1 Future prospects

The main findings of this thesis demonstrate that singular structures can emerge in real-life scenarios under various configurations. However, the stable regimes and the dynamics leading to them are not the sole points of interest in this specific field. To extend the validity of these results and deepen our understanding of the primary reactive processes, further particular investigations are here proposed among others.

First, the stability analysis of various theoretical structures should be prioritized to rule out steady-state solutions that may not be feasible in practical scenarios. In this regard, supplementary experiments with constant flow feed could prove highly valuable in the quest for stabilizing such flames. Specifically, the ability to control these flames in certain configurations may hold relevance for novel technological applications, rather than being limited to addressing safety concerns.

Furthermore, the theoretical characterization of nearly circular flames has been pivotal in understanding the structure and leading-order mechanisms underpinning these kernels. Expanding the theoretical framework to encompass double-cell structures, which lack cylindrical symmetry, poses a significant challenge but promises substantial advancements in extending the current body of knowledge.

Finally, it would be beneficial to develop extended models in the composition space. Such efforts could elucidate the effects of highly diffusive fuels, like hydrogen, in turbulent combustion. As an additional benefit, this approach could facilitate the use of reduced chemical tabulations (flamelets) to accurately replicate heterogeneous flame dynamics.

References

Abramowitz, M., & Stegun, I. A. (1964). *Handbook of mathematical functions with formulas, graphs, and mathematical tables* (Vol. 55). US Government printing office.

Ballossier, Y., Boivin, P., & Almarcha, C. (2024). Three dimensional shapes of hydrogen-air flames within millimetric hele shaw cells. *International Journal of Hydrogen Energy*, *60*, 333–341.

Baukal Jr, C. E. (2020). *A gallery of combustion and fire*. Cambridge University Press.

Bezdek, R. H. (2018). The hydrogen economy and jobs of the future. *Renewable Energy and Environmental Sustainability*.

Bonnet, A. (1995). Non-uniqueness for flame propagation when the lewis number is less than 1. *European Journal of Applied Mathematics*, *6*(4), 287–306.

Buckmaster, J., & Joulin, G. (1991). Flame balls stabilized by suspension in fluid with a steady linear ambient velocity distribution. *Journal of Fluid Mechanics*, *227*, 407–427.

Buckmaster, J., Joulin, G., & Ronney, P. D. (1990). The structure and stability of nonadiabatic flame balls. *Combustion and Flame*, *79*(3-4), 381–392.

Canuto, C., Hussaini, M. Y., Quarteroni, A., & Zang, T. A. (2007). *Spectral methods: Fundamentals in single domains*. Springer Science & Business Media.

Carpio, J., Martínez-Ruiz, D., Liñán, A., Sánchez, A. L., & Williams, F. A. (2020). Hysteresis in the vaporization-controlled inertial regime of nonpremixed counterflow spray combustion. *Combustion Science and Technology*.

Chen, X., Lu, Z., & Wang, S. (2017). Near limit premixed flamelets in hele-shaw cells. *Proceedings of the Combustion Institute*, *36*(1), 1585–1593.

Clavin, P., Fife, P., & Nicolaenko, B. (1987). Multiplicity and related phenomena in competing reaction flames. *SIAM Journal on Applied Mathematics*, *47*(2), 296–331.

Clavin, P., & Searby, G. (2016). *Combustion waves and fronts in flows: Flames, shocks, detonations, ablation fronts and explosion of stars*. Cambridge University Press.

Dagdougui, H., Sacile, R., Bersani, C., & Ouammi, A. (2018). *Hydrogen infrastructure for energy applications: Production, storage, distribution and safety*. Academic Press.

Daou, R., Daou, J., & Dold, J. (2003). Effect of heat-loss on flame-edges in a premixed counterflow. *Combustion Theory and Modelling*, *7*(2), 221.

Domínguez-González, A., Encinar, M. P., & Martínez-Ruiz, D. (2024). Pathway dynamics to double-cell premixed flames in lean hydrogen–air mixtures. *Proceedings of the Combustion Institute*, *40*(1-4), 105496.

Domínguez-González, A., Martínez-Ruiz, D., & Sánchez-Sanz, M. (2023). Stable circular and double-cell lean hydrogen-air premixed flames in quasi two-dimensional channels. *Proceedings of the Combustion Institute*, *39*(2), 1731–1741.

Edwards, P. P., Kuznetsov, V. L., & David, W. I. (2007). Hydrogen energy. *Philosophical Transactions of the Royal Society A: Mathematical, Physical and Engineering Sciences*, *365*(1853), 1043–1056.

Elyanov, A., Golub, V., Volodin, V., & Alekhnovich, P. (2024). Decay of a hydrogen-air flame front to cup-like cells in a narrow horizontal gap. *Process Safety and Environmental Protection*, *191*, 1872–1882.

Etikyala, S., & Sujith, R. I. (2017). Change of criticality in a prototypical thermoacoustic system. *Chaos: An Interdisciplinary Journal of Nonlinear Science*, *27*(2).

Fernández-Galisteo, D., Dejoan, A., Melguizo-Gavilanes, J., & Kurdyumov, V. N. (2023). A three-dimensional study of the influence of momentum loss on hydrodynamically unstable premixed flames. *Proceedings of the Combustion Institute*, *39*(2), 1545–1554.

Fernández-Galisteo, D., Kurdyumov, V. N., & Ronney, P. D. (2018). Analysis of premixed flame propagation between two closely-spaced parallel plates. *Combustion and Flame*, *190*, 133–145.

Fernández-Galisteo, D., Sánchez, A., Liñán, A., & Williams, F. A. (2009). One-step reduced kinetics for lean hydrogen–air deflagration. *Combustion and flame*, *156*(5), 985–996.

Fernández-Tarrazo, E., Sánchez, A. L., Liñán, A., & Williams, F. A. (2011). The structure of lean hydrogen-air flame balls. *Proceedings of the Combustion Institute*, *33*(1), 1203–1210.

Fernández-Tarrazo, E., Sánchez, A. L., Liñán, A., & Williams, F. A. (2012). Flammability conditions for ultra-lean hydrogen premixed combustion based on flame-ball analyses. *International Journal of Hydrogen Energy*, *37*(2), 1813–1825.

Frazier, K. (2007). Muskingum river plant, hydrogen explosion. *Edison Electric Institute Spring Meeting*.

Freefem. (n.d.). https://freefem.org/

Friedlingstein, P., O'Sullivan, M., Jones, M. W., Andrew, R. M., Hauck, J., Landschützer, P., Le Quéré, C., Li, H., Luijkx, I. T., Olsen, A., Peters, G. P., Peters, W., Pongratz, J., Schwingshackl, C., Sitch, S., Canadell, J. G., Ciais, P., Jackson, R. B., Alin, S. R., ... Zeng, J. (2024). Global carbon budget 2024. *Earth System Science Data Discussions*, *2024*, 1–133.

Grcar, J. F. (2009). A new type of steady and stable, laminar, premixed flame in ultra-lean, hydrogen–air combustion. *Proceedings of the Combustion Institute*, *32*(1), 1011–1018.

Hieber, C., & Gebhart, B. (1968). Low reynolds number heat transfer from a circular cylinder. *Journal of Fluid Mechanics*, *32*(1), 21–28.

Jiménez, J. (2018a). Coherent structures in wall-bounded turbulence. *Journal of Fluid Mechanics*, *842*, P1.

Jiménez, J. (2018b). Machine-aided turbulence theory. *Journal of Fluid Mechanics*, *854*, R1.

Kagan, L., & Sivashinsky, G. (1997). Self-fragmentation of nonadiabatic cellular flames. *Combustion and Flame*, *108*(1-2), 220–226.

Kailasanath, K. (2003). Recent developments in the research on pulse detonation engines. *AIAA Journal*, *41*(2), 145–159.

Kassam, A.-K., & Trefethen, L. N. (2005). Fourth-order time-stepping for stiff pdes. *SIAM Journal on Scientific Computing*, *26*(4), 1214–1233.

Kurdyumov, V. N. (2019). Propagation of premixed isobaric flames in narrow channels with heat-losses: The asymptotic analysis revised and reliance on the flame-sheet model. *Combustion and Flame*, *206*, 138–149.

Kurdyumov, V. N., Fernández-Galisteo, D., & Jiménez, C. (2020). Superadiabatic small-scale combustor with counter-flow heat exchange: Flame structure and limits to narrow-channel approximation. *Combustion and Flame*, *222*, 233–241.

Kurdyumov, V. N., & Matalon, M. (2013). Flame acceleration in long narrow open channels. *Proceedings of the Combustion Institute*, *34*, 865–872.

Kuznetsov, M., & Grune, J. (2019). Experiments on combustion regimes for hydrogen/air mixtures in a thin layer geometry. *International Journal of Hydrogen Energy*, *44*(17), 8727–8742.

Lagerstrom, P. A. (2013). *Matched asymptotic expansions: Ideas and techniques* (Vol. 76). Springer Science & Business Media.

Lu, T., & Law, C. K. (2009). Toward accommodating realistic fuel chemistry in large-scale computations. *Progress in Energy and Combustion Science*, *35*(2), 192–215.

Lu, Z., & Li, J. (2021). Dynamics of flame rings in a thermally-conductive narrow channel: A numerical experiment. *Combustion Theory and Modelling*, 1–17.

Martínez-Ruiz, D., Veiga-López, F., Fernández-Galisteo, D., Kurdyumov, V. N., & Sánchez-Sanz, M. (2019). The role of conductive heat losses on the formation of isolated flame cells in hele-shaw chambers. *Combustion and Flame*, *209*, 187–199.

Matkowsky, B., & Sivashinsky, G. (1979). Asymptotic derivation of two models in flame theory associated with the constant density approximation. *SIAM Journal on Applied Mathematics*, *37*(3), 686–699.

Melguizo-Gavilanes, J., Fernández-Galisteo, D., Dejoan, A., Sánchez-Sanz, M., & Kurdyumov, V. N. (2021). Three-dimensional simulations of lean h2-air flames propagating in a narrow gap: On the validity of the quasi-two-dimensional approximation. *International Conference on Hydrogen Safety*.

Minaev, S., Kagan, L., Joulin, G., & Sivashinsky, G. (2001). On self-drifting flame balls. *Combustion Theory and Modelling*, *5*(4), 609.

Pagliaro, M., & Iulianelli, A. (2020). Hydrogen refueling stations: Safety and sustainability. *General Chemistry*, *6*(1), 190029.

Palomeque-Santiago, R., Domínguez-González, A., Martínez-Ruiz, D., Rubio-Rubio, M., Fernández Tarrazo, E., & Sánchez-Sanz, M. (2024). Unveiling the bi-stable character of stealthy hydrogen–air flames. *Physics of Fluids*, *36*(8).

Reuter, C. B., Won, S. H., & Ju, Y. (2016). Experimental study of the dynamics and structure of self-sustaining premixed cool flames using a counterflow burner. *Combustion and Flame*, *166*, 125–132.

Ritchie, H., Roser, M., & Rosado, P. (2020). CO_2 and greenhouse gas emissions. *Our world in data*.

Ronney, P. D. (1990). Near-limit flame structures at low lewis number. *Combustion and Flame*, *82*(1), 1–14.

Ronney, P. D., Whaling, K., Abbud-Madrid, A., Gatto, J., & Pisowicz, V. (1994). Stationary premixed flames in spherical and cylindrical geometries. *AIAA Journal*, *32*(3), 569–577.

Ronney, P. D., Wu, M.-S., Pearlman, H. G., & Weiland, K. J. (1998). Experimental study of flame balls in space: Preliminary results from sts-83. *AIAA Journal*, *36*(8), 1361–1368.

Salvi, B. L., & Subramanian, K. A. (2015). Sustainable development of road transportation sector using hydrogen energy system. *Renewable and Sustainable Energy Reviews*, *51*, 1132–1155.

Sánchez, A. L., & Williams, F. A. (2014). Recent advances in understanding of flammability characteristics of hydrogen. *Progress in Energy and Combustion Science*, *41*, 1–55.

Scholtissek, A., Popp, S., Hartl, S., Olguin, H., Domingo, P., Vervisch, L., & Hasse, C. (2020). Derivation and analysis of two-dimensional composition space equations for multi-regime combustion using orthogonal coordinates. *Combustion and Flame*, *218*, 205–217.

Spalart, P. R., Moser, R. D., & Rogers, M. M. (1991). Spectral methods for the navier-stokes equations with one infinite and two periodic directions. *Journal of Computational Physics*, *96*(2), 297–324.

Staffell, I., Scamman, D., Abad, A. V., Balcombe, P., Dodds, P. E., Ekins, P., Shah, N., & Ward, K. R. (2019). The role of hydrogen and fuel cells in the global energy system. *Energy and Environmental Science*, *12*(2), 463–491.

Taneda, S. (1956). Experimental investigation of the wake behind a sphere at low reynolds numbers. *Journal of the Physical Society of Japan*, *11*(10), 1104–1108.

Thomas, J. K., Eastwood, C., & Goodrich, M. (2015). Are unconfined hydrogen vapor cloud explosions credible? *Process Safety Progress*, *34*(1), 36–43.

Van Dyke, M. (1982). *An album of fluid motion* (Vol. 176). Parabolic Press Stanford.

Van Oijen, J., Donini, A., Bastiaans, R., ten Thije Boonkkamp, J., & De Goey, L. (2016). State-of-the-art in premixed combustion modeling using flamelet generated manifolds. *Progress in Energy and Combustion Science*, *57*, 30–74.

Veiga-López, F., Kuznetsov, M., Martínez-Ruiz, D., Fernández-Tarrazo, E., Grune, J., & Sánchez-Sanz, M. (2020). Unexpected propagation of ultra-lean hydrogen flames in narrow gaps. *Physical Review Letters*, *124*(17), 174501.

Veiga-López, F., Martínez-Ruiz, D., Kuznetsov, M., & Sánchez-Sanz, M. (2020). Thermoacoustic analysis of lean premixed hydrogen flames in narrow vertical channels. *Fuel*, *278*, 118212.

Weeratunga, S., Buckmaster, J., & Johnson, R. (1990). A flame-bubble analogue and its stability. *Combustion and Flame*, *79*(1), 100–109.

Williams, F. A. (1985). *Combustion theory* (2nd Edition). Menlo Park, CA: Benjamin Cummings.

Yañez, J., Kagan, L., Sivashinsky, G., & Kuznetsov, M. (2023). Modeling of 2d self-drifting flame-balls in hele-shaw cells. *Combustion and Flame*, *258*, 113059.

Yañez, J., & Veiga-López, F. (2021). Theoretical analysis of the condensation of combustion products in thin gaseous layers. *Physics of Fluids*, *33*(8).

Zeldovich, IA, Barenblatt, Io, G., Librovich, VB, Makhviladze, & GM. (1985). *Mathematical theory of combustion and explosions*. United States.

Appendix A: FreeFEM computational notes

Convergence aspects

The numerical simulations performed for the work in chapter 4 were computed with Freefem^{++}, a finite element solver. The specific set of equations and boundary conditions stated above can be implemented using the weak variational formulation. Convergence to the steady state is achieved through a second order implicit algorithm of time step $dt = 1e-4$. Furthermore, adaptive mesh refinement is programmed to meet a mixed criteria based on the gradient of several fluid variables, T, p, Ω at each time step. In particular, the minimum size of triangle edge is set to $d_e = 0.01$, such that characteristic flame thicknesses δ_T of order unity are described by around one hundred elements.

The convergence study regarding the element size d_e and the span of the domain $x \in [-L/2, L/2]$, $y \in [-L/2, L/2]$, is offered in fig. 1. A mesh comparison for a change in minimum element size d_e is shown for clarity (c) in the cases $d_e = 0.02$ and $d_e = 0.05$. The profiles of temperature, velocity and species along the symmetry axis are shown to be in perfect agreement (a) for sizes of the elements d_e two and five times larger than the reference value used in the study, $d_e = 0.01$. Finally, solutions in larger domains of side $L = 34$ and 40 are compared to the reference cases presented above with $L = 28$ (b), with relative errors in the steady solution of $(S_{u34} - S_{u28})/S_{u28} = 1.6 \times 10^{-2}$ and $(S_{u40} - S_{u28})/S_{u28} = 1.3 \times 10^{-2}$.

For the sake of conciseness, the detailed analysis and validation against finite differences codes is not reproduced here. The reader is referred to the numerical Appendix in Martínez-Ruiz et al., 2019 for further information.

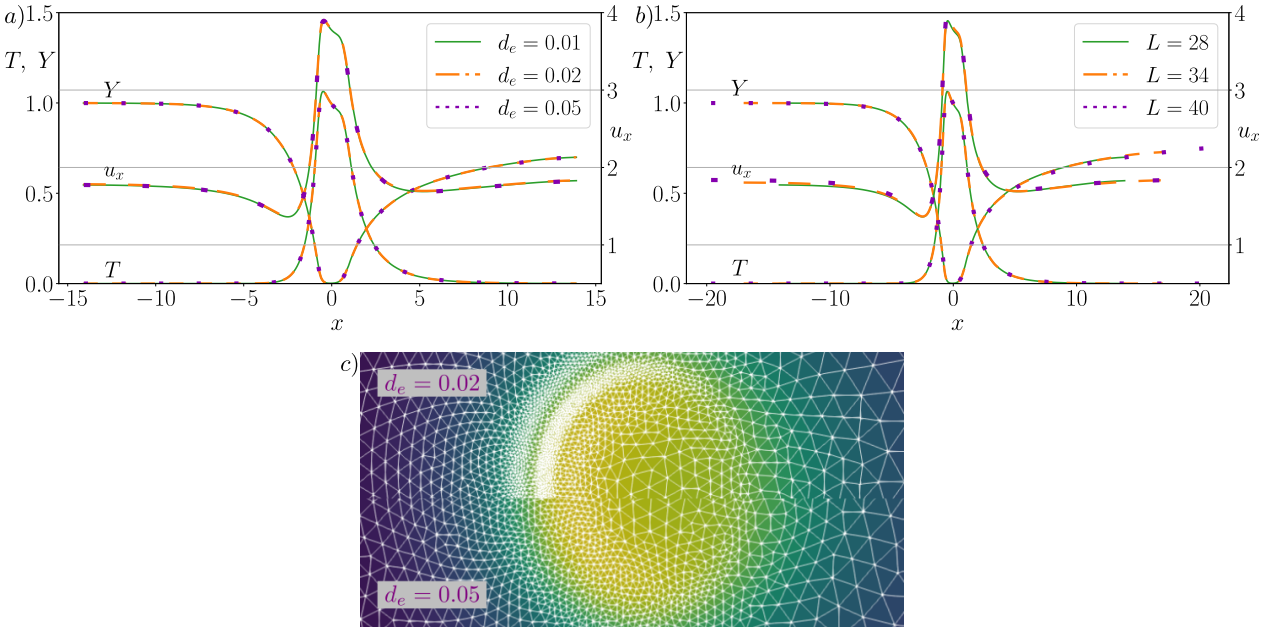

Figure 1: Stable solution profiles along x-axis for variations in the minimum element size d_e (a), the domain span L (b) and mesh refinement detail (c),

Variational formulation notes

The use of FreeFEM solver for the resolution of the system involves the weak formulation of the problem (variational formulation) where the equations are expressed in an integral way over the calculation domain. Green's identities are used to rewrite the divergence and laplacian operators,

$$\int_V \left[\Phi \left(\nabla \cdot \Gamma\right) + \Gamma \cdot \nabla\Phi\right] dV = \int_\Sigma \Phi \left(\Gamma \cdot \mathbf{n}\right) dS \tag{1}$$

$$\int_V \left[\Phi\nabla^2\Gamma + \nabla\Phi \cdot \nabla\Gamma\right] dV = \int_\Sigma \Phi \left(\nabla\Gamma \cdot \mathbf{n}\right) dS \tag{2}$$

Taking into account the test functions Φ (finite element functions) the laplacian terms of the equations implemented in our code are split up in a volume integral and a surface one which corresponds to the boundary condition involving the gradient of the variable Γ, use made of the second of Green's identities.

Appendix B: RK3CN2 integration notes

A Fourier-Fourier discretization of 2048^2 modes is used to compute the equations system governing the flow problem. The three main equations are rewritten here, the temperature, species and pressure equations,

$$\frac{\partial T}{\partial t} + u_x \frac{\partial T}{\partial x} + u_y \frac{\partial T}{\partial y} = \frac{\nabla^2 T}{\rho} + \frac{\Omega}{\rho} - \frac{bT}{\rho} \tag{3}$$

$$\frac{\partial Y}{\partial t} + u_x \frac{\partial Y}{\partial x} + u_y \frac{\partial Y}{\partial y} = \frac{1}{\mathrm{Le}} \frac{\nabla^2 Y}{\rho} + \frac{\Omega}{\rho} \tag{4}$$

$$\nabla^2 p = -q \left(\nabla^2 T + \Omega - bT \right) \tag{5}$$

The temporal integration scheme is a third-order Runge-Kutta second-order Crank-Nicolson method by Spalart et al., 1991. Being $\mathbf{u}$ a generic variable, the integration scheme works as follows,

$$\frac{\partial \mathbf{u}}{\partial t} = L(\mathbf{u}) + N(\mathbf{u}) \equiv R(\mathbf{u}) \tag{6}$$

The temporal derivative is built from a linear part plus a non-linear one. L is the linear operator, including viscous terms and pressure; and N the non-linear operator which comprises convection terms, in this case also production rate and part of the laplacian and heat losses.

$$\mathbf{u'} = \mathbf{u_n} + \triangle t \left[L\left(\alpha_1 \mathbf{u_n} + \beta_1 \mathbf{u'}\right) + \gamma_1 N_n \right], \tag{7}$$

$$\mathbf{u''} = \mathbf{u'} + \triangle t \left[L\left(\alpha_2 \mathbf{u'} + \beta_2 \mathbf{u''}\right) + \gamma_1 N' + \zeta_1 N_n \right], \tag{8}$$

$$\mathbf{u_{n+1}} = \mathbf{u''} + \triangle t \left[L\left(\alpha_3 \mathbf{u''} + \beta_3 \mathbf{u_{n+1}}\right) + \gamma_1 N'' + \zeta_2 N' \right], \tag{9}$$

This is a method composed of three sub-steps, combining implicit and explicit parts in addition to using the values from the previous sub-steps. $\mathbf{u_n}$, $\mathbf{u_{n+1}}$ indicate two consecutive temporal steps while $\mathbf{u'}$, $\mathbf{u''}$ correspond to the sub-step values. The integrator coefficients lead:

$$\begin{array}{llll} \gamma_1 = 8/15, & \gamma_2 = 5/12, & \gamma_3 = 3/4, & \zeta_1 = -17/60, \\ \alpha_1 = 29/96, & \alpha_2 = -3/40, & \alpha_3 = 1/6, & \zeta_2 = -5/12 \\ \beta_1 = 37/160, & \beta_2 = 5/24, & \beta_3 = 1/6, & \end{array} \tag{10}$$

Plugging-in eqs. (3), (4) and (5) into structure (6) reads,

$$\frac{\partial \widehat{T}}{\partial t} = -\left(\alpha_T k^2 + \gamma b\right) \widehat{T} - \widehat{\vec{u} \cdot \nabla T} + \Omega \widehat{(1+qT)} + (1 - \alpha_T \widehat{+ qT}) \nabla^2 T - b(1 - \widehat{\gamma + qT}) T \tag{11}$$

$$\frac{\partial \widehat{Y}}{\partial t} = -\frac{\alpha_Y k^2}{\mathrm{Le}} \widehat{Y} - \widehat{\vec{u} \cdot \nabla Y} - \Omega \widehat{(1+qT)} + \frac{(1 - \widehat{\alpha_Y + qT})}{\mathrm{Le}} \nabla^2 Y \tag{12}$$

$$k^2 \hat{p} = q\mu \left(-\mu k^2 \hat{T} + \hat{\Omega} - b\hat{T} \right) \tag{13}$$

$$\hat{\vec{u}} = -ik\hat{p} \tag{14}$$

where α_T, α_Y and γ are three coefficients which specify the portion of the diffusion and heat losses terms that will be calculated through the implicit or explicit term. The hat symbol denote the Fourier transform, the first spatial derivative rends $\partial/\partial x = -ik$, the second one $\partial^2/\partial x^2 = k^2$.

$$L_T = -\left(\alpha_T k^2 + \gamma b\right)\hat{T}; \quad L_Y = -\frac{\alpha_Y k^2}{\mathrm{Le}}\hat{Y} \tag{15}$$

$$N_T = -\widehat{\vec{u}\cdot\nabla T} + \Omega\,\widehat{(1+qT)} + (1-\alpha_T\widehat{+qT})\,\nabla^2 T - b\,(1-\widehat{\gamma+qT})\,T \tag{16}$$

$$N_Y = -\widehat{\vec{u}\cdot\nabla Y} - \Omega\,\widehat{(1+qT)} + (1-\alpha_Y\widehat{+qT})\,\nabla^2 Y \tag{17}$$

The following notes contain the basics of the code shell. The loop at the end of performs the temporal integration steps, calling RK3CN2 function, which contains the temporal scheme details. L is a function where the linear part of the equation is evaluated, while N takes the non-linear part; Li is the linear operator matrix.

```
def RK43CN3(L, N, phi):
    # First sub-step
    phi'   = phi  + dt*(alpha1 *L(phi)  + gamma1 *N(phi))
    phi'  /= 1 - beta1 *dt *Li

    # Second sub-step
    phi''  = phi' + dt*(alpha2 *L(phi') + gamma2 *N(phi') + zeta1 *N(
       phi))
    phi'' /= 1 - beta2 *dt *Li

    # Third sub-step
    phi    = phi'' + dt*(alpha3 *L(phi'')  + gamma3 *N(phi'') + zeta2
       *N(phi'))
    phi   /= 1 - beta3 *dt *Li

# Temporal loop
for i in range(it_max):
    RK3CN2(L, N, phi)
```

Appendix C: Segmentation and tracking code notes

In the context of the transient study, an in-house segmentation and tracking code is developed in Python to follow the reaction kernels over time and cluster the different events occurring during a simulation. General notes are given throughout this appendix to provide further details to the interested reader.

In general terms, in the first part of the code, the field is segmented and labeled. The Python library *scipy.ndimage* allows us to define a mask, based on the percolation threshold of the reaction rate, and create a numbering on the spatially connected domains found. The library facilitates the computation of certain functions on each of the labeled subsets. In the following code extract, the definition of the mask is presented. The use of *ng.label* function numbers the structures and, then, quantities linked to the previous number labels are calculated (averaged variables, maximum peaks, area...).

```
import scipy.ndimage as ng
# file lecture
variables[temp,spec,omeg...] = h5py.File(filename,'r')
# mask -- THRESHOLD
mask = (intensity).copy()>threshold_value
# labeling step, replacing ones with numbers
lbl, nlbl = ng.label(mask)
# average quantities over each variable
it_mean_phi1, it_mean_phi2... = map(lambda x: ng.measurements.mean(x,lbl,
   arrange(1, nlbl+1)),phi1,phi2...)
it_max_phi1,  it_max_phi2...  = map(lambda x: ng.measurements.maximum(x,
   lbl,arrange(1, nlbl+1)),phi1,phi2...)
it_min_phi1,  it_min_phi2...  =  map(lambda x: ng.measurements.mainimum(x,
   lbl,arrange(1, nlbl+1)),phi1,phi2...)
# Area -- pixels
count = ng.measurements.sum(mask, lbl,arrange(1,nlbl+1))
```

These operations are performed on each temporal step of the simulation. Therefore, the information of two consecutive time steps is linked thanks to the adjacency matrix, relating the spatial position of the labeled connected regions in this two consecutive steps. The rows of the matrix refer to the structures of the current time step and its columns to the structures of the previous step. For a specific row of the matrix, the elements that correspond to structures of the previous step (labeled by the column position) which spatially overlap with the present structure are marked with unity value, and zero otherwise. The loop used to built the adjacency matrix is presented here,

```
# conectivity step
last = None
if any(last):
    c = zeros((nlbl+1,nlast+1),dtype='i4')
    for ila, la in enumerate (ng.labeled_comprehension(bl,last,arrange(max
       (nlbl+1,nlast+1)),unique,'0',nan)):
        if isinstance(la, ndarray):
            c[la, ila] = 1
    cs.append(c)
# store labels for next conectivity
last, last = lbl, nlbl
```

The *ng.labeled_comprehension* function computes the function *unique* to the index positions of the current label matrix *lbl* which present the same label in the previous label matrix *last*. The loop is responsible for filling with a one the corresponding index positions. A simplified example with three-time steps is prepared to show how the adjacency matrix works. THe flow variable data reads,

$$\frac{\Omega}{\rho}\Big|_{t_1,t_2,t_3} = \begin{bmatrix} 5.1 & 5.2 & 4 & 4 \\ 5.2 & 5.5 & 4 & 5.2 \\ 4.8 & 4.2 & 3 & 5.1 \\ 5.3 & 5.1 & 4.2 & 4.2 \end{bmatrix}, \begin{bmatrix} 4.9 & 5.2 & 3.8 & 4 \\ 5.1 & 5.5 & 3.8 & 5.2 \\ 4.9 & 4.1 & 3 & 5.1 \\ 5.3 & 5 & 4.2 & 5.1 \end{bmatrix}, \begin{bmatrix} 4.9 & 5.2 & 3.8 & 4 \\ 5 & 5.5 & 3.8 & 5 \\ 5.1 & 4.1 & 3 & 5.2 \\ 5.1 & 5 & 4.2 & 5.1 \end{bmatrix}$$

Furthermore, its binarized matrixes can be computed

$$\frac{\Omega}{\rho}\Big|_{t_1,t_2,t_3} > \text{threshold value}, 5 = \begin{bmatrix} 1 & 1 & 0 & 0 \\ 1 & 1 & 0 & 1 \\ 0 & 0 & 0 & 1 \\ 1 & 1 & 0 & 0 \end{bmatrix}, \begin{bmatrix} 0 & 1 & 0 & 0 \\ 1 & 1 & 0 & 1 \\ 0 & 0 & 0 & 1 \\ 1 & 0 & 0 & 1 \end{bmatrix}, \begin{bmatrix} 0 & 1 & 0 & 0 \\ 0 & 1 & 0 & 0 \\ 1 & 0 & 0 & 1 \\ 1 & 0 & 0 & 1 \end{bmatrix}$$

A labeled matrix is returned for each binarized set by the *ng.label* function

$$\text{lbl}|_{t_1,t_2,t_3} = \begin{bmatrix} 1 & 1 & 0 & 0 \\ 1 & 1 & 0 & 2 \\ 0 & 0 & 0 & 2 \\ 3 & 3 & 0 & 0 \end{bmatrix}, \begin{bmatrix} 0 & 1 & 0 & 0 \\ 1 & 1 & 0 & 2 \\ 0 & 0 & 0 & 2 \\ 3 & 0 & 0 & 2 \end{bmatrix}, \begin{bmatrix} 0 & 1 & 0 & 0 \\ 0 & 1 & 0 & 0 \\ 2 & 0 & 0 & 3 \\ 2 & 0 & 0 & 3 \end{bmatrix}$$

The two adjacency matrices could be written as,

$$c|_{t_2,t_3} = \begin{bmatrix} 1 & 1 & 0 & 1 \\ 0 & 1 & 0 & 0 \\ 1 & 0 & 1 & 0 \\ 0 & 0 & 0 & 1 \end{bmatrix}, \begin{bmatrix} 1 & 1 & 1 & 0 \\ 0 & 1 & 0 & 0 \\ 1 & 0 & 0 & 1 \\ 0 & 0 & 1 & 0 \end{bmatrix}$$

where first row and column describe the overlap of the structure with the background of each instant. The elements of c out of these first row and column, c^*, represent the movement of the structures along the square domain.

$$c^*|_{t_2,t_3} = \begin{bmatrix} 1 & 0 & 0 \\ 0 & 1 & 0 \\ 0 & 0 & 1 \end{bmatrix}, \begin{bmatrix} 1 & 0 & 0 \\ 0 & 0 & 1 \\ 0 & 1 & 0 \end{bmatrix}$$

First, since the number of rows remains constant in this example, there are no structure splittings or extinctions. From the eye disposition of the first one, it is deduced that the labeling between the first step and the following is conserved. In the second case, a change in the labeling order occurs, the label 2 structure in t_3 corresponds to the label 3 structure in t_2.

By analyzing the movements of the ones in the adjacency matrices we can identify the different events that can occur, as a starting point: splitting processes, extinctions or just tag reordering. The identification of extinctions is based on the null sum of the columns, an 'old' structure does not correspond to any of the new ones; the splitting process is located where a column summation excedes unity.

```
c[:,0] = 0.;c[0,:] = 0.
nlbl  = len(c[:,0])-1
nlast = len(c[0,:])-1

nspl_index = 0
next_index = 0
# Extinction events
ext_index  = argwhere(sum(c,axis=0)==0.)[1::]
next_index = len(ext_index)

# Splitting events
spl_index  = argwhere(sum(c,axis=0)>1.) # old index
nspl_index = len(spl_index)             # n old str breaking
nspl       = sum(c[:,spl_index],axis=0) # n new str breaking
spl_new_index = []
for j in range(nspl_index):
    spl_new_index.append(argwhere(c[:,spl_index[j][0]]==1.))

# New structures
n_new = sum(nspl)

# No-event
noe_index = argwhere(sum(c,axis=0)==1.)
nnoe_index = len(noe_index)
noe_new_index = []
for j in range(nnoe_index):
    noe_new_index.append(argwhere(c[:,noe_index[j][0]]==1.))
```

Once these basic movements are identified, a coordinate card is created to allow the tracking, a matrix whose rows keep the structures while the columns store the different temporal steps [k,i]=[structure index, time step]. In the following code extract, related to one time step, a new temporal column is created to store the new data. The new time column is filled with a nan if the structure 'old' index corresponds to an already dead or divided structure (already nan in the card), or a splitting or extinction process just detected in the current time step; if it corresponds to a non-event index, the card is filled with the new index which corresponds to the old structure stored in that index of the card. Now, as many rows are created as there are new structures (splitting processes already identified), and filled with the new splitting index, solving any reorder issue problem here. In addition, while creating the coordinate card, variable cards are also created so, each row of these matrices represents the temporal evolution of a variable associated with a single structure.

```
nstr  += n_new

# new time-step column addition
str_card  = append(str_card,zeros(nstr-n_new)[:,nw],axis=1)
phi_card  = append(tstr,zeros(nstr-n_new)[:,nw],axis=1)

for k in range(nstr-n_new):
    if str_card[k,i-1] != str_card[k,i-1]:      # Previous ext/splt
        str_card[k,i] = nan
        phi_card[k,i] = nan
```

```
    if np.any(ext_index == str_card[k,i-1]):    # Extinction process
        str_card[k,i] = nan
        phi_card[k,i] = nan

    if np.any(spl_index == str_card[k,i-1]):    # Splitting process
        str_card[k,i] = nan
        phi_card[k,i] = nan

    if np.any(noe_index == str_card[k,i-1]):     # No event
        aho           = int(str_card[k,i-1])
        str_card[k,i] = int(noe_new_index[int(argwhere(noe_index == aho)
            [0][0])])
        phi_card[k,i] = it_phi[int(str_card[k,i])-1]

# new rows for the new structures are created
# the old structure is storaged in the new row
for k in range(len(spl_index)):
    row = argwhere(str_card[:,i-1]== spl_index[k])[0][0]
    for l in range(int(nspl[k])):
        str_card        = append(str_card,array(str_card[row,:])[nw,:],
            axis=0)
        str_card[-1,-1] = int(spl_new_index[k][l])
        phi_card        = append(phi_card,array(phi_card[row,:])[nw,:],
            axis=0)
        phi_card[-1,-1] = it_card[int(str_card[-1,-1])-1]
```

It is also possible to create a clustering loop for the events, where the precursor structure is nicknamed 'father' and the successor structures 'sons'.

```
# Clustering loop
for z in range(len(case_list)):
    str_card = str_card_list[z]
    event_list   = []                                   # index == number
        of structure
    father_index = []
    alive        = []
    extinction   = []
    sons_overall = []
    total_str = len(str_card[:,0])
    for ii in range(total_str):
        i = total_str -1 -ii
        if isnan(sum(str_card[i,:])):                   # nan: ext/splt
            nan_index = len(str_card[i,:][~np.isnan(array(str_card[i,:],
                dtype=float))])
            col = array(str_card[:,nan_index-1],dtype=float)
            num = array(str_card[i,nan_index-1],dtype=int)
            unique, counts = np.unique(col, return_counts=True)

            if counts[argwhere(unique==num)][0][0]>1:    # splitting
                father_index.append(i)
                sons_index = []
                for j in range(len(argwhere(col==num))):
                    son = argwhere(col==num)[j]
                    if np.any(son == array(sons_overall)) or son<=i:
```

```
                        continue
                    sons_index.append(argwhere(col==num)[j])
                    sons_overall.append(argwhere(col==num)[j])
                    #print('pasa')
                event_list.append([i,'splitting event',array(sons_index)])

            else:                                           # extinction
                event_list.append([i,'extinction'])
                extinction.append(i)
        else:
            event_list.append([i,'alive'])
            alive.append(i)

    event_simul[z] = event_list
    alive_simul.append(alive)
    extinction_simul.append(extinction)
    sons_simul.append(sons_overall)
```

Appendix D: Bi-dimensional polar computations

A validation of the theoretical distributions for the temperature and species field is offered through a numerical implementation of eqs. (6.11) and (6.13), which is presented in this section. Both equations are rewritten in a vectorial way as follows

$$\mathbf{Le}\left\{\cos\theta\frac{\partial\boldsymbol{\phi}}{\partial\zeta}-\sin\theta\frac{1}{\zeta}\frac{\partial\boldsymbol{\phi}}{\partial\theta}\right\}=\frac{1}{\zeta}\frac{\partial}{\partial\zeta}\left(\zeta\frac{\partial\boldsymbol{\phi}}{\partial\zeta}\right)+\frac{1}{\zeta^2}\frac{\partial^2\boldsymbol{\phi}}{\partial\theta^2}-\frac{1}{\mathrm{Pe}^2}\mathbf{b}\boldsymbol{\phi} \tag{18}$$

where $\zeta = r\mathrm{Pe}$, $\mathbf{Le} = \{1, \mathrm{PeLe}\} = \{1, 0.3\}$, $\mathbf{b} = \{b, 0\}$ and $\boldsymbol{\phi} = \{T, Y\}$. A pseudo-transient relaxation method is applied with second-order finite differences to discretize the equation. The spatial discretization is optimized through a change of variable that transforms the radial $\zeta-$coordinate array into a more convenient distribution of points. In particular, a logarithmic change is proposed since a fine resolution is desired close to the flame area, where the jump condition is imposed. Moreover, it also allows to solve the largest domain possible with far-decay boundary conditions. Applying the change of variable $\xi = \ln(\zeta)$, the equation reads

$$\mathbf{Le}\exp(\xi)\left\{\cos\theta\frac{\partial\boldsymbol{\phi}}{\partial\xi}-\sin\theta\frac{\partial\boldsymbol{\phi}}{\partial\theta}\right\}=\frac{\partial^2\boldsymbol{\phi}}{\partial\xi^2}+\frac{\partial^2\boldsymbol{\phi}}{\partial\theta^2}-\exp(2\xi)\frac{\mathbf{b}}{(\mathrm{Pe})^2}\boldsymbol{\phi} \tag{19}$$

The numerical domain is a semicircle $r \in [0, r_{end}]$, $\theta \in [0, \pi]$, imposing a symmetry boundary condition on the $x-$axis, $\partial/\partial\theta = 0$. The value of the temperature and species field is fixed at the flame front, located at $r = 1$ (or $\xi = \ln(\mathrm{Pe})$). For the outermost boundary, another Dirichlet condition is used. In particular, for a large enough domain ($r \gtrsim \mathrm{Pe}^{-1}$) the far-field expansion series developed in chapter 6 are valid for the outer region. Then, the theoretical value for the variables is used, $T(\zeta = A) = T_{\mathrm{far}}(\zeta = A)$ and $Y(\zeta = A/\mathrm{Le}) = Y_{\mathrm{far}}(\zeta = A/\mathrm{Le})$, with A a number greater than unity. The domain dependency on the coordinate ζ gives the same density of points for the different Pe computation cases. In addition, a more convenient distribution of points through the logarithmic change of variable is obtained.

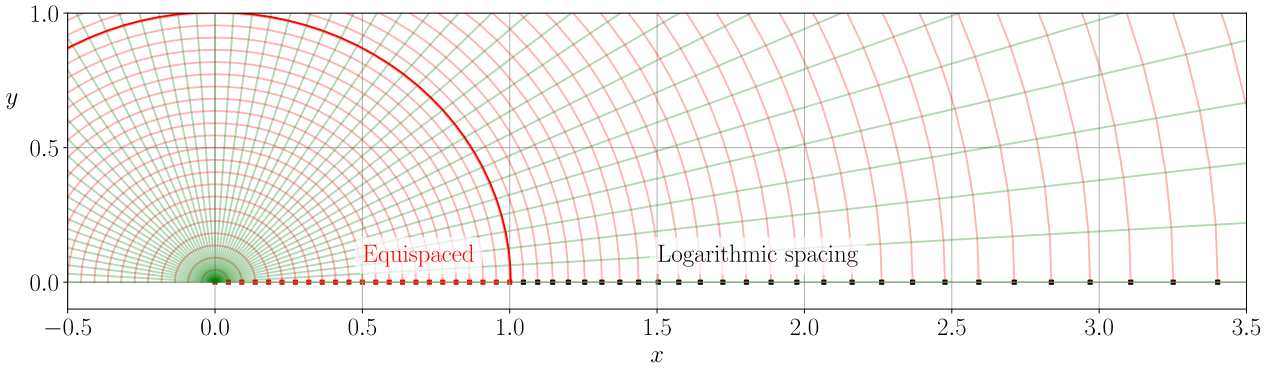

Figure 2: Polar mesh, homogeneous radial spacing for the inner part (red dots), logarithmic radial spacing for the outer part (black dots).

Appendix E: One-dimensional flame computations

Non-adiabatic planar flame model, physical space

Equations system for the non-adiabatic planar flame model used through chapter 7, (7.15), are here recovered:

$$m\frac{\partial T}{\partial x} = \frac{\partial^2 T}{\partial x^2} + \Omega - bT, \qquad m\frac{\partial Y}{\partial x} = \frac{1}{\mathrm{Le}}\frac{\partial^2 Y}{\partial x^2} - \Omega, \tag{20}$$

The non-dimensional variables used correspond to the generic ones defined in chapter 3. Space coordinates are related to the flame thickness δ'_T, $x = x'/\delta'_T$, $y = y'/\delta'_T$. Temperature $T = (T' - T'_u)/(T'_a - T'_u)$, species $Y = Y_F/Y_{F_u}$, and mass flow $m = \rho u$. The heat losses term is written in an analogous way to the two-dimensional case, a sink term depending on temperature through the parameter b. In addition, the production term reads,

$$\Omega = \rho^2 \beta^2 (1+q)^2 \frac{Y}{2 s_L^2 \mathrm{Le}} \exp\left(\frac{\beta(T-1)}{1 + \frac{q}{1+q}(T-1)}\right). \tag{21}$$

The original system of equations is linearized following $T \to T_0 + dT$, $Y \to Y_0 + dY$, $\Omega \to \Omega_0 + d\Omega \to \Omega_0 + \partial\Omega/\partial T|_0\, dT + \partial\Omega/\partial Y|_0\, dY$, giving rise to

$$m_0\frac{\partial dT}{\partial x} + dm\frac{\partial T_0}{\partial x} - \frac{\partial^2 dT}{\partial x^2} - d\Omega = -m_0\frac{\partial T_0}{\partial x} + \frac{\partial^2 T_0}{\partial x^2} + \Omega_0 \tag{22}$$

$$m_0\frac{\partial dY}{\partial x} + dm\frac{\partial Y_0}{\partial x} - \frac{1}{\mathrm{Le}}\frac{\partial^2 dY}{\partial x^2} + d\Omega = -m_0\frac{\partial Y_0}{\partial x} + \frac{1}{\mathrm{Le}}\frac{\partial^2 Y_0}{\partial x^2} - \Omega_0 \tag{23}$$

Second-order centered finite differences are used to discretize the equations to linearly solve dT, dY and dm directly inverting the problem matrix M $d\phi = f(\phi_0)$. Here $d\phi$ represents the unknown perturbations of variables and ϕ_0 the previous-step variable values.

The mass-flow eigenvalue m is calculated by the exchange of the unknown variable dm in one of the points of the domain (index=i) where the temperature value is imposed, $dT_i = 0$. Submatrices (24) and (25) sketch the structure of the discrete-problem matrix. Elements A, B, C and AY, BY, CY represent the three main diagonals of the second-order scheme. Elements D and DY indicate the change in the unknown variable for the index i and, E and EY the remaining cross terms. The system to solve in each iteration is presented in (26). A relaxation method is used to converge the solution from an initial condition built from two hyperbolic tangents. Figures 3 and 4 show a visual reference of how convergence occurs for Le = 0.3 and Le = 1.0 cases.

$$M00 = \begin{pmatrix} B & A & & D_0 & \cdots & 0 \\ C & B & \ddots & \vdots & & \vdots \\ & \ddots & \ddots & & & \\ & & & D_i & & \\ \vdots & & & \vdots & & A \\ 0 & \cdots & & D_{N-1} & C & B \end{pmatrix}; \; M11 = \begin{pmatrix} B_Y & A_Y & & & \cdots & 0 \\ C_Y & B_Y & \ddots & & & \vdots \\ & \ddots & \ddots & & & \\ & & & & & \\ \vdots & & & & & A_Y \\ 0 & \cdots & & & C_Y & B_Y \end{pmatrix} \tag{24}$$

$$M01 = \begin{pmatrix} E & & & \cdots & 0 \\ & E & & & \vdots \\ & & \ddots & & \\ & & & & \\ \vdots & & & & \\ 0 & \cdots & & & E \end{pmatrix}; \; M10 = \begin{pmatrix} EY & & & DY_N & \cdots & 0 \\ & EY & & \vdots & & \vdots \\ & & \ddots & & & \\ & & & DY_{i+N} & & \\ \vdots & & & & & \\ 0 & \cdots & & DY_{2N-2} & & EY \end{pmatrix} \tag{25}$$

$$M = \begin{pmatrix} M00 & M01 \\ M10 & M11 \end{pmatrix}; \qquad M \begin{pmatrix} dT_0 \\ \vdots \\ \\ \\ dm \\ \\ dT_{N-1} \\ dY_0 \\ \vdots \\ dY_{N-1} \end{pmatrix} = \begin{pmatrix} f_0 \\ \vdots \\ \\ \\ dm \\ \\ f_{N-1} \\ fY_0 \\ \vdots \\ fY_{N-1} \end{pmatrix} \tag{26}$$

where the diagonals building the problem matrix read,

$$A = \frac{m_0}{2dx} - \frac{1}{dx^2}, \qquad AY = \frac{m_0}{2dx} - \frac{1}{dx^2}$$

$$B = \frac{2}{dx^2} - \mathcal{C}Y\left(-\frac{2q}{(1+qT)^3} + \frac{\beta\,(q+1)^2}{(1+qT)^4}\right), \qquad BY = \frac{2}{dx^2} + \mathcal{C}\frac{1}{(1+qT)^2}$$

$$C = -\frac{m_0}{2dx} - \frac{1}{dx^2}, \qquad CY = -\frac{m_0}{2dx} - \frac{1}{dx^2}$$

$$D = \frac{\partial T_0}{\partial x}, \qquad DY = \frac{\partial Y_0}{\partial x}$$

$$E = -\mathcal{C}\frac{1}{(1+qT)^2}, \qquad EY = \mathcal{C}Y\left(-\frac{2q}{(1+qT)^3} + \frac{\beta\,(q+1)^2}{(1+qT)^4}\right)$$

where

$$\mathcal{C} = \frac{\beta^2\,(1+q)^2}{2s_l^2\mathrm{Le}}\exp\left(\frac{\beta\,(q+1)\,(T-1)}{1+qT}\right).$$

Non-adiabatic flame model, composition space

The energy equation in composition space is also computed to explore the addition of the transverse-curvature and heat-loss effects. Equation (7.19) is discretized using a second-order centered finite differences, and it is numerically converged to the steady state through a pseudotransient integration, use made of a fourth order Runge-Kutta temporal scheme, RK4.

$$\frac{\partial T}{\partial t_{\mathrm{pseu}}} = \underbrace{\frac{\partial^2 T}{\partial Y^2}g_Y^2 + \frac{\partial T}{\partial Y}\left(1 - \frac{1}{\mathrm{Le}}\right)g_Y\left(\frac{\partial g_Y}{\partial Y} - \kappa\right) + \Omega\left(1 + \frac{\partial T}{\partial Y}\right) - bT}_{RHS} \tag{27}$$

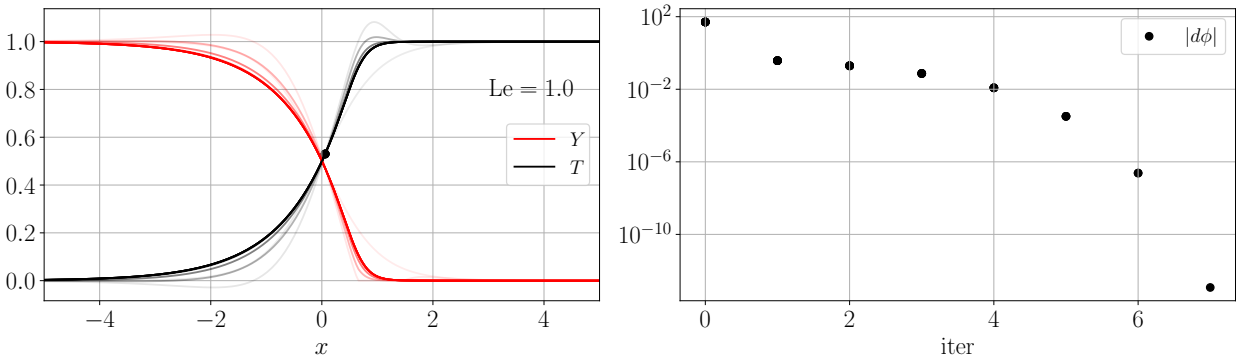

Figure 3: Le = 1.0 planar flame computation. On the left, temperature and species distribution from the initial condition to the final stationary solution (increasing opacity). On the left, iteration residual for each iteration.

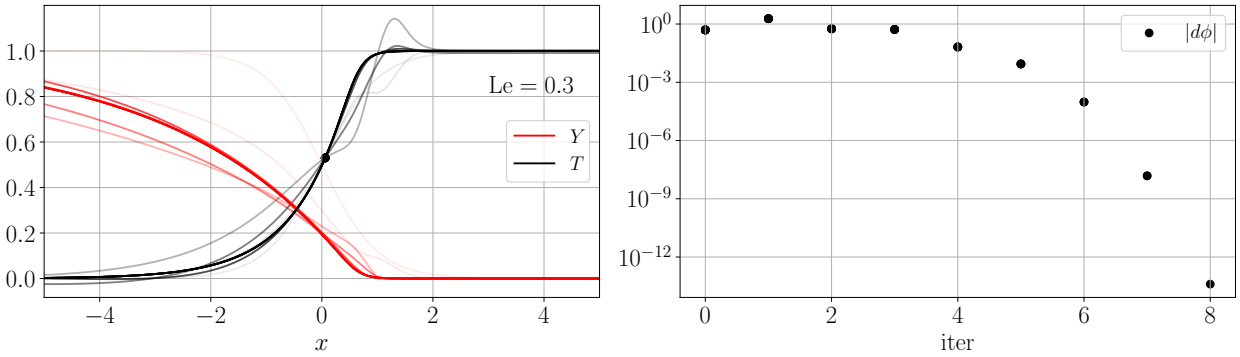

Figure 4: Le = 0.3 planar flame computation. On the left, temperature and species distribution from the initial condition to the final stationary solution (increasing opacity). On the left, iteration residual for each iteration.

The computation is based on the following code shell. The successive temporal steps of integration are calculated through the loop at the bottom of the code extract. RK4 function is called for each time instant, where the integration scheme is contained. This function, likewise, depends on the right hand side of eq. (27), evaluated explicitly. At each step, a residual, based on the difference between the present state and the previous one, is compared to a tolerance criterium to exit the process.

```
def rhs(phi):
    dphi = ... (RHS evaluation)

def RK4(rhs, phi, dphi):
    k1[:] = rhs(phi, dphi)
    k2[:] = rhs(phi + dt2*k1, dphi)
    k3[:] = rhs(phi + dt2*k2, dphi)
    k4[:] = rhs(phi + dt *k3, dphi)
    phi += dt2*(k1 + 2*(k2 + k3) + k4)/3

# Temporal loop
for i in range(it_max):
    RK4(rhs, phi, dphi)
```

```
residue = ...
if (residue<tolerance):
    break
```